THESIS FOR THE DEGREE OF LICENTIATE OF ENGINEERING

in

Thermo and Fluid Dynamics

Development of Vortex Filament Method for Aerodynamic Loads on Rotor Blades

by

HAMIDREZA ABEDI

Department of Applied Mechanics
CHALMERS UNIVERSITY OF TECHNOLOGY
Gothenburg, Sweden, 2013

Development of Vortex Filament Method for Aerodynamic Loads on Rotor Blades
HAMIDREZA ABEDI

THESIS FOR LICENTIATE OF ENGINEERING No. 2013:22
ISSN 1652-8565

Department of Applied Mechanics
Chalmers University of Technology
SE-412 96 Gothenburg
Sweden
Telephone +46-(0)31-7721000

This document was typeset using LaTeX

Printed at Chalmers Reproservice
Gothenburg, Sweden, 2013

Development of Vortex Filament Method for Aerodynamic Loads on Rotor Blades

HAMIDREZA ABEDI

hamidreza.abedi@chalmers.se
Department of Applied Mechanics
Chalmers University of Technology

Abstract

Wind power is currently one of the most reliable new energy sources serving as an alternative to fossil fuel generated electricity and is known as a widely distributed clean and renewable source of energy. It is now the world's fastest growing energy source and has also become one of the most rapidly expanding industries.

The aerodynamics of a wind turbine are governed by the flow around the rotor, where the prediction of air loads on rotor blades in different operational conditions and its relation to rotor structural dynamics is crucial for design purposes. One of the most important challenges in wind turbine aerodynamics is therefore to accurately predict the forces on the blade, where the blade and wake are modeled by different approaches such as the Blade Element Momentum (BEM) theory, the vortex method and Computational Fluid Dynamics (CFD). Here, the application of the vortex filament method for wind turbine aerodynamic performance is used. Different blade models such as the lifting line and the lifting surface with prescribed and free wake models are studied. The main purpose is to find the proper combination of blade and wake models for the aerodynamic loads as well as the computational time in order to develop an accurate and efficient aerodynamic tool. The results of the different approaches are compared with the BEM method and GENUVP code (see the acknowledgments).

Keywords: aerodynamic load, rotor blade, wind turbine, lifting line, lifting surface, vortex lattice method, prescribed wake, free wake.

Acknowledgments

I would like to express my sincere gratitude to my supervisors, Professor Lars Davidson and Professor Spyros Voutsinas for their support, guidance and encouragement. This thesis would never reach to this point without their enlightening discussions and brilliant advices.

I would like to thank Ingemar Carlen at Teknikgruppen AB for his valuable advice and insights. I should thank Vasilis Riziotis and Petros Chasapogiannis for the novel ideas that they have shared with me during the study visit in National Technical University of Athens (NTUA) and also my best friend, Alireza Majlesi for his excellent contribution.

Thanks to all my colleagues and friends at the fluid dynamics division for creating an enjoyable working atmosphere, especially Mohammad Irannezhad for his valuable advices in both academic and life problems.

My warmest and deepest sense of gratitude goes to my family; my father Abbas, the first teacher in my life, who taught me dignity and loyalty; my mother, Maryam, the teacher of love and selflessness and my sister Fatemeh, for her companionship and patience. Thanks for their interminable love and support.

This project is financed through the Swedish Wind Power Technology Centre (SWPTC), see the Preface.

The technical support of National Technical University of Athens (NTUA) to use the GENUVP is greatfully acknowledged. (GENUVP is an unsteady flow solver based on vortex blob approximations developed for rotor systems by National Technical University of Athens).

Preface

The Swedish Wind Power Technology Centre (SWPTC) is a research centre for design of wind turbines. The purpose of the Centre is to support Swedish industry with knowledge of design techniques as well as maintenance in the field of wind power. The research in the Centre is carried out in six theme groups that represent design and operation of wind turbines; Power and Control Systems, Turbine and Wind loads, Mechanical Power Transmission and System Optimisation, Structure and Foundation, Maintenance and Reliability as well as Cold Climate. This project is part of Theme group 2.

SWPTCs work is funded by the Swedish Energy Agency, by three academic and thirteen industrial partners. The Region Västra Götaland also contributes to the Centre through several collaboration projects.

List of publications

This thesis is based on the work contained in the following publications:

I H. Abedi, L. Davidson, and S. Voutsinas. Vortex Method Application for Aerodynamic Loads on Rotor Blades, EWEA Conference 2013, Europes Premier Wind Energy Event, Vienna, Austria.

Nomenclature

Latin symbols

$\mathbf{D}'$	Drag force vector per unit span length
$\mathbf{e}$	Unit vector
$\mathbf{L}$	Lift force vector
$\mathbf{L}'$	Lift force vector per unit span length
$\mathbf{n}$	Normal unit vector
$\mathbf{r}$	distance vector
$\mathbf{V}$	Velocity vector
$\mathbf{x}'$	Position vector
$\mathbf{x}$	Position vector
c	Chord length
C_L	Lift coefficient
$d\mathbf{l}$	Infinitesimal length of a vortex filament
$d\mathbf{s}$	Infinitesimal path vector
dM	Infinitesimal generated torque
F_n	Normal force
F_t	Tangential force
h	Perpendicular distance
K_v	Correction factor
L	Vortex filament length
M	Generated torque, Number of spanwise section
N	Number of chordwise section
N_b	Number of blade
P	Generated power
T	Thrust
t	Time
V_θ	Tangential velocity
C	Constant, A curve
r	radius, distance

Greek symbols

α	Constant number, Angle of attack
β	Damping factor
$\Delta\mathbf{y}$	Vortex ring length
δ	Cut-off radius
Γ	Circulation
ν	Kinematic viscosity
$\mathbf{\Omega}$	Rotational velocity, Vorticity

ω	Rotational velocity
Φ	Velocity potential, Scalar potential
ϕ	Flow angle
Ψ	Vector potential
ρ	Density
θ_0	Initial angle
Subscripts	
∞	Infinity, Free stream
ax	Axial
b	Blade
bound	Bound vortex
circ	Circumferential
eff	Effective
geom	Geometric
ind	Induced
n	Normal direction
p	Pitch
t	Tangential direction, Twist, Time step
T.E.	Trailing edge
tot	Total
und	Undisturbed
Symbols	
∇	Del operator
Abbreviations	
BEM	Blade Element Momentum
CFD	Computational Fluid Dynamics
GW	Giga Watt
LLPW	Lifting Line Prescribed Wake
MW	Mega Watt
NRMSE	Normalized Root Mean Squared Error
PV	PhotoVoltaics
RHS	Right-hand side
SWPTC	Swedish Wind Power Technology Centre
VLFW	Vortex Lattice Free Wake
VLM	Vortex Lattice Method
VLPW	Vortex Lattice Prescribed Wake

Contents

Chapter 1

Introduction

1.1 Wind Energy Global Market and Industry

Among clean energy sources that are renewable, wind is regarded as less destructive to the environment. By the exponential growth of wind turbines all around the world, and its general acceptance among people, the demand and its worthwhileness makes it apt for research, especially to enhance its accurate performance.

According to data provided by the **Renewables Global Status Report** in 2013, wind capacity increased globally by 19%, the increase being 45 GW. That is, it reached 283 GW to a record high despite the uncertainty in the policy in the key markets. The total 85% of the global capacity, however, is accounted for by only 10 countries even though the market continues to grow. From 2007 to 2013, the growth rate of cumulative wind power capacity reached on average of 25%. Forty four countries added capacity during 2012 and 64 produced greater than 10 MW and 24 less than 1 GW in operation. The EU passed the highest record of 100 GW in 2012, adding 11.9

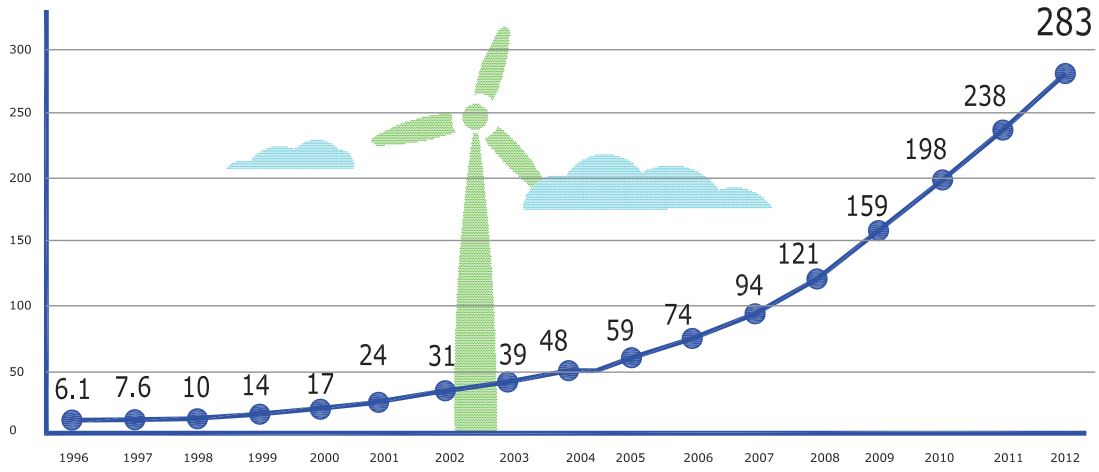

Figure 1.1: Wind power global capacity, 1996-2012

GW of wind capacity for a total of 106 GW. After solar PV (37%), ranking higher in comparison to natural gas (23%), wind capacity for supplying electricity comes in second (26.5%). 11.4% of the EU electric capacity was supplied by wind by the year end.

The increasing production of electric energy by wind is now 45% of the total production of

electric energy in the U.S. It now a more successful industry than natural gas, supplying power to 15.2 million U.S. homes by 60 GW at year end.

There other countries that have speeded up their investment in this industry. For instance, China, up to 2011, had installed almost 13 GW, the equivalent of 27% in the world market, even though it now shows comparatively low installation. Germany is still a giant in the European market, having the highest number of installation in the last decade (2.4 GW), totalling 31.3 GW. The U.K may be ranked the second in Europe for the new installations adding, by this year end, the 1.9 GW totalling 8.4 GW. 45% of the U.K installations are offshore. The leading markets in Europe are Italy (1.3 GW), Spain (1.1 GW), Romania (0.9 GW), and Poland (almost 0.9 GW), among which Poland and Romania had record years by increasing their capacity respectively 55% and almost 100%. India has been also made its name as a phenomenon by keeping its global ranking in fifth place by adding about 2.3 GW, totalling 18.4 at year end. Viewing around the

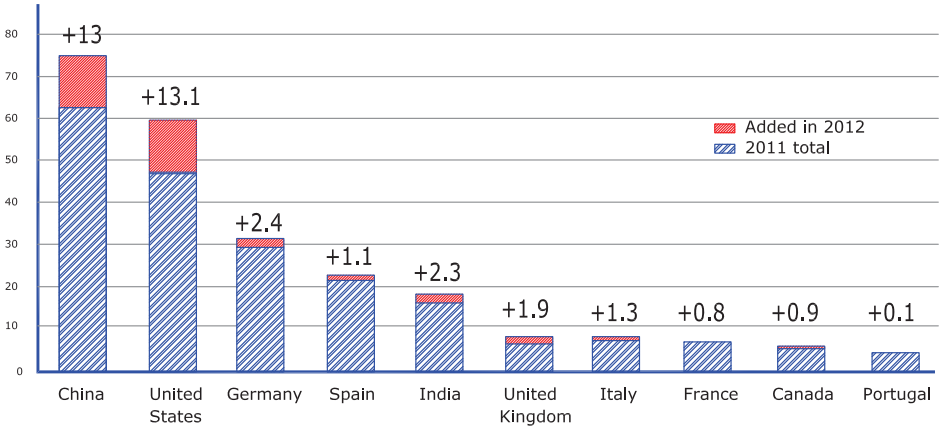

Figure 1.2: Wind power capacity and additions, top 10 countries, 2012

world as a whole, one cannot forget the rapid growth in Latin America, including Brazil, with 1.1 GW adding to its capacity of 2.5 GW, supplying 4 million households. Furthermore, Mexico also added 0.8 GW to reach a total of 1.4 GW, when the region's largest project (306 MW) was initiated. In the region, those that added to their capacity include Argentina, Costa Rica, Nicaragua, Uruguay, and Venezuela commissioned its first commercial wind farm (30 MW).

In North America, Canada has had the second best year by adding more than 0.9 GW, to reach a total of 6.2 GW. In Canada, Ontario, a totalling over 2 GW, and Alberta and Quebec, producing 1 GW each, have shown a significant change.

The development is not eye-catching in Africa and the Middle East , even though Tunisia added 50 MW, almost doubling its capacity. Ethiopia has started to build commercial wind farms with a production of 52 MW. Several projects have been initiated in South Africa, totalling more than 0.5 GW. Elsewhere, Australia as the only country in the Pacific added a capacity of 0.4 GW, totalling about 2.6 GW. Turkey has also added 0.5 GW, for a total of 2.3 GW. At the end of 2012, there were only 13 countries worldwide that have offshore wind turbines adding 1.3 GW for a total 5.4 GW. Among those offshore operating turbines, 90% of the capacity is located off northern Europe, adding a record 1.2 GW for almost 5 GW total in ten countries. It is now up to 35% over 2011. Owing to the cost considerations, the trend to expand the single projects continues. In terms of capacity installed, even though the independent power producers and

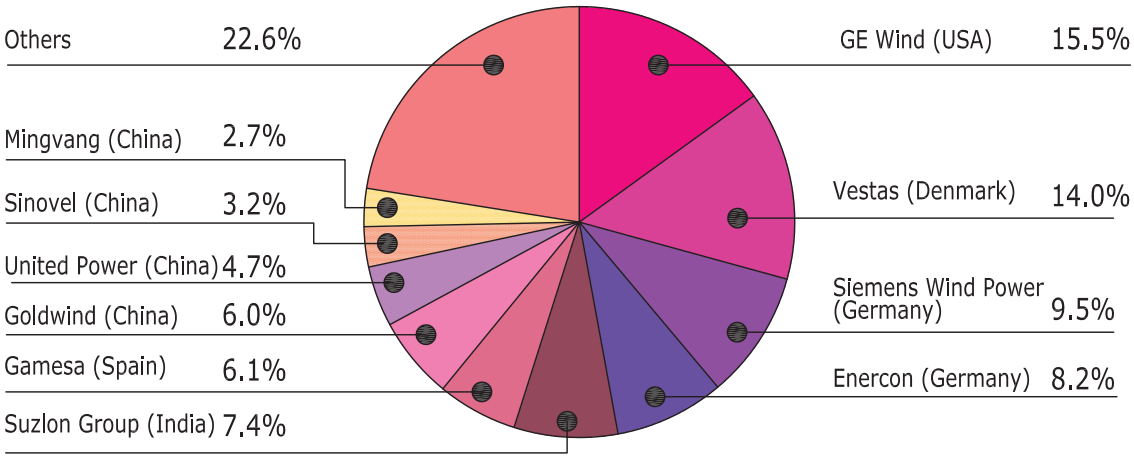

Figure 1.3: Market shares of top 10 wind turbine manufacturers, 2012

energy utilities are still the most important clients in the market, interest in community-owned wind power projects in Australia, Canada, Japan, the U.S. and part of Europe is rising. Small-scale turbines are becoming more trendy to meet the demand of energy both on and off-grid. This is because of the lower cost grid-connected inverters, the high cost of fossil fuel and governments' interventions and incentives. Small-scale turbines worldwide reached 730,000 operating at the end of 2011, producing 576 MW which is 27% over 2010.

At least 2.6-3% of the global electricity consumption in 2012 was supplied by wind power. At year end, in Europe, 7% of the region's electricity consumption was supplied by wind power, showing a rise from 6.3% in 2011. The increase can be seen in the higher share of the countries, demand being produced by wind, including Denmark (30 % in 2012; up from nearly 26 % in 2011), Portugal (20 % up from 18 %), Spain (16.3 % up from 15.9 %), Ireland (12.7 % up from 12 %), and Germany (7.7 % down from 8.1 %).

The growth in the demand for turbines worldwide was also reflected in the rise of its price between 2005 and 2009. On the other hand, there are factors to reduce the price of turbines, such as growing scale and greater efficiency, oversupply and the like. Reducing prices may however challenge the industry, and there are also challenges from increased competition among the manufacturers. At the same time, there is also competition with low-cost gas production in some markets, especially those affected by economic austerity.

1.2 Wind Energy Technology

The methods for predicting of wind turbine performance are similar to propeller or helicopter theories, where the torque generated by wind turbine blades is considered an important parameter to evaluate. There are different methods for modelling the aerodynamics of a wind turbine with different levels of complexity and accuracy, such as the BEM theory and solving the Navier-Stokes equations using CFD.

Today, an engineering model based on the BEM method is extensively used for analyzing the aerodynamic performance of a wind turbine where it is based on the steady and homogeneous flow assumption and aerodynamic loads act on an actuator disc instead of a finite number of blades. The BEM method is known as the improved model of the Rankine-Froude momentum

theory [1] and [2], which was the first model to predict inflow velocities at the rotor, where it assumes that the rotor can be replaced by a uniformally loaded actuator disc, and the inflow is uniform as well. Moreover, Prandtl's hypothesis is the foundation of the BEM method, assuming that a section of a finite wing behaves as a section of an infinite wing at an angle equal to the effective angle of attack. The BEM method is computationally fast and is easily implemented, but it is acceptable only for a certain range of flow conditions [3]. A number of empirical and semi-empirical correction factors have been added to the BEM in order to increase its application range, such as yaw misalignment, dynamic inflow, dynamic stall, tower influence, finite number of blades and blade cone angle [4], but they are not relevant to all operating conditions and are often incorrect at high tip speed ratios where wake distortion is significant [5]. The existence of these numbers of correction formula leads to uncertainties to the BEM method, while the foundation of such corrections is based on the experimental results, decreasing the reliability of the BEM method.

The vortex theory, which is based on the potential, inviscid and irrotational flow can also be used to predict the aerodynamic performance of wind turbines. The advantage of vortex flow is to reduce the flow complexity, and it has been widely used for aerodynamic analysis of airfoils and aircrafts. Although it cannot be used to predict viscous phenomena such as drag and boundary layer separation, its combination with tabulated airfoil data makes it a powerful tool for the prediction of fluid flow. Compared with the BEM method, the vortex method is able to provide more physical solutions for attached flow conditions with boundary layer corrections, and it is also valid over a wider range of turbine operating conditions. Although it is computationally more expensive than the BEM method, it is still feasible as an engineering method.

The early vortex method application was introduced by Glauert [6], Prandtl [7] and Goldstein [8]. In the Glauert theory, instead of a finite number of blades, the rotor is modeled as a uniformly loaded actuator disc and the wake is modeled as a semi-infinite cylindrical sheet of vortices that is shed from the edge of an actuator disk. The Prandtl method introduced radial inflow distribution, which leads to the tip-loss factor concept correcting the assumption of an infinite number of blades. The Goldstein theory represents the inflow by assuming the trailing vortices of each blade as a finite number of infinite length coaxial helicoidal surfaces but with a finite radius moving at a constant velocity. Falkner [9] used the vortex lattice method in 1943 to calculate aerodynamic forces on a surface of arbitrary shape. This method is still used in engineering applications because it requires relatively small computational time with a considerable level of accuracy compared with CFD.

In vortex methods, the trailing and shed vortices are generally modeled by either vortex particles or vortex filaments moving either freely, known as free wake such as work by [10], [11], [12], or restrictedly by imposing the wake geometry known as prescribed wake [13], [14]. The prescribed wake requires less computational effort than free wake, but it requires experimental data to be valid for a broad range of operating conditions. The free wake model, which is the most computationally expensive vortex method, is able to predict the wake geometry and loads more accurately than the prescribed wake because of the less restrictive assumptions.

The vortex method has historically been used for helicopters [15], [16] and [17] to model the wake and aerodynamic loads for different operational conditions. Landgrebe [18] developed a prescribed wake consisting of a number of filaments shed into the wake from the blade trailing edge that are rolled up immediately into a tip vortex. An analytical approach to predict propellers' inflow by using lifting line theory, was described by Crimi [19], where the wake is replaced by a single tip vortex and moved based on the induced velocity field during the blade rotation. Several simplified methods by Brady [20] and Trenka [21] have been developed to model the wake by

vortex rings or vortex tubes. Landgrebe [18], Leishman [22] and Sadler [23] also proposed a free wake model for helicopters, where the wake is modeled by segmented vortex filaments which are allowed to distort freely. Coton [24], Dumitrescu [25], Kocurek [26]) and Curin [27] introduced the prescribed vortex filament wake model for wind turbine applications in addition to a work by Gohard [28], which is regarded as a pioneer free wake model for wind turbines.

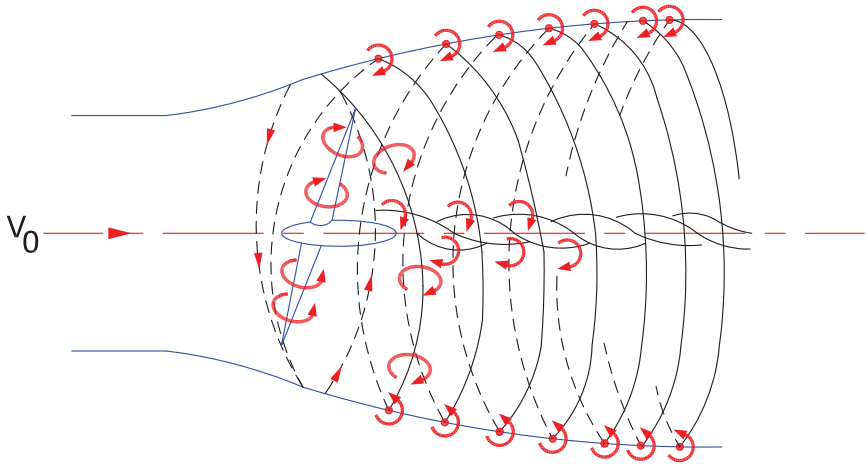

Figure 1.4: Schematic of the vortex wake behind the rotor blades [3]

Finally, CFD, which solves the Navier-Stokes equations for the flow around the rotor blade, is known as the most accurate but computationally most expensive method making it an impractical engineering method for wind turbine applications, at least with the current computational hardware resources.

To overcome this limitation, a combination of Navier-Stokes equations and an actuator disc method was proposed by Madsen [29], where instead of resolving the viscous flow around the rotor blades, the swept surface of the rotor blade is replaced by surface forces acting upon the inflow. Another method called actuator line was proposed by Sørensen [30] where the air load is distributed radially in the solution domain along the lines representing the blade forces. In this method, the blade element method and airfoil data are used to determine the aerodynamic loads in an iterative method while the wake is simulated by a 3D Navier-Stokes solver. The hybrid CFD-Inviscid method was proposed by Berkman [31], Xu [32] and Schmitz [33] in order to remove the dependency on the tabulated airfoil data while a small region around the blade is solved by Navier-Stokes equations and a full potential vortex method is applied for the rest of the computational domain.

Chapter 2

Theory

Vortex flow theory is based on assuming incompressible ($\nabla \cdot \mathbf{V} = 0$) and irrotational ($\nabla \times \mathbf{V} = 0$) flow at every point except at the origin of the vortex, where the velocity is infinite [34]. A region containing a concentrated amount of vorticity is called a vortex, where a vortex line is defined as a line whose tangent is parallel to the local vorticity vector everywhere. Vortex lines surrounded by a given closed curve make a vortex tube with a strength equal to the circulation Γ, around the vortex region. A vortex filament with a strength of Γ, is represented as a vortex tube of an infinitesimal cross-section with strength Γ. According to the Helmholtz theorem, an irrotational motion of an inviscid fluid started from rest remains irrotational. Also, a vortex line cannot end in the fluid. It must form a closed path, end at a solid boundary or go to infinity implying that vorticity can only be generated at solid boundaries. Therefore, a solid surface may be considered as a source of vorticity. This leads to replacing the solid surface in contact with fluid by a distribution of vorticity.

For an irrotational flow, a velocity potential, Φ, can be defined as $\mathbf{V} = \nabla\Phi$, where in order to find the velocity field, solving Laplace's equation, $\nabla^2\Phi = 0$, with a proper boundary condition for the velocity on the body and at infinity is used. In addition, in vortex theory, the vortical structure of a wake can be modeled by either vortex filaments or vortex particles, where a vortex filament is modeled as concentrated vortices along an axis with a singularity at the center. By introducing V_θ as the tangential velocity (see fig.(2.1)), the flow for an ideal vortex line is given by

$$V_\theta = \frac{C}{r} \tag{2.1}$$

where C is obtained by taking the circulation around a given circular streamline of radius r as

$$\begin{aligned} \Gamma = \oint_c \mathbf{V}.d\mathbf{s} = V_\theta(2\pi r) \\ V_\theta = \frac{\Gamma}{2\pi r} \end{aligned} \tag{2.2}$$

So, by comparing eqs.(2.1) and (2.2), we get

$$C = \frac{\Gamma}{2\pi} \tag{2.3}$$

where Γ is termed the strength of the vortex flow. Equation (2.3) shows that the circulation taken about all streamlines is the same value as $\Gamma = 2\pi C$. Further, eq.(2.2) gives the velocity field for a vortex flow of strength Γ. Moreover, according to vector analysis of fluid dynamics, any velocity

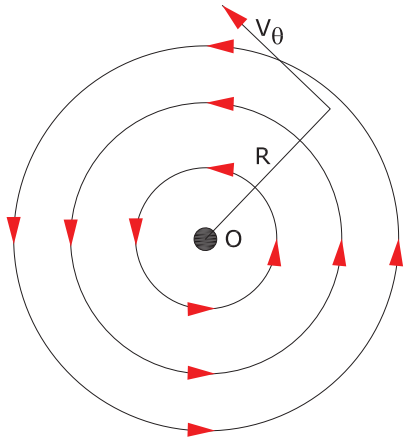

Figure 2.1: Vortex flow

field can be decomposed into a solenoidal part and a rotational part [5] as

$$\mathbf{V} = \nabla \times \Psi + \nabla \Phi \tag{2.4}$$

where Ψ is a vector potential and Φ is a scalar potential. Curl of eq.(2.4) yields

$$\nabla \times \mathbf{V} = \nabla \times (\nabla \times \Psi) + \nabla \times \nabla \Phi \tag{2.5}$$

Vector identity gives

$$\nabla^2 \Psi = \nabla (\nabla \cdot \Psi) - \nabla \times (\nabla \times \Psi) = -\nabla \times (\nabla \times \Psi) \tag{2.6}$$

where $\nabla (\nabla \cdot \Psi) = 0$ since Ψ is a solenoidal vector field (also known as an incompressible vector field) with divergence zero. From eqs.(2.5), (2.6) and the definition of vorticity, the Poisson equation for the vector potential is derived as

$$\nabla^2 \Psi = -\Omega \tag{2.7}$$

where Ω denotes the rotational velocity $(\nabla \times \mathbf{V} = \Omega)$. The solution of the Poisson equation is

$$\Psi (\mathbf{x}) = \frac{1}{4\pi} \int \frac{\Omega (\mathbf{x}')}{| \mathbf{x} - \mathbf{x}' |} dvol \tag{2.8}$$

where $\mathbf{x}$ and *dvol* denote the point where the potential and the vortex filament volume are computed, respectively. A prime denotes evaluation at the point of integration $\mathbf{x}'$, which is taken over the region where the vorticity is non-zero, designated by *dvol*. Therefore, the induced velocity field is obtained by taking the curl of eq.(2.8) as

$$\mathbf{V}_{ind} (\mathbf{x}) = -\frac{1}{4\pi} \int \frac{(\mathbf{x} - \mathbf{x}') \times \Omega}{| \mathbf{x} - \mathbf{x}' |^3} dvol \tag{2.9}$$

Similarly, the velocity induced by a straight vortex filament can be determined by the Biot-Savart law as

$$\mathbf{V}_{ind} = \frac{\Gamma}{4\pi} \frac{d\mathbf{l} \times \mathbf{r}}{| \mathbf{r} |^3} \tag{2.10}$$

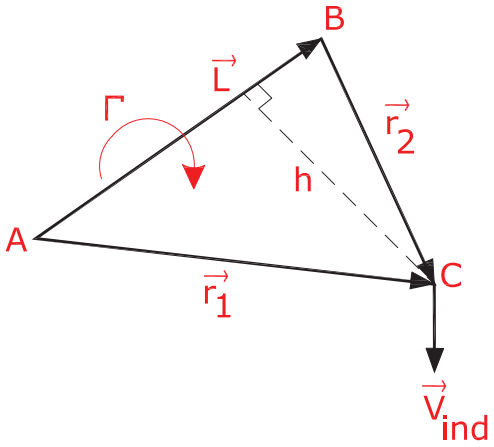

Figure 2.2: Schematic for the Biot-Savart law

which can also be written as

$$\mathbf{V}_{ind} = \frac{\Gamma}{4\pi}\frac{(r_1+r_2)(\mathbf{r}_1\times\mathbf{r}_2)}{r_1r_2+\mathbf{r}_1\cdot\mathbf{r}_2} \tag{2.11}$$

where Γ denotes the strength of the vortex filament and $\mathbf{r_1}$, $\mathbf{r_2}$ are the distance vectors from the beginning, A, and end, B, of a vortex segment to an arbitrary point C, respectively (see fig.(2.2)).

The Biot-Savart law has a singularity when the point of evaluation for induced velocity is located on the vortex filament axis. Also, when the evaluation point is very near to the vortex filament, there is an unphysically large induced velocity at that point. The remedy is either to use a cut-off radius, δ [35], or to use a viscous vortex model with a finite core size by multiplying a factor to remove the singularity [22].

The modified Biot-Savart law based on the cut-off radius can be written as

$$\mathbf{V}_{ind} = \frac{\Gamma}{4\pi}\frac{(r_1+r_2)(\mathbf{r}_1\times\mathbf{r}_2)}{r_1r_2+\mathbf{r}_1\cdot\mathbf{r}_2+(\delta L)^2} \tag{2.12}$$

where L is the length of the vortex filament. The advantage of the cut-off method is that, when the evaluation point moves toward the vortex filament, the induced velocity smoothly goes to zero. A cut-off radius value can be varied between 0.0 and 0.1 [4].

The Biot-Savart law correction based on the viscous core correction model can be done by introducing a finite core size, r_c, for a vortex filament [36]. Since the induced velocity field has a significant effect on the wake geometry and rotor aerodynamic loads, a suitable viscous core model thus increases the accuracy of the entire flow field. There are two general approaches representing the induced velocity using the desingularized algebraic profile, i.e., a constant viscous core size which is used extensively in engineering applications because of its simplicity and a diffusive viscous core size where the core size grows with time based on the Lamb-Oseen model [36]. The Rankine model is considered the simplest model for the swirl velocity inside a viscous vortex with a finite core and is defined as

$$V_\theta(\bar{r}) = \begin{cases} \left(\dfrac{\Gamma}{2\pi r_c}\right)\bar{r} & 0 \leqslant \bar{r} \leqslant 1 \\ \left(\dfrac{\Gamma}{2\pi r_c}\right)\dfrac{1}{\bar{r}} & \bar{r} > 1 \end{cases} \tag{2.13}$$

where $\overline{r} = r/r_c$, and r_c is the viscous core radius, which is defined as the radial distance from the vortex axis to the position of the maximum swirl velocity.

A general form of a desingularized algebraic swirl-velocity profile for stationary vortices is proposed by Vasitas [37] as

$$V_\theta(r) = \frac{\Gamma}{2\pi}\left(\frac{r}{(r_c^{2n} + r^{2n})^{1/n}}\right) \tag{2.14}$$

Moreover, the Lamb-Oseen vortex model for the swirl velocity is represented as

$$V_\theta(\overline{r}) = \frac{\Gamma}{2\pi r_c}\left(\frac{1 - e^{-\alpha\overline{r}^2}}{\overline{r}}\right) \tag{2.15}$$

This is a solution of the 1D laminar Navier-Stocks equations, i.e., an axisymmetric solution for the swirl velocity by assuming that the axial and radial velocities are equal to zero. In this model, the viscous vortex core radius grows with time as $r_c(t) = \sqrt{4\alpha\nu t}$ where $\alpha = 1.25643$, ν, t are constant, air kinematic viscosity and time, respectively. Figure 2.3 shows the effect of different vortex viscous core models on the tangential velocity. As can be seen, there is good agreement for the swirl velocity between the Vasitas model for $n = 2$ and the Lamb-Oseen model.

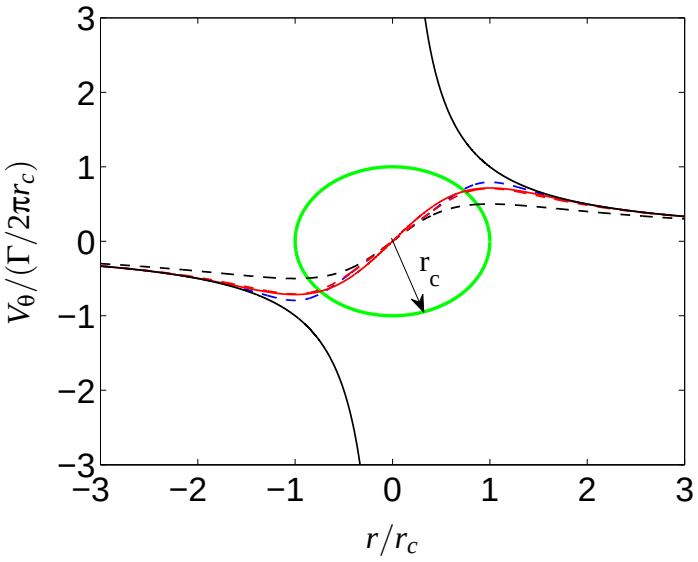

Figure 2.3: Tangential velocity of ideal vortex, Lamb-Oseen model and Vasitas model, ——: Ideal vortex, ——: Lamb-Oseen, - - - - - -: $n = 1$, - - - - - -: $n = 2$, - - - - - -: $n = 3$, ——: Vortex core

In addition, Bagai [38] suggested the velocity profile based on eq.(2.14) for $n = 2$ for the rotor tip vortices. In order to take into account the effect of viscous vortex core, a factor of K_ν must be added to the Biot-Savart law as

$$\mathbf{V}_{ind} = K_\nu \frac{\Gamma}{4\pi}\frac{(r_1 + r_2)(\mathbf{r}_1 \times \mathbf{r}_2)}{r_1 r_2 + \mathbf{r}_1 \cdot \mathbf{r}_2} \tag{2.16}$$

where

$$K_\nu = \frac{h^n}{(r_c^{2n} + h^{2n})^{1/n}} \tag{2.17}$$

and h is defined as the perpendicular distance of the evaluation point as (see fig.(2.2))

$$h = \frac{|\,\mathbf{r_1} \times \mathbf{r_2}\,|}{|\,\mathbf{L}\,|} \tag{2.18}$$

Factor K_v desingularizes the Biot-Savart equation when the evaluation point distance tends to zero and prevents a high induced velocity in the vicinity region of the vortex core radius.

Chapter 3

Application

The rotor inflow distribution is a key parameter in studies of aerodynamic loads on rotor blades and is highly dependent on the wake geometry. Hence, predicting the geometry of trailing wake vortices and their strength makes it possible to analyze wind turbine aerodynamic performance. In other words, suitable modeling of the blade and trailing wake has a great influence on the prediction of inflow at the rotor blade.

This chapter presents three different applications for modeling the blade and wake by vortex filament method, i.e., lifting line prescribed wake, vortex lattice prescribed wake and vortex lattice free wake. In these methods, the blade is modeled by either lifting line or lifting surface, and the wake is modeled by either trailing horseshoe vortices or vortex ring elements. Each engineering model is constructed on the basis of some assumptions. Some of those are discussed here.

In the prescribed wake model known as rigid wake, the upstream flow is uniform, both in time and space, and it is perpendicular to the rotor plane (parallel to the rotating axis), whereas, in the free wake model, it can be either uniform or non-uniform (varying both in time and space).

For both prescribed and free wake methods, blades are assumed to be rigid, so the elastic effect of the blades is neglected. Also, because of the large circulation gradients ($d\Gamma/dr$) near the tip and the root of the rotor blade, it is suggested to use the cosine rule for the blade radial segmentation [4].

In the prescribed wake model, the wake that is shed from the blade trailing edge follows the helix equation which consists of a helical sheet of vorticity approximated by a series of points connected by a straight vortex filament with a constant diameter and pitch. Hence, there is no wake expansion, and the wake elements move downstream with a constant velocity including free stream and axial induced velocity, where the interaction between the vortex wake filaments is ignored. In the free wake approach, a finite number of vortex wake elements move freely based on the local velocity field, allowing wake expansion as well. Each vortex wake element contains two points, one at the head and another at the tail, which are known as Lagrangian markers, where the induced velocity components are calculated using the Biot-Savart law, and their movements make the wake deformation. For both the prescribed and the free wake models, which are based on the incompressible and inviscid, it is assumed that the trailing wake vortices extend to infinity. However, since the effect of the induced velocity field by the far wake is small on the rotor blade, the wake extends only to three or four diameters downstream of the wind turbine rotor plane.

As stated before, the vortex flow is known as incompressible and inviscid flow. The viscous effect is taken into account by using 2D airfoil data applied only for the lifting line prescribed wake approach, where the power, P, and thrust, T, are calculated based on the lift and drag forces. In both vortex lattice methods, prescribed and free wakes, the power and thrust are calculated

based on the potential lift (no viscous drag force) where, in general, the lift coefficient, C_L, is a function of the angle of attack, $C_L = 2\pi\alpha$, according to the thin airfoil theory.

3.1 Lifting Line Prescribed Wake

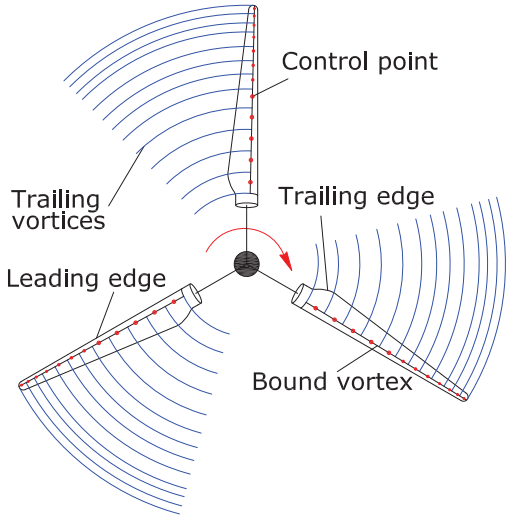

Figure 3.1: Schematic of prescribed lifting line model

The lifting line theory, originally proposed by Prandtl in 1921, is valid for a wing with an aspect ratio much greater than one. It is also suitable for slender and planar or slightly curved blades [35]. In the lifting line prescribed wake based on the Prandtl lifting line theory, the blade is divided into one or more sections that are replaced by a spanwise varying strength straight (it is not straight for a twisted blade) vortex filament Γ, called a bound vortex, which is located at $1/4$ of the chord line (downstream of the leading edge) along the span. The control points storing the bound vortex strength (circulation), the induced velocity (generated only by the wake), the free stream and the rotational velocities are located at the middle of the bound vortex of each spanwise section. In this approach, the trailing vortices are generated by spanwise bound

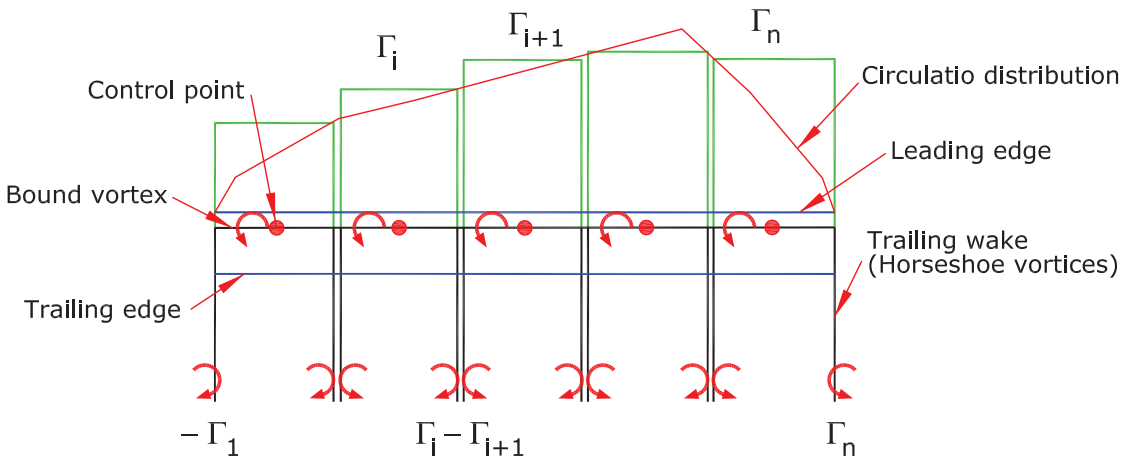

Figure 3.2: Blade and wake modeling in prescribed wake lifting line

circulation difference where they originate from the blade bound vortices. They emanate from all points along the blade, making a helical vortex sheet for each blade with a constant diameter and

pitch [39] behind each rotor blade. This helical vortex sheet induces the velocity field around the rotor blade, reducing the angle of attack seen by each blade section.

In the prescribed wake, an iterative method is used to find the final wake configuration, so the solution is started by an initial wake geometry such as a helix and an initial bound vortex distribution along the blade in order to determine the strength of the trailing wake vortices. An initialization of circulation distribution can be done by an elliptical wing circulation distribution defined as

$$\Gamma = \Gamma_{max}\sqrt{1-\left(\frac{r}{b/2}\right)^2} \tag{3.1}$$

where the blade tip position is equal to $+b/2$, and the blade root radius is equal to $-b/2$ and Γ_{max} is an arbitrary value. Another way to initialize the circulation distribution is to combine the Kutta-Jukowski theory with the lift coefficient. The Kutta-Jukowski theory is used to calculate the lift force per span (L') of each blade element as

$$\mathbf{L}' = \rho \mathbf{V}_{tot} \times \Gamma \tag{3.2}$$

where $\mathbf{V}$, Γ and ρ denote the velocity vector seen by the blade section, circulation and air density, respectively. The lift coefficient, C_L, is expressed as

$$C_L = \frac{L'}{\frac{1}{2}\rho V^2 c} \tag{3.3}$$

where c denotes the chord length of the blade section. A combination of eqs.(3.2) and (3.3) gives a correlation for circulation at each blade section as

$$\Gamma = \frac{1}{2} c V_{und} C_L(\alpha_{geom}) \tag{3.4a}$$

$$\mathbf{V}_{und} = \mathbf{V}_\infty + \Omega \mathbf{r} \tag{3.4b}$$

where $\mathbf{V}_{und}$, $\mathbf{V}_\infty$, Ω, $\mathbf{r}$ and α_{geom} denote undisturbed velocity vector, free stream velocity vector, blade rotational velocity, vector position of the control point and geometric angle of attack, respectively.

It is worth mentioning that, since the wind turbine rotor blade is often constructed by the number of different airfoil types in the spanwise direction in order to avoid a jump for the lift and drag force values between two adjacent different airfoils, the calculated lift and drag forces should be interpolated.

The geometric angle of attack is calculated by

$$\alpha_{geom} = tan^{-1}\left(\frac{\mathbf{V}_{und,n}}{\mathbf{V}_{und,t}}\right) \tag{3.5a}$$

$$\mathbf{V}_{und,n} = \mathbf{V}_{und} \cdot \mathbf{e}_n \tag{3.5b}$$

$$\mathbf{V}_{und,t} = \mathbf{V}_{und} \cdot \mathbf{e}_t \tag{3.5c}$$

where $\mathbf{e}_n$ and $\mathbf{e}_t$ are defined as (see fig.(3.3))

$$\mathbf{e}_r = \frac{\vec{\mathbf{AB}}}{|\,\vec{\mathbf{AB}}\,|} \tag{3.6a}$$

$$\mathbf{e}_t = \frac{\vec{\mathbf{CD}}}{|\,\vec{\mathbf{CD}}\,|} \tag{3.6b}$$

$$\mathbf{e}_n = \frac{\mathbf{e}_t \times \mathbf{e}_r}{|\,\mathbf{e}_t \times \mathbf{e}_r\,|} \tag{3.6c}$$

The wake geometry based on the helix equation is initialized as

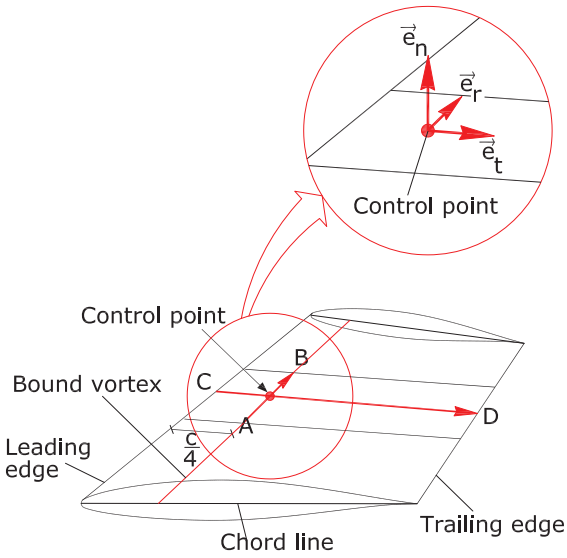

Figure 3.3: Schematic of normal and tangent unit vectors

$$\begin{aligned} x &= r\cos(\Omega t + \theta_0) \\ y &= r\sin(\Omega t + \theta_0) \\ z &= V_\infty t \end{aligned} \tag{3.7}$$

where r, Ω, V_∞, θ_0 and t denote the rotor section radius, rotor blade rotational velocity, free stream velocity, blade initial angle and time, respectively. The prescribed trailing vortices are divided into a number of straight segments where the segmentation is done based on the azimuthal angle. The accuracy of the velocity field induced by the wake depends on the number of segments per blade rotation, where a coarse segmentation gives a poor quality for the induced velocity field leading to an incorrect load estimation. It will be shown in the results that 10 degrees of azimuth segmentation satisfy both the accuracy and computational time efficiency. Once the wake is prescribed, the velocity field, $\mathbf{V}_{ind}$, induced by all equally segmented vortex filaments of the wake is calculated for all control points located at the blade bound vortex by the Biot-Savart law. The undisturbed velocity is modified as

$$\mathbf{V}_{tot} = \mathbf{V}_{und} + \mathbf{V}_{ind} \tag{3.8}$$

Theoretically, the effective angle of attack is defined as $\alpha_{eff} = \alpha_{geom} - \alpha_{ind}$. Knowing the values of α_{eff} for each blade section and using the aerodynamic table (C_L, C_D vs. α) give the lift and drag forces per blade span, and the torque and power of the wind turbine are then computed by tangential and normal forces with respect to the rotor plane, respectively.

$$\alpha_{eff} = tan^{-1}\left(\frac{\mathbf{V}_{tot,n}}{\mathbf{V}_{tot,t}}\right) \tag{3.9a}$$

$$\mathbf{V}_{tot,n} = \mathbf{V}_{tot} \cdot \mathbf{e}_n \tag{3.9b}$$

$$\mathbf{V}_{tot,t} = \mathbf{V}_{tot} \cdot \mathbf{e}_t \tag{3.9c}$$

The updated value for the circulation is given by

$$\Gamma = \frac{1}{2} c V_{tot} C_L(\alpha_{eff}) \tag{3.10}$$

Using a damping factor (β) prevents the solution from diverging, so the updated circulation distribution for the next iteration can be expressed as

$$\Gamma = \Gamma_{old} + \beta(\Gamma_{eff} - \Gamma_{old}) \tag{3.11}$$

The circulation convergency criterion for each control point is

$$\left| \frac{\Gamma_{new} - \Gamma_{old}}{\Gamma_{old}} \right| < 0.001 \tag{3.12}$$

When the criterion is fulfilled by all control points, then we are able to update the wake geometry. This is done as

$$\begin{aligned} x &= r cos(\Omega t + \theta_0) \\ y &= r sin(\Omega t + \theta_0) \\ z &= tan\phi_{eff} \Omega r t \end{aligned} \tag{3.13}$$

where r, Ω, θ_0, ϕ_{eff} and t denote the rotor section radius, rotor blade rotational velocity, blade initial angle, flow angle and time, respectively, and the effective flow angle (ϕ_{eff}) is defined as

$$\phi_{eff} = \alpha_{eff} + \theta_t + \theta_p \tag{3.14}$$

where α_{eff}, θ_t and θ_p represent the effective angle of attack, the blade section local twist and the blade pitch, respectively (see fig.(3.5)). Recall that in each iteration, the circulation distribution

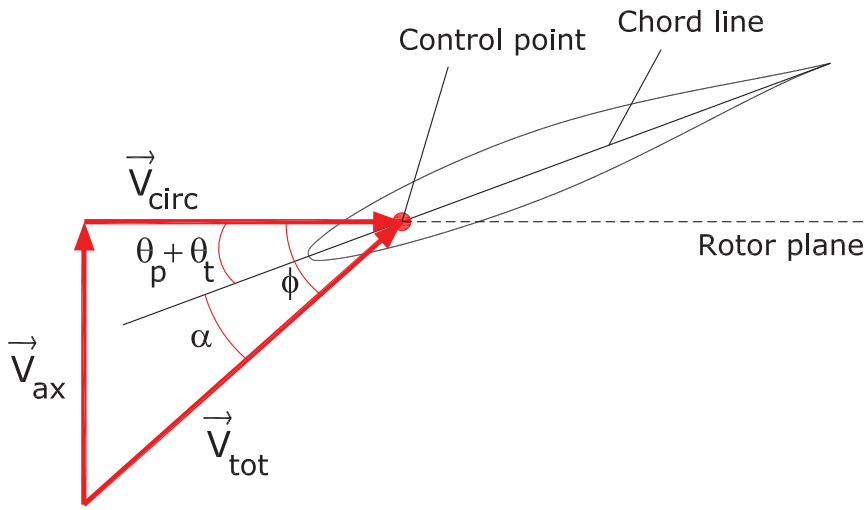

Figure 3.4: Schematic of velocity triangle

of the trailing vortices is updated hence the induced velocity field at the control points is changed, resulting in the updated released emission angle of the trailing vortices (see fig.(3.5)).

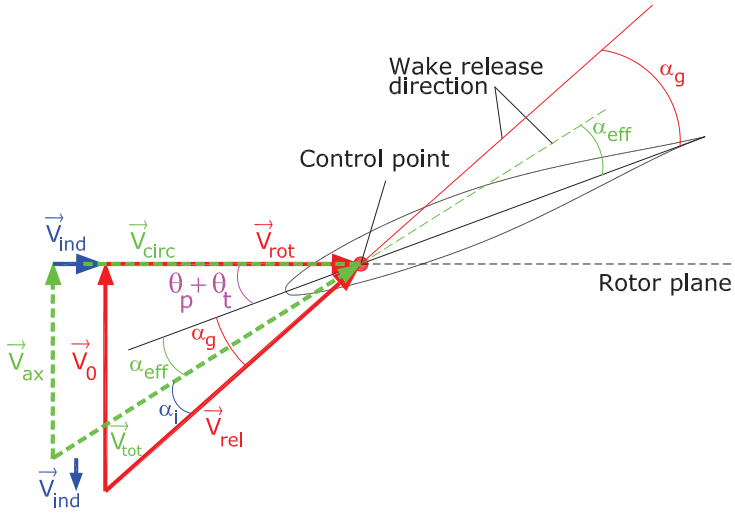

Figure 3.5: Schematic of wake emission angle

Using the 2D airfoil data to calculate the lift (L') and drag (D') forces per span at each control point based on the effective angle of attack yields

$$L' = \frac{1}{2}\rho c V_{tot}^2 C_L(\alpha_{eff}) \tag{3.15a}$$

$$D' = \frac{1}{2}\rho c V_{tot}^2 C_D(\alpha_{eff}) \tag{3.15b}$$

In order to calculate the torque and the thrust of a wind turbine, the lift and drag forces must be projected into the normal and tangential directions with respect to the rotor plane thus according to fig.(3.6), we get

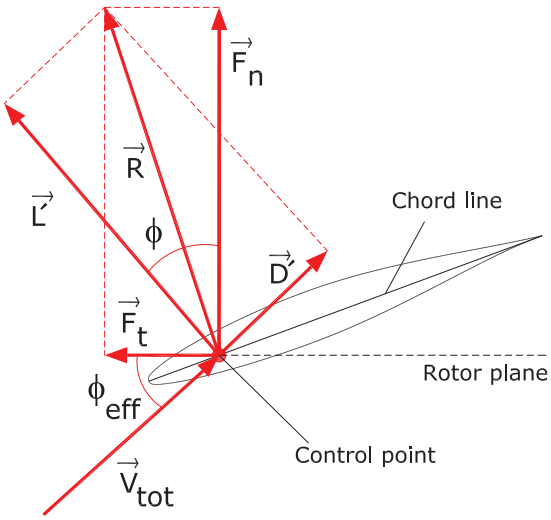

Figure 3.6: Decomposition of the lift and drag forces with respect to the rotor plane

$$F_n = L'cos\phi + D'sin\phi \tag{3.16a}$$

$$F_t = L'sin\phi - D'cos\phi \tag{3.16b}$$

By assuming a linear variation for the normal and tangential forces [3] stored at the control points between two adjacent radial position, $\mathbf{r}_i$ and $\mathbf{r}_{i+1}$, we get

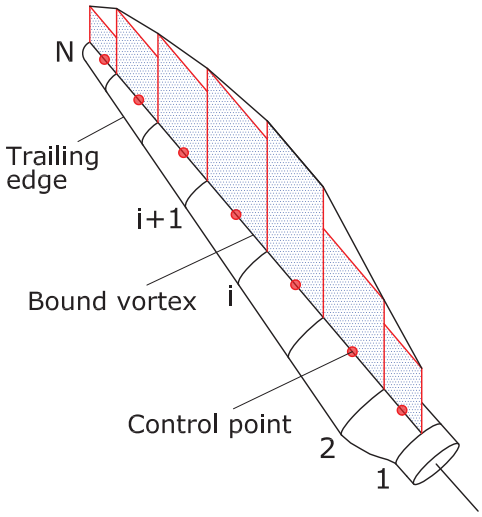

Figure 3.7: Schematic of blade segmentation

$$F_{t,i} = A_i r + B_i \tag{3.17}$$

where

$$A_i = \frac{F_{t,i+1} - F_{t,i}}{r_{i+1} - r_i} \tag{3.18a}$$

$$B_i = \frac{F_{t,i} r_{i+1} - F_{t,i+1} r_i}{r_{i+1} - r_i} \tag{3.18b}$$

The generated torque for an infinitesimal part of the blade of length dr is defined as

$$dM = r F_{t,i} dr = \left(A_i r^2 + B_i r\right) dr \tag{3.19}$$

where, by integrating of dM between $r_{i+1}$and r_i, we get

$$M|_i^{i+1} = \frac{1}{3} A_i \left(r_{i+1}^3 - r_i^3\right) + \frac{1}{2} B_i \left(r_{i+1}^2 - r_i^2\right) \tag{3.20}$$

By summation over all blade sections and multiplying by the rotational velocity of the blade, the total power is calculated as

$$P = \Omega N_b \sum_{i=1}^{k-1} M|_i^{i+1} \tag{3.21}$$

where N_b and k denote the number of rotor blade(s) and the number of blade segments (see fig.(3.7)). The thrust of each blade section is calculated as

$$T|_i^{i+1} = F_{n,i} \left(r_{i+1} - r_i\right) \tag{3.22}$$

and the total thrust is obtained by

$$T = N_b \sum_{i=1}^{k-1} T|_i^{i+1} \tag{3.23}$$

The convergency criterion is set based on the generated power so that the power difference between two consecutive iterations must satisfy the below criterion as

$$|\frac{P_{new}-P_{old}}{P_{old}}|<0.001 \tag{3.24}$$

and the iteration procedure is repeated until eq.(3.24) is satisfied.

3.2 Vortex Lattice Prescribed Wake

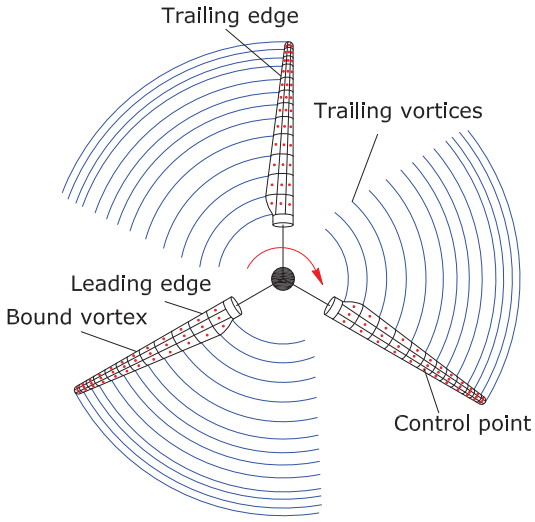

Figure 3.8: Schematic of vortex lattice prescribed wake

The vortex lattice method (VLM) is based on the thin lifting surface theory of vortex ring elements [40], where the blade surface is replaced by vortex panels that are constructed based on the airfoil camber line of each blade section (see fig.(3.9)). In order to take into account the blade

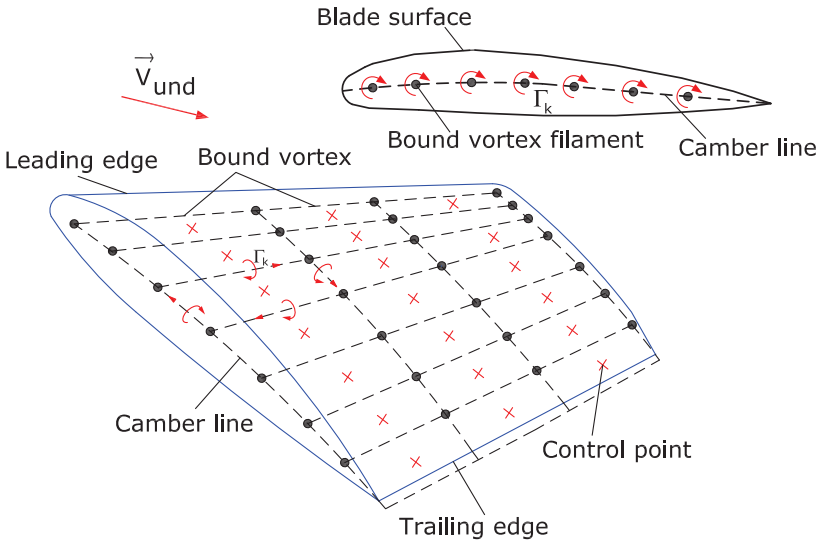

Figure 3.9: Lifting surface and vortex panels construction

surface curvature, the lifting surface is divided into a number of panels both in the chordwise and spanwise directions, where each panel contains the vortex ring with strength Γ_{ij} in which i and j indicate panel indices in the chordwise and spanwise directions, respectively. The strength of each blade bound vortex ring element, $\Gamma_{i,j}$, is assumed to be constant and the positive circulation is defined on the basis of right-hand rotation rule.

In order to fulfill the 2D Kutta condition, the leading segment of a vortex ring is located at the $1/4$ panel length (see fig.(3.10)) and the control point of each panel is located at the $3/4$ panel

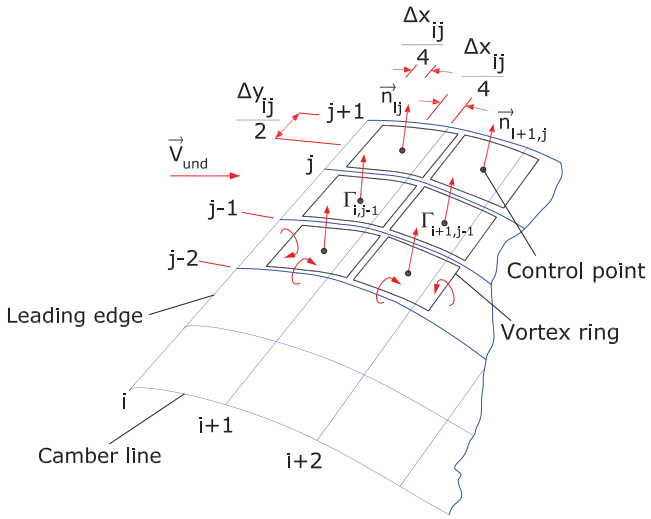

Figure 3.10: Numbering procedure

length meaning that the control point is placed at the center of the panel's vortex ring. Also, to

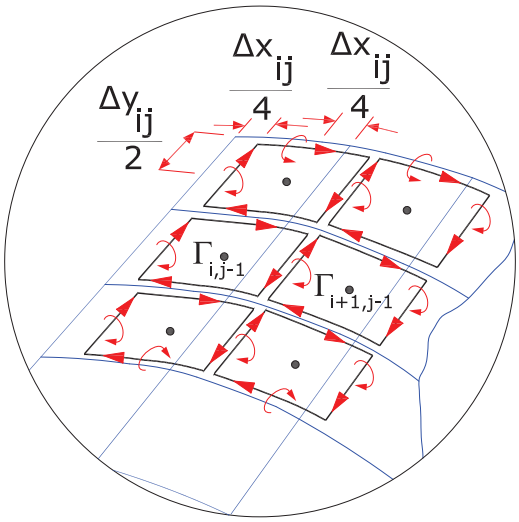

Figure 3.11: Blade panels (blue line) and vortex ring elements (black line)

satisfy the 3D trailing edge condition for each spanwise section, the strength of the trailing vortex wake rings must be equal to the last vortex ring row in the chordwise direction ($\Gamma_{T.E.} = \Gamma_{Wake}$) (see fig.(3.12)). The normal vector at each control point must be defined in order to apply the zero normal flow boundary condition across the blade, where, according to fig.(3.13), the control point and the normal unit vector are defined as

$$\mathbf{x}_{cp} = \frac{1}{4}\left(\mathbf{x}_{i,j} + \mathbf{x}_{i+1,j} + \mathbf{x}_{i,j+1} + \mathbf{x}_{i+1,j+1}\right) \tag{3.25}$$

$$\mathbf{n} = \mathbf{a} \times \mathbf{b} \tag{3.26}$$

Similar to the previous approach in section 3.1, an iterative method is used in the prescribed

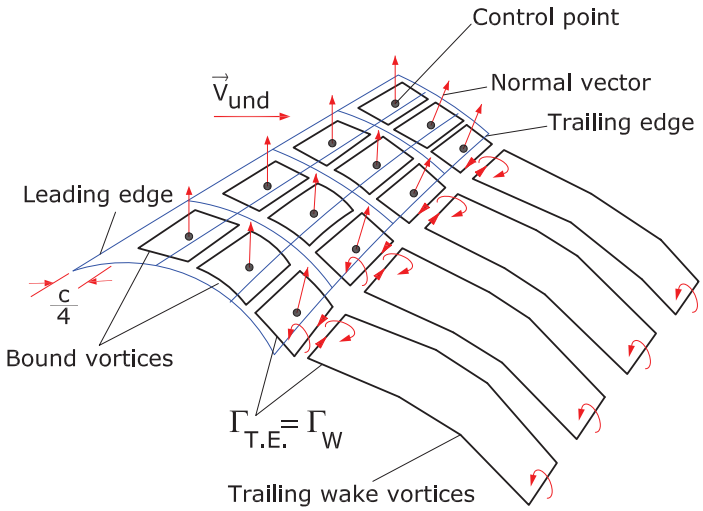

Figure 3.12: Kutta condition at the trailing edge

vortex lattice model, where an initial helical wake geometry based on eq.(3.7) is constructed and the trailing vortices are divided into a number of small segments.

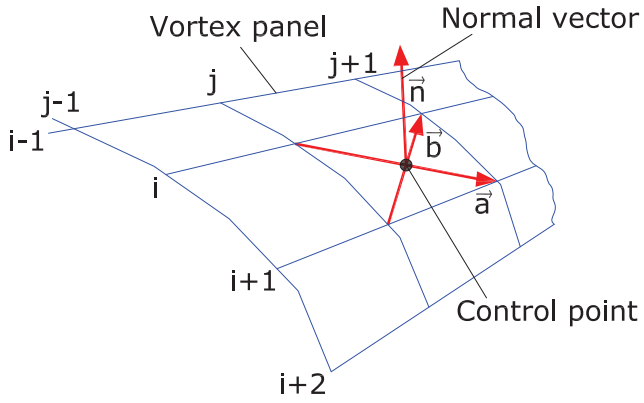

Figure 3.13: Normal vector definition

Generally, the wake vortices are modeled as vortex ring elements that are trailed from the trailing edge and induce the velocity field around the blade (see fig.(3.14), part I). The upstream flow in the prescribed vortex lattice method is assumed to be steady (no time variation), so the blade bound vortices' strength does not change in time; as a consequence, the strength of the trailing wake vortices remains constant for each blade section meaning that the wake vortex ring elements are converted to the horseshoe trailing vortices similar to the prescribed lifting line approach (see fig.(3.14, part III)). As mentioned in the theory section, the vortex flow is known as an incompressible, irrotational and inviscid flow where the solution of Laplace's equation with a suitable boundary condition gives the velocity field. The required boundary condition is zero normal flow across the blade surface, $\nabla(\Phi + \Phi_\infty) \cdot \mathbf{n} = 0$, where Φ and Φ_∞ denote the velocity potential due to the solid boundary and free stream flow, respectively [40]. This means that the sum of the wall-normal velocity components at each control point, including the induced velocity by the bound and trailing wake vortices as well as the free stream and rotational velocity, must be

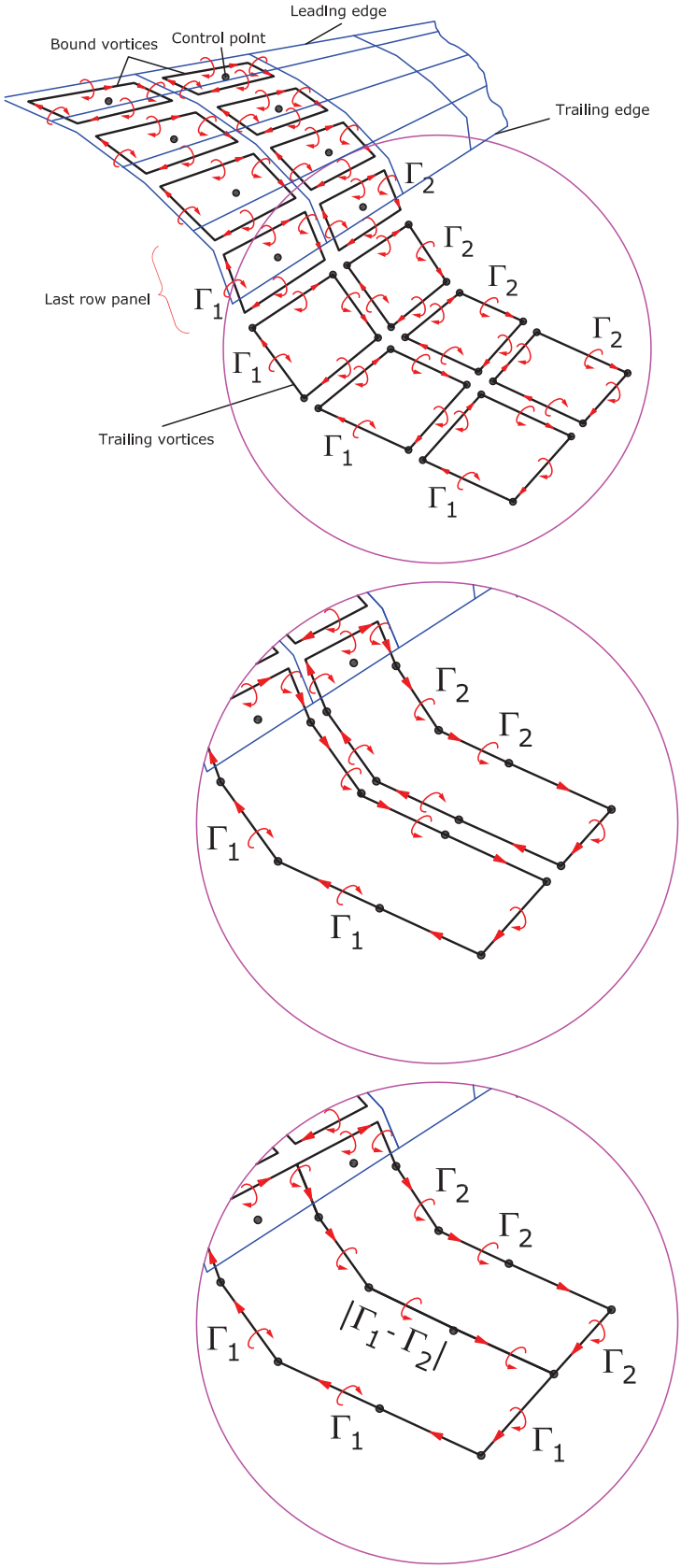

Figure 3.14: Schematic for trailing vortices, Part *I*: above, Part *II*: middle, Part *III*: bottom

zero, i.e. $\left(\mathbf{V}_{ind,bound}+\mathbf{V}_{ind,wake}+\mathbf{V}_{\infty}+\Omega\mathbf{r}\right)\cdot\mathbf{n}=0$. By applying this condition at each control point on the blade surface, a system of equations is constructed as

$$\begin{pmatrix} a_{11} & a_{12} & \cdots & a_{1m} \\ a_{21} & a_{22} & \cdots & a_{2m} \\ \vdots & \vdots & \ddots & \vdots \\ a_{m1} & a_{m2} & \cdots & a_{mm} \end{pmatrix} \begin{pmatrix} \Gamma_1 \\ \Gamma_2 \\ \vdots \\ \Gamma_m \end{pmatrix} = \begin{pmatrix} -(\mathbf{V}_{\infty}+\Omega\mathbf{r})\cdot\mathbf{n_1} \\ -(\mathbf{V}_{\infty}+\Omega\mathbf{r})\cdot\mathbf{n_2} \\ \vdots \\ -(\mathbf{V}_{\infty}+\Omega\mathbf{r})\cdot\mathbf{n_m} \end{pmatrix} \tag{3.27}$$

where a_{ij} and $\mathbf{n_i}$ denote the influence coefficient of the j^{th} blade vortex ring on the i^{th} blade control point and the unit vector normal of i^{th} blade control point, respectively. Here, the influence coefficient is defined as the induced velocity of a vortex ring with a strength equal to one on an arbitrary blade control point. Therefore, the influence coefficients of all vortex ring elements (blade surface and wake) on an arbitrary control point are evaluated.

This procedure is repeated for all control points on the blade with an M spanwise and an N chordwise section where $m = M \times N$. The solution of eq.(3.27) gives the strength of all vortex ring elements on the blade, $\Gamma_{i,j}$, where the strength of the last vortex ring row of each blade section determines the wake vortex ring strength, which makes it possible to calculate the wake induced velocity on the blade control points.

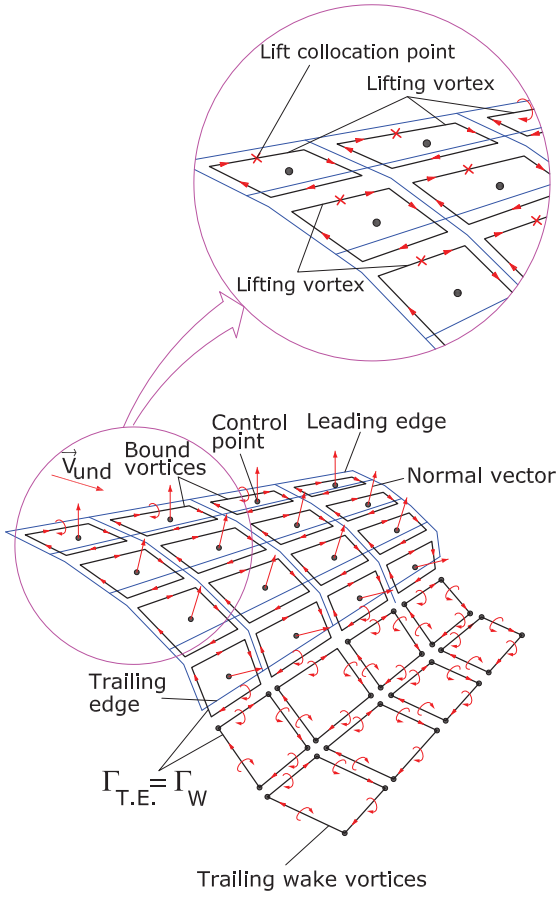

Figure 3.15: Lift collocation point

The Kutta-Jukowski theorem is applied at the mid point of the front edge of each blade vortex ring (see fig.(3.15)) and gives the potential lift force where the lift force of each spanwise blade

section is calculated by summing up the lift force of all panels along the chord. The lift force for each blade panel except the first row near the leading edge is computed by

$$\mathbf{L}_{i,j} = \rho \mathbf{V}_{tot,i,j} \times \left(\Gamma_{i,j} - \Gamma_{i-1,j}\right) \Delta \mathbf{y}_{i,j} \tag{3.28}$$

and, for the blade panels in the vicinity of the leading edge, eq.(3.28) can be written as

$$\mathbf{L}_{1,j} = \rho \mathbf{V}_{tot,1,j} \times \Gamma_{1,j} \Delta \mathbf{y}_{1,j} \tag{3.29}$$

where $\mathbf{V}_{tot,i,j}$ is computed as

$$\mathbf{V}_{tot,i,j} = \mathbf{V}_{und,i,j} + \mathbf{V}_{ind,wake,i,j} + \mathbf{V}_{ind,bound,i,j} \tag{3.30}$$

The total lift of each blade section in the spanwise direction can be written as

$$\mathbf{L}_j = \sum_{i=1}^{N} \mathbf{L}_{i,j} \tag{3.31}$$

where N denotes the number of spanwise sections. Decomposition of the lift force for each blade spanwise section into the normal and tangential directions with respect to the rotor plane (see fig.(3.16)) gives the effective angle of attack for each section.

$$\alpha_{eff} = tan^{-1}\left(F_t / F_n\right) - \theta_t - \theta_p \tag{3.32}$$

where α_{eff}, F_t, F_n, θ_t and θ_p represent the effective angle of attack, tangential force, normal force, blade section twist and blade pitch, respectively.

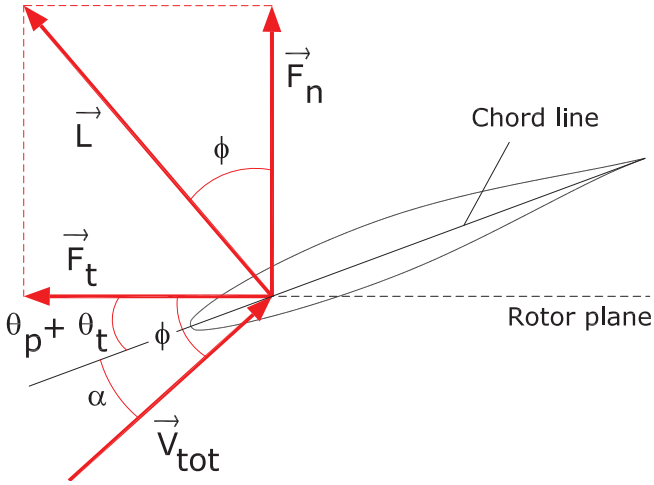

Figure 3.16: Potential load decomposition

Since the velocity field induced by the blade bound vortices and the vortex wake elements on the rotor blade change the lift force distribution over the blade in each iteration, the wake geometry can be updated by

$$\begin{aligned} x &= r cos\left(\Omega t + \theta_0\right) \\ y &= r sin\left(\Omega t + \theta_0\right) \\ z &= tan\phi_{eff} \Omega r t \end{aligned} \tag{3.33}$$

where r, Ω, θ_0, ϕ_{eff} and t denote the rotor section radius, rotor blade rotational velocity, blade initial angle, flow angle and time, respectively, and the effective flow angle (ϕ_{eff}) is defined as

$$\phi_{eff} = tan^{-1}(F_t/F_n) \tag{3.34}$$

It is worth mentioning that the forces acting on the rotor blades represent the integral effect of the induced velocity where it alternatively can be used to compute the flow angle of the trailing edge. Since the tangential and normal forces along the blade change with respect to the lift variation due to updating the wake geometry, the power and thrust are calculated in each iteration like the prescribed lifting line by using eqs.(3.21) and (3.23). The generated power is set as the criterion for fulfilling the convergency criterion, which means that the difference value of calculated power between the two consequent iterations must be lower than 0.0001, as eq.(3.24) and the iteration procedure are finished when the convergency criterion is satisfied.

3.3 Vortex Lattice Free Wake

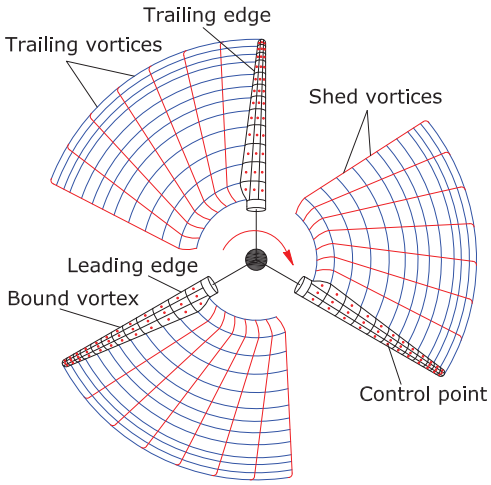

Figure 3.17: Schematic of vortex lattice free wake

This method is similar to the vortex lattice prescribed wake where the blade is represented as the lifting surface constructed on the basis of the camber line of each blade airfoil profile and consists of a number of vortex ring elements both in the spanwise and the chordwise directions, including a control point inside of each vortex panel. The major difference between the free wake vortex lattice method and the prescribed vortex lattice method is that the wake geometry is not prescribed and the wake elements are trailed and shed based on the time-marching method. Similar to the prescribed vortex lattice method, the solution of Laplace's equation with a proper

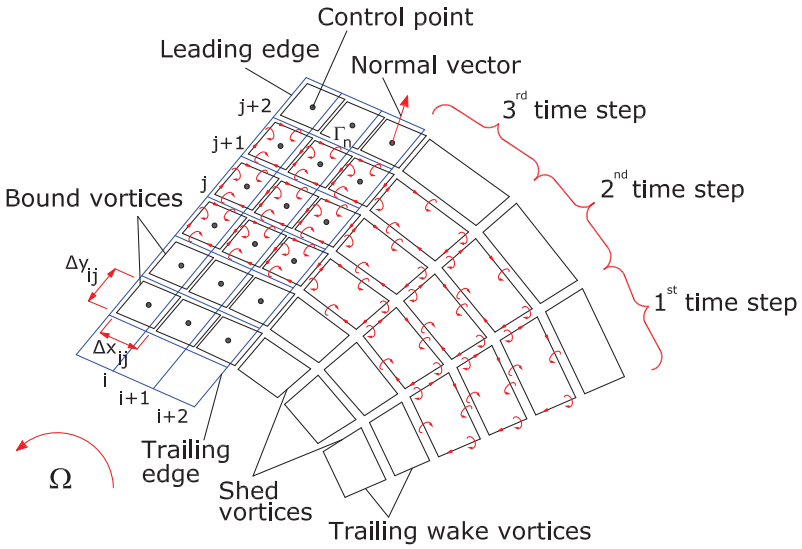

Figure 3.18: Schematic of blade and wake vortex panels

boundary condition gives the inflow around the blade resulting in an aerodynamic load calculation, generated power and thrust of the wind turbine. In the free wake vortex lattice method, there is a small difference when setting up the system of equations for calculating the blade bound vortex circulation in comparison with the prescribed vortex lattice method. To find the blade bound

vortices' strength, the flow tangency condition at each blade control point must be specified by establishing a system of equations. The velocity components at each blade control point includes the free stream ($\mathbf{V}_\infty$), rotational ($\mathbf{\Omega r}$), blade vortex rings self-induced ($\mathbf{V}_{ind,bound}$) and wake induced ($\mathbf{V}_{ind,wake}$) velocities. The blade self-induced component is known as influence coefficient a_{ij} and is defined in a way similar to that in the prescribed vortex lattice method as the induced velocity of a j^{th} blade vortex ring with a strength equal to one on the i^{th} blade control point. If the blade is assumed to be rigid, then the influence coefficients are constant at each time step, which means that the left-hand side of the equation system is computed only once. However, if the blade is modeled as a flexible blade, they must be calculated at each time step. Since the wind and rotational velocities are known during the wind turbine operation, they are transferred to the right-hand side of the equation system. In addition, at each time step, the strength of the wake vortex panels is known from the previous time step, so the induced velocity contribution by wake panels is also transferred to the right-hand side. Therefore, the system of equations can be expressed as

$$\begin{pmatrix} a_{11} & a_{12} & \cdots & a_{1m} \\ a_{21} & a_{22} & \cdots & a_{2m} \\ \vdots & \vdots & \ddots & \vdots \\ a_{m1} & a_{m2} & \cdots & a_{mm} \end{pmatrix} \begin{pmatrix} \Gamma_1 \\ \Gamma_2 \\ \vdots \\ \Gamma_m \end{pmatrix} = \begin{pmatrix} RHS_1 \\ RHS_2 \\ \vdots \\ RHS_m \end{pmatrix} \tag{3.35}$$

where m is defined as $m = M \times N$ for a blade with an M spanwise and an N chordwise section and the right-hand side is computed as

$$RHS_k = -\left(\mathbf{V}_\infty + \mathbf{\Omega r} + \mathbf{V}_{ind,wake}\right)_k \cdot \mathbf{n}_k \tag{3.36}$$

where $\mathbf{V}_\infty$, $\mathbf{\Omega r}$ and $\mathbf{V}_{ind,wake}$ are the velocity components by the wind flow, the blade rotation and the wake panels induced velocities, respectively, which are known at each time step. The blade bound vortex strength ($\Gamma_{i,j}$) is calculated by solving eq.(3.35) at each time. At the first time

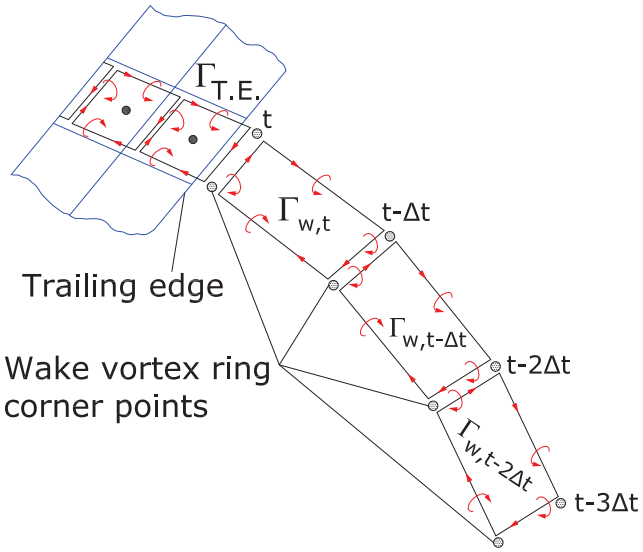

Figure 3.19: Schematic of generation and moving of wake panels at each time step

step (see fig.(3.20)), there are no free wake elements. The strength of the blade vortex rings is determined by applying the zero normal flow boundary condition on all blade control points. At

the second time step (see fig.(3.21)), when the blade is rotating, the first wake panels are shed. Their strength is equal to the bound vortex circulation of the last row of the blade vortex ring elements (Kutta condition), located at the trailing edge, at the previous time step, which means that $\Gamma_{W_{t_2}} = \Gamma_{T.E.,t_1}$, where the W and $T.E.$ subscripts represent the wake and the trailing edge, respectively. At the second time step, the strength of the blade bound vortex rings is calculated by specifying the flow tangency boundary condition where, in addition to the blade vortex ring elements, the contribution of the first row of the wake panels is considered.

This methodology is repeated, and the vortex wake elements are trailed and shed at each time step, where their strengths remain constant (Kelvin theorem) and their corner points are moved based on the governing equation (eq.(3.37)) by the local velocity field, including the wind velocity and the induced velocity by all blade and wake vortex rings (see fig.(3.22) and fig.(3.23)). The

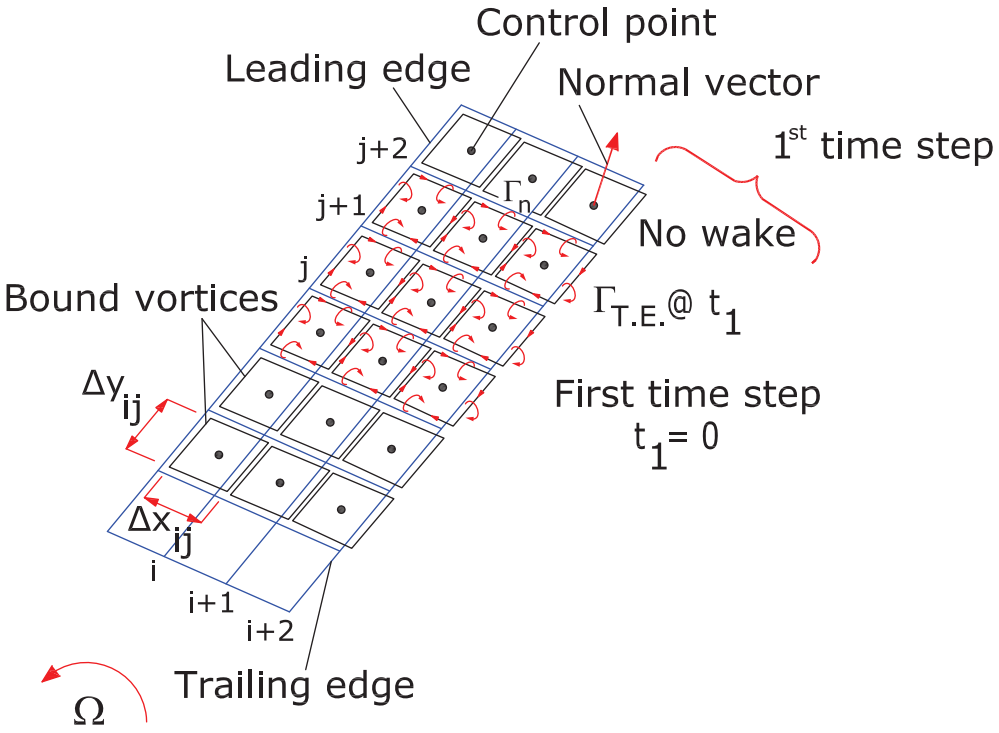

Figure 3.20: Schematic of wake evolution at the first time step

governing equation for the wake geometry is

$$\frac{d\mathbf{r}}{dt} = \mathbf{V}(\mathbf{r},t) \qquad \mathbf{r}(t=0) = \mathbf{r_0} \tag{3.37}$$

where $\mathbf{r}$, $\mathbf{V}$ and t denote the position vector of a Lagrangian marker, the total velocity field and time, respectively, and the total velocity field can be written as

$$\mathbf{V} = \mathbf{V}_\infty + \mathbf{V}_{ind,blade} + \mathbf{V}_{ind,wake} \tag{3.38}$$

Different numerical schemes may be used for eq.(3.37) such as the explicit Euler method, the implicit method, the Adams-Bashforth method and the Predictor-Corrector method. The numerical integration scheme must be considered in terms of the accuracy, stability and computational efficiency. The Euler explicit method is the first-order scheme stated as

$$\mathbf{r}_{t+1} = \mathbf{r}_t + \mathbf{V}(\mathbf{r}_t)\,\Delta t \tag{3.39}$$

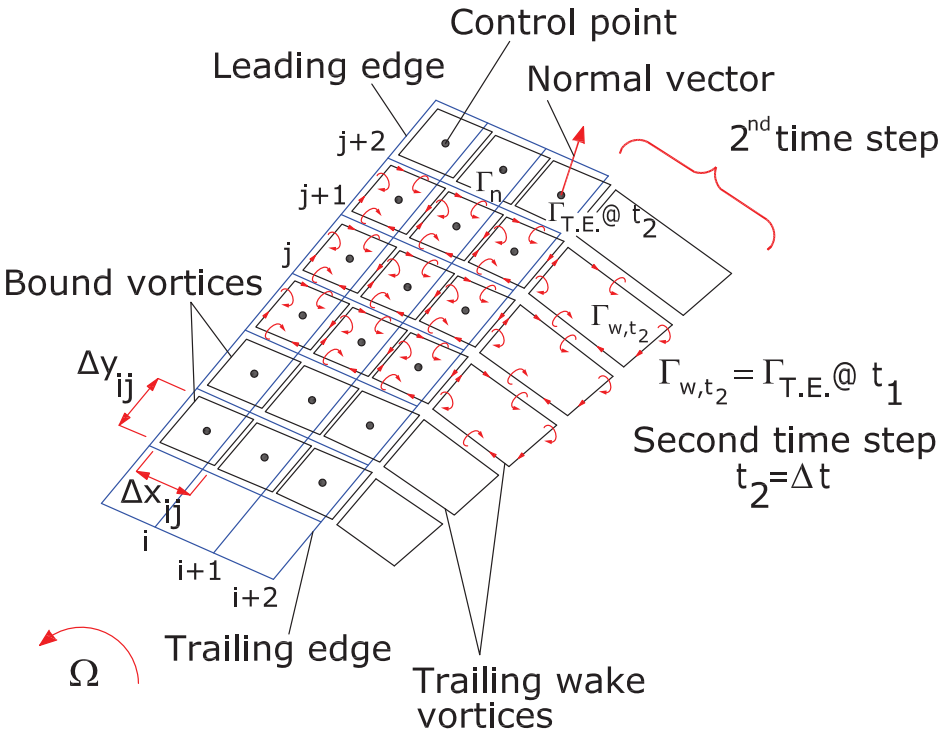

Figure 3.21: Schematic of wake evolution at the second time step

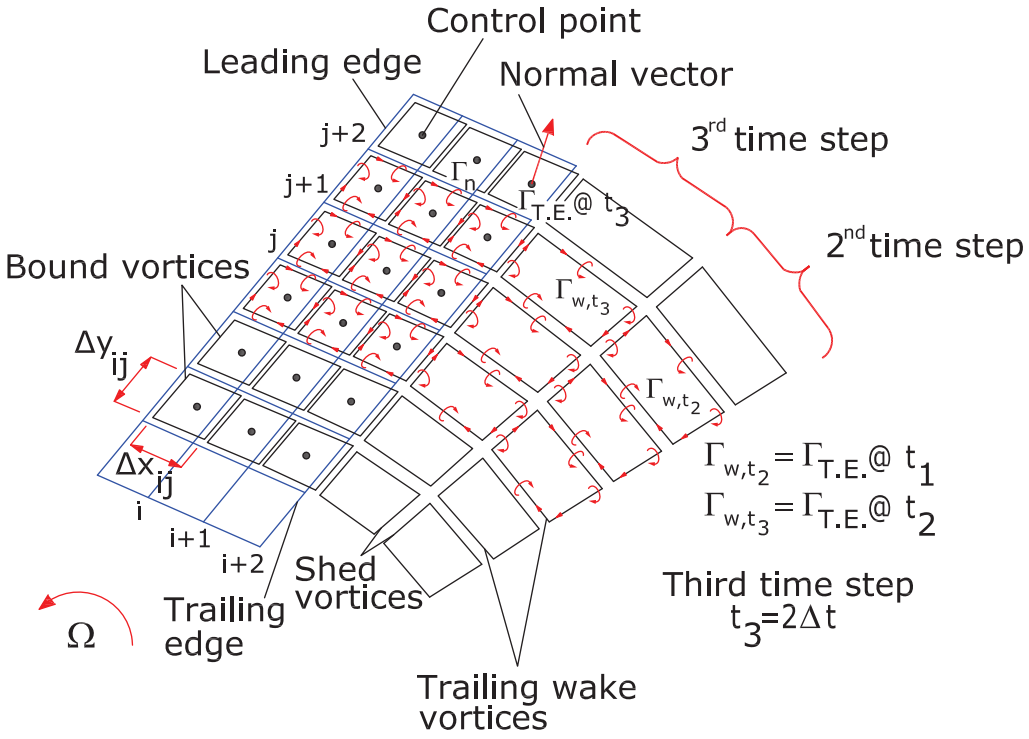

Figure 3.22: Schematic of wake evolution at the third time step

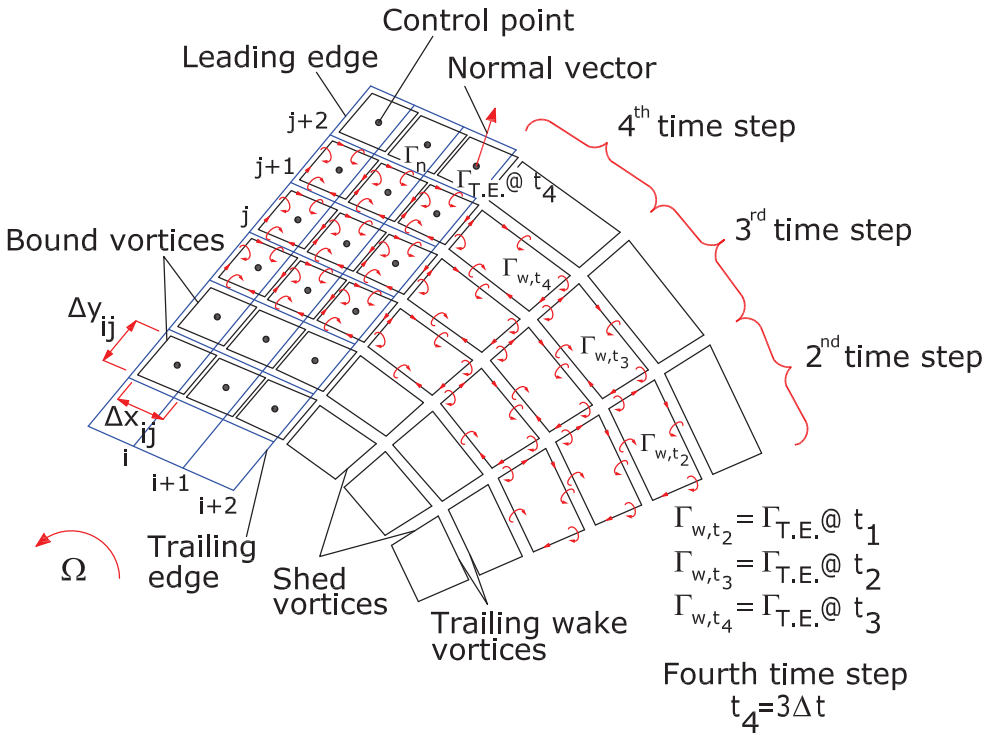

Figure 3.23: Schematic of wake evolution at the fourth time step

According to the linear stability analysis done by Gupta [41], the Euler explicit method is considered to be an unstable integration scheme. Small time steps can be used to improve the stability of this scheme, but the very fine wake discretization, for example $2-6$ degrees of azimuth, makes the free wake method computationally expensive.

The implicit scheme for a rotor wake application is defined as

$$\mathbf{r}_{t+1} = \mathbf{r}_t + \mathbf{V}(\mathbf{r}_{t+1})\,\Delta t \tag{3.40}$$

which is a stable numerical method. Since this method needs information from the current time step, a set of linear equations must be solved in each time step, which makes it computationally too expensive and impractical for the free wake method.

Higher order accurate schemes may be also used, such as the 2^{nd} order Adams-Bashforth

$$\mathbf{r}_{t+2} = \mathbf{r}_{t+1} + \frac{1}{2}\left(3\mathbf{V}(\mathbf{r}_{t+1}) - \mathbf{V}(\mathbf{r}_t)\right)\Delta t \tag{3.41}$$

Similar to the Euler explicit method, this scheme is numerically unstable for rotor wake applications [41].

The predictor-corrector scheme is well known as a numerical scheme that improves the stability of the explicit method. In the predictor step, the Euler explicit method is used to get an intermediate solution for the Lagrangian markers' position. The velocity field in the corrector step is calculated on the basis of the position of Lagrangian markers computed in the predictor step. Mathematically, the predictor step is defined as

$$\overline{\mathbf{r}}_{t+1} = \mathbf{r}_t + \mathbf{V}(\mathbf{r}_t)\,\Delta t \tag{3.42}$$

and the corrector step becomes

$$\mathbf{r}_{t+1} = \mathbf{r}_t + \mathbf{V}\left(\overline{\mathbf{r}}_{t+1}\right)\Delta t \tag{3.43}$$

The drawback of the predictor-corrector scheme is that it requires two velocity field calculations in each time step.

In each time step, when the position of all the Lagrangian markers is calculated, we are able to compute the velocity field around the rotor blade where, as a consequence, similar to the prescribed vortex lattice method, the lift force can be calculated according to the Kutta-Jukowski theorem (see eqs. 3.28, 3.29, 3.30 and 3.31). Decomposition of the lift force of each spanwise section with respect to the rotor plane is used to find the effective angle of attack according to eq.(3.32). Further, the generated power and thrust are determined by eqs.(3.21), (3.23).

The convergency of the time-marching free wake is obtained on the basis of the steady state wake geometry known as the periodic solution. To reach a periodic solution, the free wake should run for many time steps. However, a periodic solution may not be achieved for some upstream flow conditions [42].

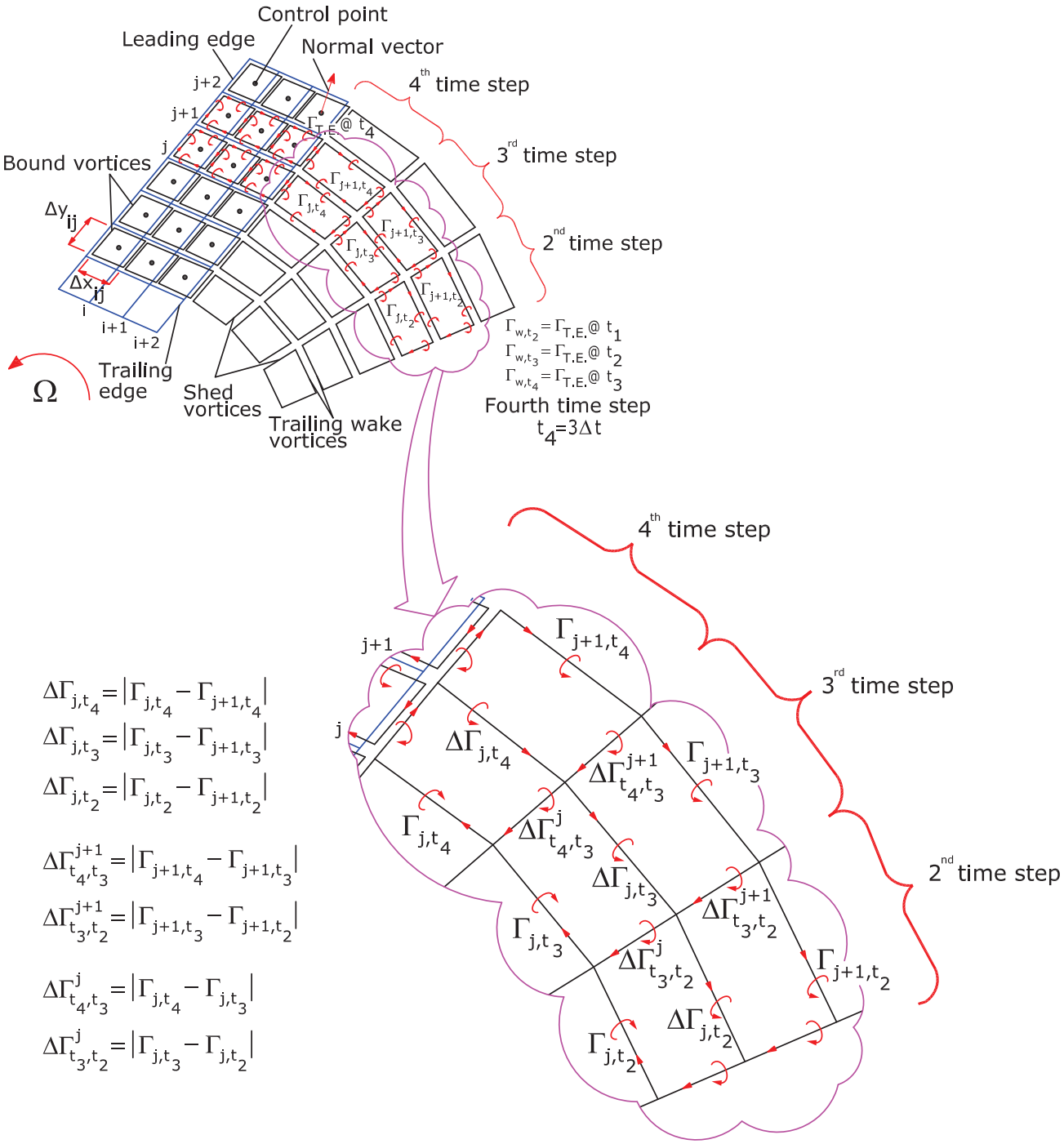

$$\Delta\Gamma_{j,t_4} = \left|\Gamma_{j,t_4} - \Gamma_{j+1,t_4}\right|$$
$$\Delta\Gamma_{j,t_3} = \left|\Gamma_{j,t_3} - \Gamma_{j+1,t_3}\right|$$
$$\Delta\Gamma_{j,t_2} = \left|\Gamma_{j,t_2} - \Gamma_{j+1,t_2}\right|$$

$$\Delta\Gamma^{j+1}_{t_4,t_3} = \left|\Gamma_{j+1,t_4} - \Gamma_{j+1,t_3}\right|$$
$$\Delta\Gamma^{j+1}_{t_3,t_2} = \left|\Gamma_{j+1,t_3} - \Gamma_{j+1,t_2}\right|$$

$$\Delta\Gamma^{j}_{t_4,t_3} = \left|\Gamma_{j,t_4} - \Gamma_{j,t_3}\right|$$
$$\Delta\Gamma^{j}_{t_3,t_2} = \left|\Gamma_{j,t_3} - \Gamma_{j,t_2}\right|$$

Figure 3.24: Schematic of wake strength at each time step

Chapter 4

Results

As stated before, the proper combination of the blade and wake models in the vortex method application for the performance of a wind turbine is crucial. Here, the different parameters for both the blade and the wake are studied, where there should be a reasonable balance between the accuracy and the computational time.

In the lifting line prescribed wake model, since the blade is represented as a vortex line, only the number of spanwise sections must be investigated. In contrast, in the vortex lattice prescribed wake and the vortex lattice free wake, since the blade is modeled as a lifting surface, the number of both spanwise and chordwise sections must be studied. For all the different approaches, the wake geometry is divided into a number of straight vortex wake elements, where it has a great influence on the flow field. Therefore, the number of vortex filament segments (wake azimuthal angle) per wake revolution must be studied. Another parameter that must be studied is the wake length. Recalling that the vortex method is based on the potential flow, which means that, in the absence of the viscosity, the trailing wake vortices are not dissipated and they extend to infinity. For computational efficiency, the computations are done for a limited wake length.

Finally, the different approaches are compared with the BEM method, GENUVP [12], and the NREL technical report [43]. The $5MW$ reference wind turbine [43] is used, and the operating conditions for all computations in this chapter are $\mathbf{V}_\infty = 8.0\ [m/s]$ and $\Omega = 1.0032\ [rad/s]$ as the uniform and steady free stream and constant rotational velocity, respectively. More information about the blade properties of the $5MW$ reference wind turbine can be found in [43].

4.1 Lifting Line Prescribed Wake

This section presents the effect of the number of blade spanwise sections, the number of the wake segmentations and the wake length for the lifting line prescribed wake. Calculations are made based on one wake revolution and 10 degrees of azimuth segmentation for the first two. The effect of the wake length is evaluated based on the conclusion of the first two parts.

4.1.1 Blade spanwise section

Table (4.1) shows the comparison between the generated power and the thrust for different numbers of equally spaced blade span wise sections. The error of the generated power and the thrust for 25 sections is around 2% and 0.001%, respectively which may be seen as a suitable resolution with regard to the accuracy and computational time efficiency. By increasing the number of span-

No. of spanwise section	Power [MW]	error [%]	Thrust [kN]	error [%]
10	1.927	7.136	405.66	0.014
15	1.978	4.674	401.95	0.005
25	2.032	2.088	399.61	0.001
35	2.064	0.546	400.12	7.78E-6
45	2.074	0.024	400.29	4.33E-4
50	2.075	—	400.12	—

Table 4.1: Power and thrust error for the different number of blade spanwise sections

wise sections, the generated power and the thrust errors decrease; however, the fine resolution increases the computational time.

Figure (4.1) shows the distribution of the circulation (Γ) along the blade for the various numbers of the blade spanwise sections. It can be seen that the small number of the spanwise sections gives poor result for the circulation. At least 25 spanwise sections seem to fulfill the accuracy and the computational time efficiency requirements.

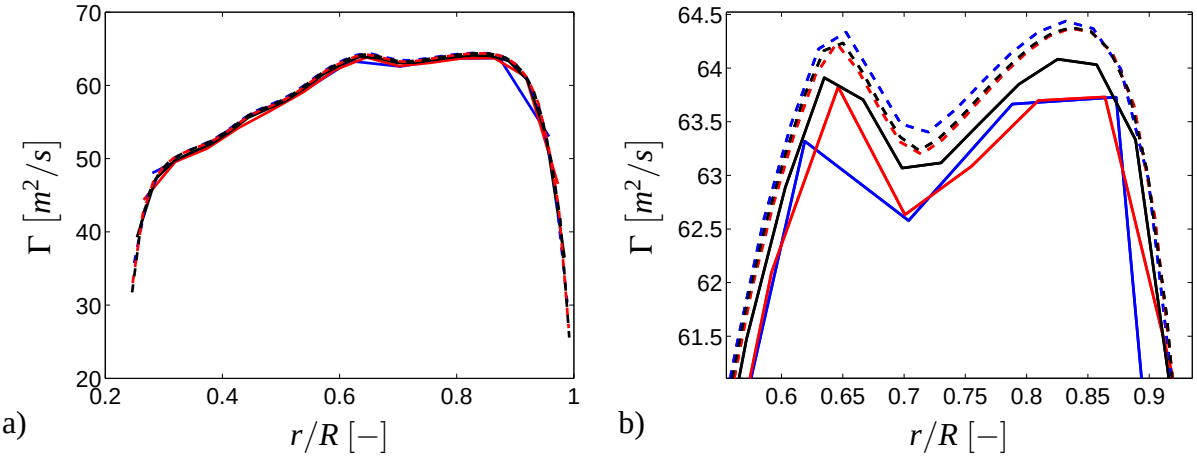

Figure 4.1: Distribution of the circulation along the blade, ——: 10 sections, ——: 15 sections, ——: 25 sections, - - - -: 35 sections, - - - -: 45 sections, - - - -: 50 sections

The distribution of the tangential force along the blade and the normal force per span length is shown in figs.(4.2) and (4.3), where they are converged for the 25 blade sections and more. As can be seen in fig.(4.4), the distribution of the angle of attack along the blade is highly dependent on the number of spanwise sections, and many spanwise sections lead to a smooth distribution of the angle of attack.

It is concluded that at least 25 sections along the blade distributed equally is enough for both the accuracy and computational time efficiency. However, because of the large circulation gradient near the root and the tip of the blade, especially near the tip, it is recommended that the number of spanwise sections be refined there. The refinement can be done on the basis of the Cosine method. This prevents the sudden jump in the circulation and increases the accuracy of the strength of the trailing wake vortices and the induced velocity field.

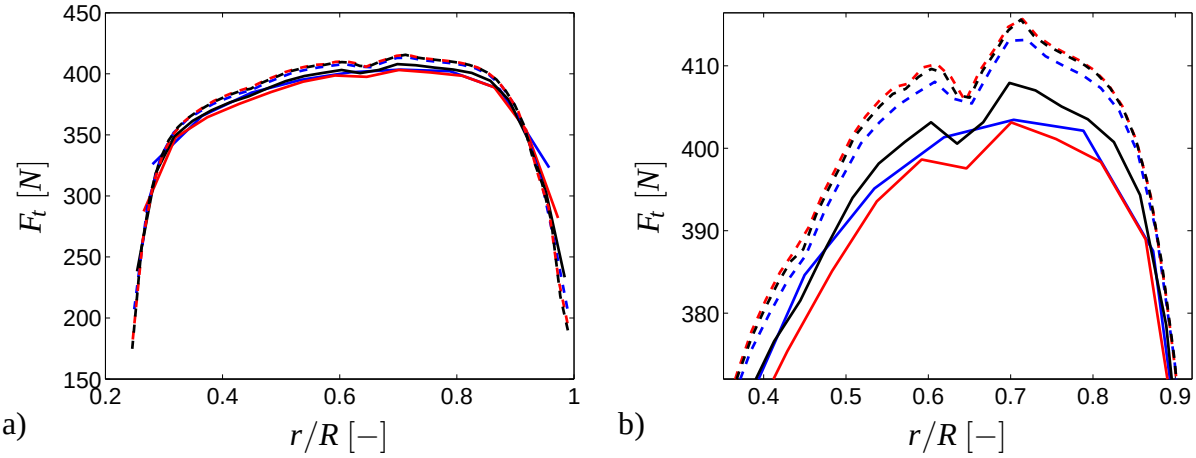

Figure 4.2: Distribution of the tangential force with respect to the rotor plane, ——: 10 sections, ——: 15 sections, ——: 25 sections, - - - -: 35 sections, - - - -: 45 sections, - - - -: 50 sections

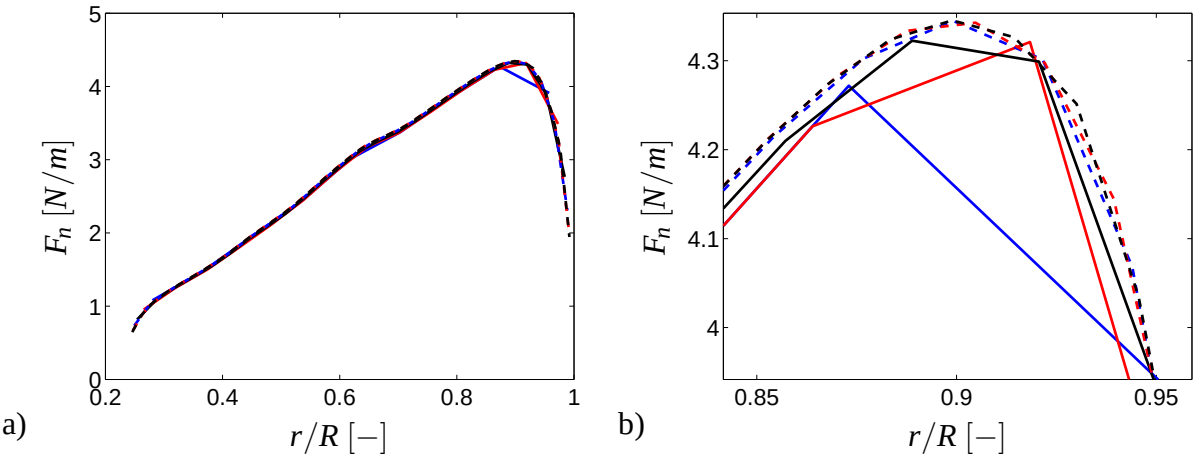

Figure 4.3: Distribution of the normal force with respect to the rotor plane, ——: 10 sections, ——: 15 sections, ——: 25 sections, - - - -: 35 sections, - - - -: 45 sections, - - - -: 50 sections

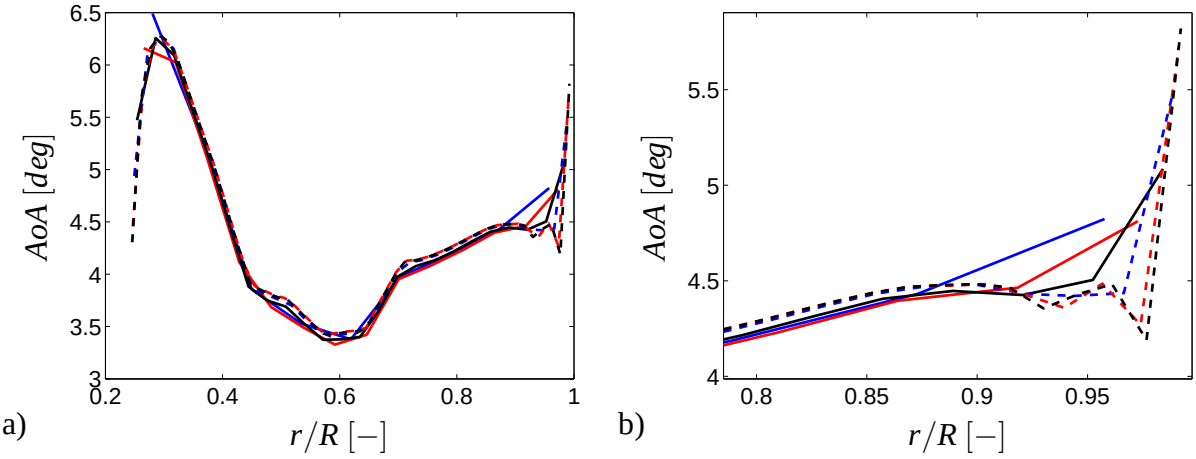

Figure 4.4: Distribution of the angle of attack along the blade, ——: 10 sections, ——: 15 sections, ——: 25 sections, - - - -: 35 sections, - - - -: 45 sections, - - - -: 50 sections

Wake azimuthal angle [deg]	Power [MW]	error [%]	Thrust [kN]	error [%]
2	2.064	—	402.386	—
5	2.052	0.056	401.373	0.252
10	2.032	1.542	399.612	0.689
15	2.009	2.661	397.600	1.189
20	1.986	3.746	395.628	1.679
30	1.938	6.104	391.274	2.762

Table 4.2: Power and thrust error for the different wake azimuthal angles

4.1.2 Wake azimuthal angle

Table (4.2) represents the power and the thrust by different wake segmentations from the finest resolution, 2 degrees, to the coarsest, 30 degrees, in the azimuthal direction. In both accuracy and computational time efficiency, 10 degrees shows an acceptable generated power and thrust error rate compared with the 2 degrees of azimuth segmentation. The data in table (4.2) are extracted on the basis of the one wake revolution and 25 equally spaced blade spanwise sections.

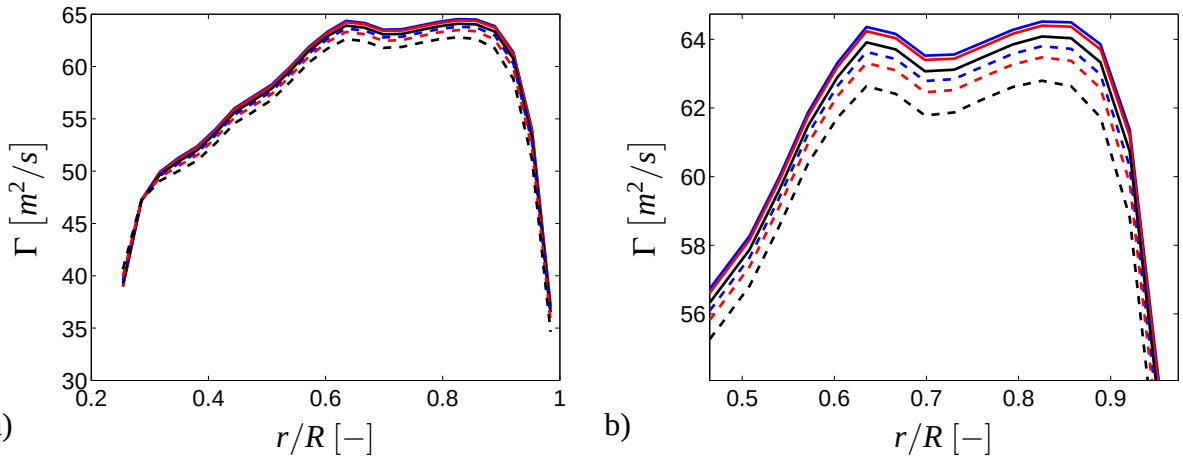

Figure 4.5: Distribution of the circulation along the blade, ——: 2 deg, ——: 5 deg, ——: 10 deg, - - - - - -: 15 deg, - - - - - -: 20 deg, - - - - - -: 30 deg

Figure 4.5 shows the distribution of the different wake azimuthal angle discretizations where the trailing wake vortices are divided into a number of straight vortex filaments. By increasing the number of wake segmentations, the accuracy of the induced velocity field is increased. However, the calculation of the Biot-Savart equation is increased dramatically which makes the model computationally expensive. The 10 degrees of azimuth resolution seem to be enough for the wake discretization.

The error rate of different wake azimuthal angle segmentations is calculated on the basis of the normalized root mean squared error (NRMSE) which is defined as

$$NRMSE = \frac{1}{x_{ref,max} - x_{ref,min}} \left(\frac{1}{n} \sum_{i=1}^{n} \left(x_{ref,i} - x_{model,i} \right)^2 \right)^{0.5} \tag{4.1}$$

where ref and n denote the reference values and number of samples, respectively.

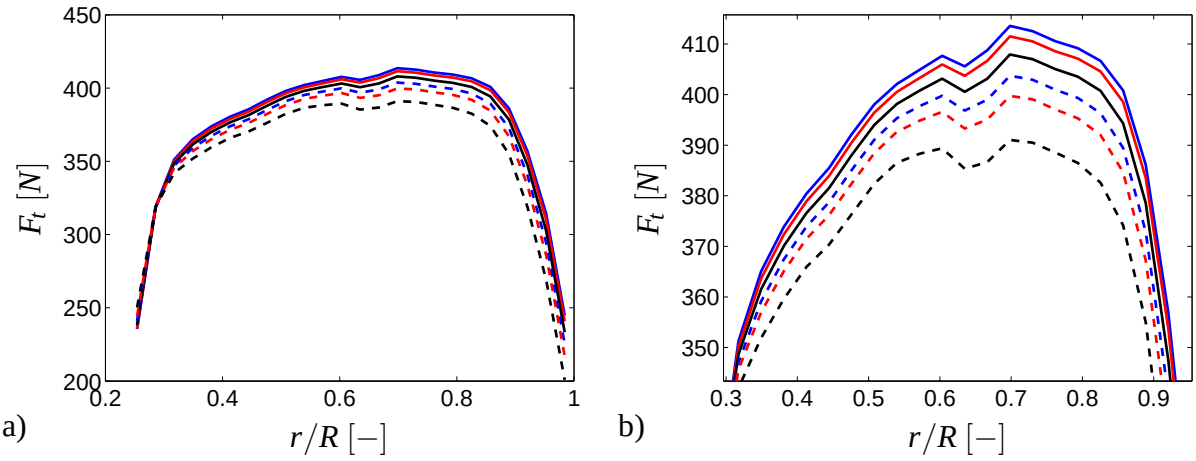

Figure 4.6: Distribution of the tangential force with respect to the rotor plane, ——: 2 deg, ——: 5 deg, ——: 10 deg, - - - -: 15 deg, - - - -: 20 deg, - - - -: 30 deg

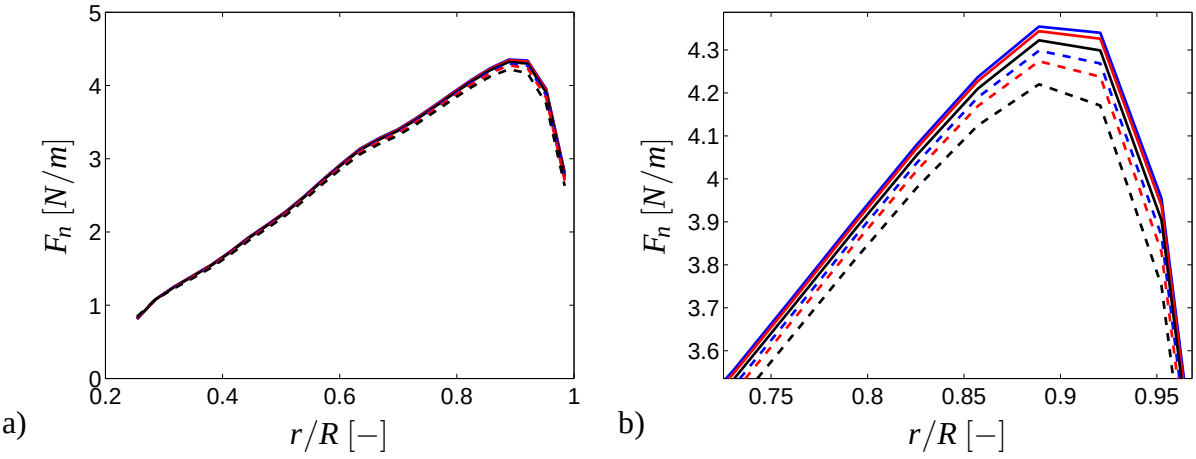

Figure 4.7: Distribution of the normal force with respect to the rotor plane, ——: 2 deg, ——: 5 deg, ——: 10 deg, - - - -: 15 deg, - - - -: 20 deg, - - - -: 30 deg

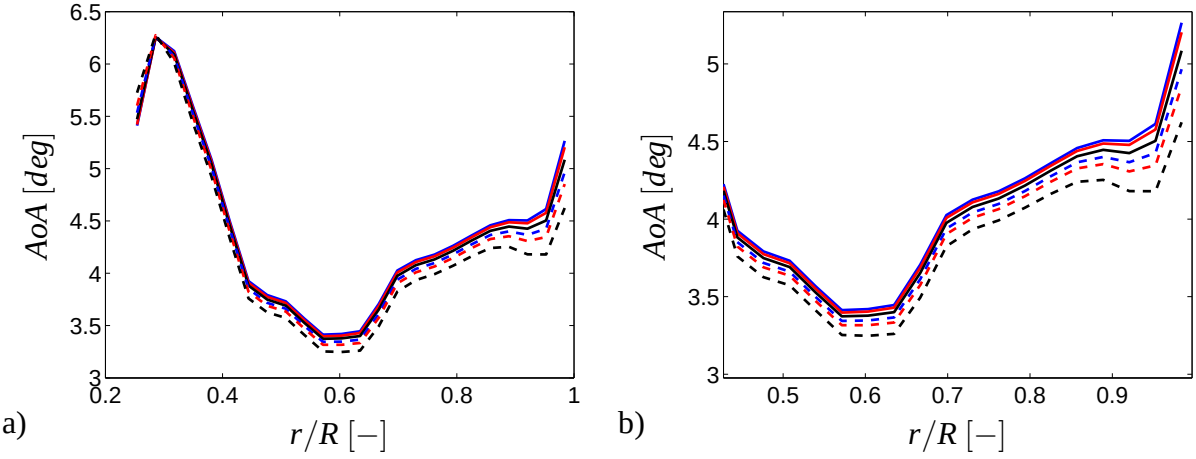

Figure 4.8: Distribution of the angle of attack along the blade, ——: 2 deg, ——: 5 deg, ——: 10 deg, - - - -: 15 deg, - - - -: 20 deg, - - - -: 30 deg

Wake azimuthal angle [deg]	NRMSE (Γ)	NRMSE (F_t)	NRMSE (F_n)	NRMSE (AoA)
2	—	—	—	—
5	0.005	0.012	0.002	0.008
10	0.016	0.034	0.007	0.022
15	0.026	0.057	0.012	0.037
20	0.038	0.079	0.017	0.051
30	0.061	0.122	0.028	0.081

Table 4.3: Normalized root-mean squared error for the different wake azimuthal angles

Wake length [m]	Power [MW]	error [%]	Thrust [kN]	error [%]
1D	2.032	13.109	399.612	5.986
2D	1.877	4.483	384.882	2.080
3D	1.830	1.856	380.301	0.864
4D	1.811	0.799	378.447	0.373
5D	1.802	0.321	377.605	0.150
6D	1.796	—	377.041	—

Table 4.4: Power and thrust error for the different wake lengths

Figures (4.6) and (4.7) show the tangential force and the normal force per span length along the blade. The results for the different wake azimuthal angle segmentations are converged where, according to table (4.3), the NRMSE of the tangential and normal forces for 10 deg of wake azimuth is negligible.

The effective angle of attack for the different wake discretization is shown in fig.(4.8), and the findings are similar to the previous results, where there is good convergency for the different number of vortex wake elements.

When the generated power and the thrust errors are less than 2% (see table 4.2), the NRMSE of different evaluated parameter is less than 0.05 (see table 4.3), which satisfies the accuracy and time efficiency.

4.1.3 Wake length

To decrease the computational time and inflow approximation, it is assumed that the trailing wake vortices are truncated after a specified length, which is normally measured based on the rotor blade diameter. Table (4.4) shows the thrust and the generated power for different wake lengths, where the blade consists of 25 equally spaced spanwise sections and the wake segmentation is equal to 10 degrees of azimuthal segmentation.

Figure (4.9) represents the circulation variation along the blade where, by increasing the wake length from one diameter ($1D$) to five diameters ($5D$), the circulation values are converged to a certain value.

The tangential and normal forces along the blade are shown in figs.(4.10) and (4.11). The effect of the wake length is obvious, as it gives quite a good prediction for $4D$ length and longer. As can be seen in fig.(4.12), after $4D$ wake length, the effective angle of attack does not change and, according to table (4.5), the NRMSE is around 0.01.

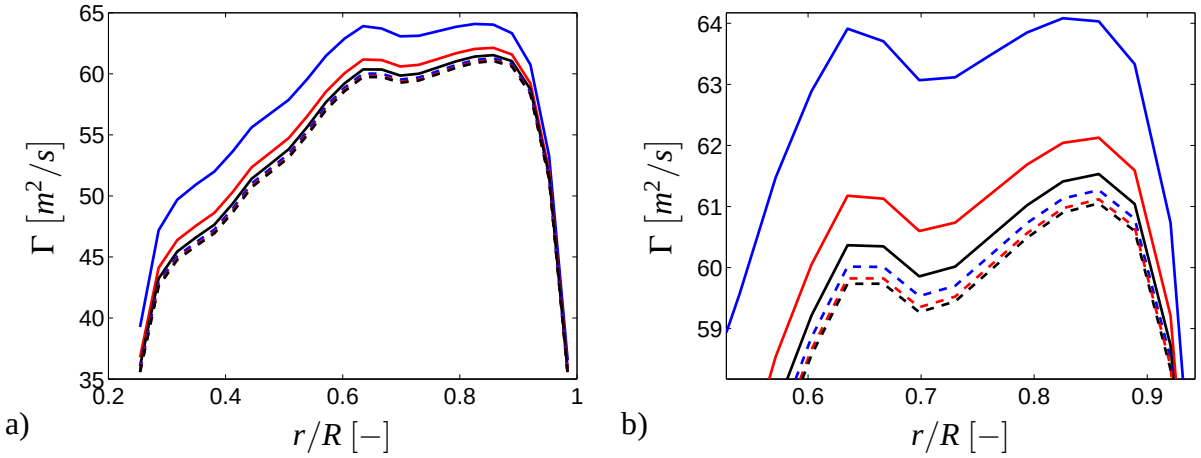

Figure 4.9: Distribution of the circulation along the blade, ——: 1D, ——: 2D, ——: 3D, ------: 4D, ------: 5D, ------: 6D

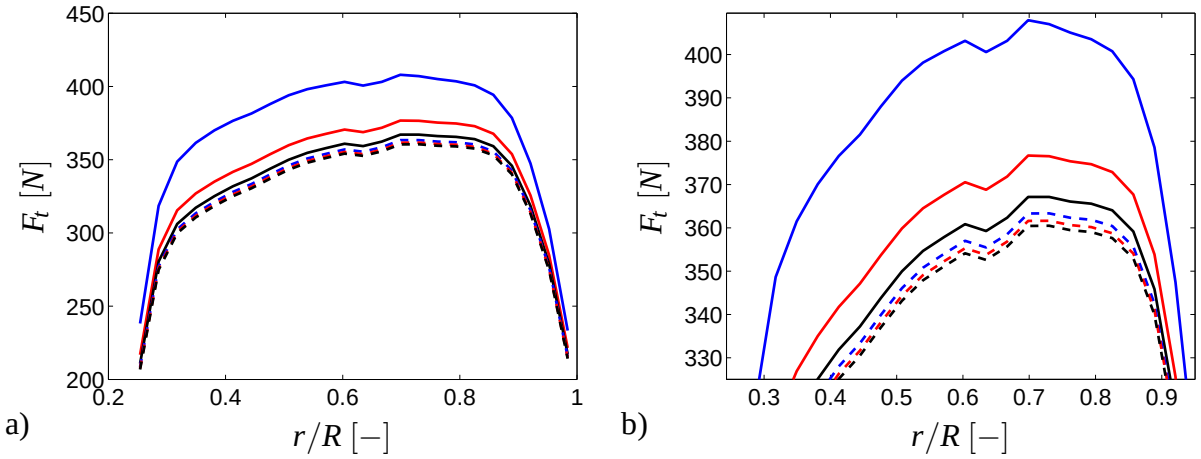

Figure 4.10: Distribution of the tangential force with respect to the rotor plane, ——: 1D, ——: 2D, ——: 3D, ------: 4D, ------: 5D, ------: 6D

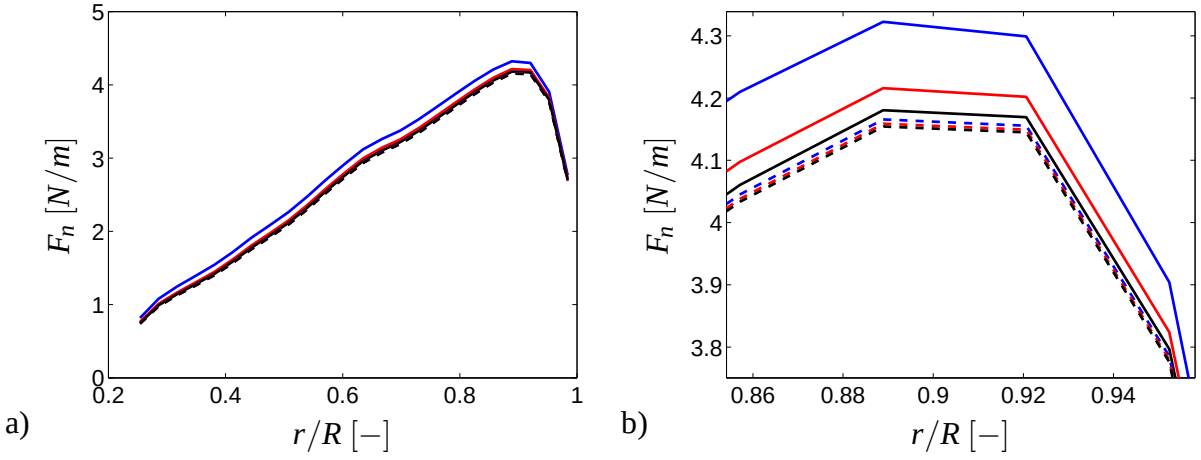

Figure 4.11: Distribution of the normal force with respect to the rotor plane, ——: 1D, ——: 2D, ——: 3D, ------: 4D, ------: 5D, ------: 6D

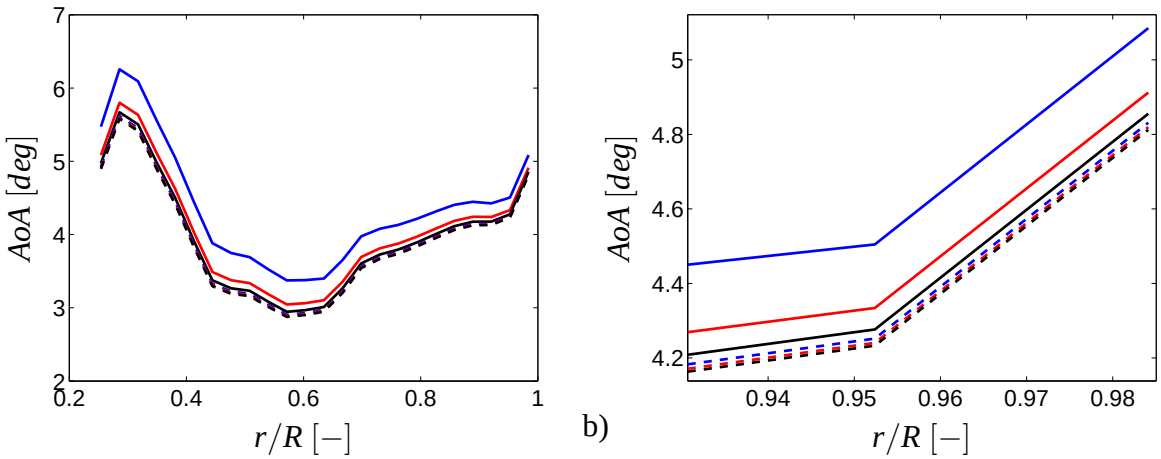

Figure 4.12: Distribution of the angle of attack along the blade, ——: 1D, ——: 2D, ——: 3D, - - - -: 4D, - - - -: 5D, - - - -: 6D

Wake length [m]	NRMSE (Γ)	NRMSE (F_t)	NRMSE (F_n)	NRMSE (AoA)
1D	0.146	0.258	0.046	0.170
2D	0.052	0.095	0.016	0.060
3D	0.023	0.040	0.007	0.025
4D	0.010	0.017	0.003	0.011
5D	0.003	0.007	0.001	0.004
6D	——	——	——	——

Table 4.5: Normalized root-mean squared error for the different wake lengths

It seems that the 4*D* wake length may be a good estimation for the wake truncation for the purpose of decreasing the computational time in parallel with a acceptable accuracy.

4.1.4 Modeling features

For the lifting line prescribed wake, different parameters such as number of blade spanwise sections, wake element discretization and the wake length were studied. It can be concluded that the 25 blade spanwise sections with fine resolution near the tip, 10 degrees in the azimuthal direction for the wake element segmentation and 4*D* wake length satisfy both the accuracy and time efficiency. The results of the simulation are shown below.

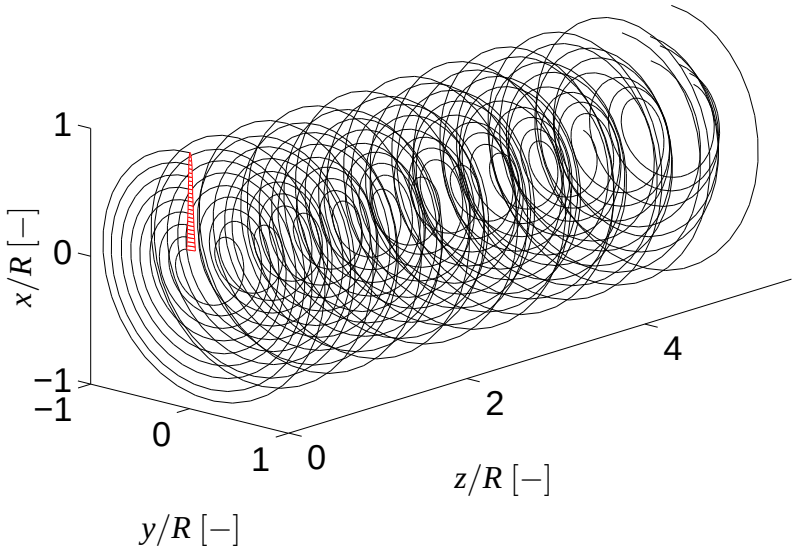

Figure 4.13: Lifting line prescribed wake. Wake geometry for one blade normalized by the blade radius

Figures (4.13), (4.14) and (4.15) represent the wake configuration by the lifting line prescribed wake for one blade. As can be seen, the wake moves forward around 2.5*D*, which means that the induced velocity field generated by the wake vortex filaments retards the wake motion compared to constant velocity equal to the upstream flow. It is obvious that all the trailing vortices are not moving downstream with the same axial velocity (here the axial direction is parallel to the *z* axis) which means that all the control points along the blade do not sense the same induced velocity and it varies from one control point to another. According to figs.(4.16) and (4.17), the tip vortex travels faster than the root vortex, implying that the induced velocity field is larger near the blade root than the blade tip and that it increases in the blade radial direction.

Note that there is no wake expansion in the blade radial direction since the wake travels downstream with constant radius in the prescribed wake model.

The tip and the root trailing wake vortices are compared with the helix geometry in fig.(4.18). The effect of velocity field induced by the trailing vortices is obvious. The axial induced velocity prevents the wake from moving as fast as the upstream flow speed, but the circumferential induced velocity makes the wake rotate faster. This means that the velocity field induced by the trailing

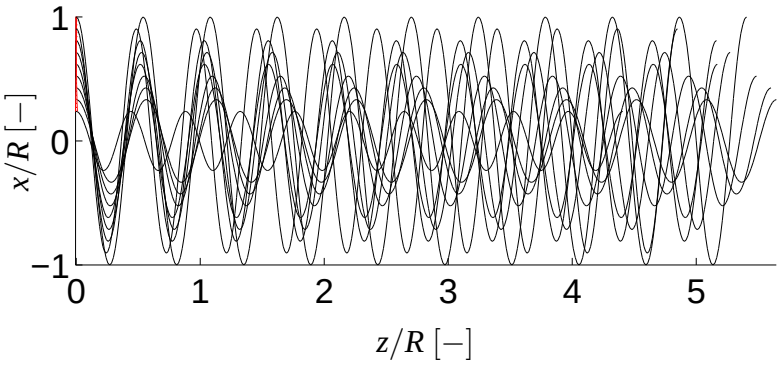

Figure 4.14: Lifting line prescribed wake. Wake geometry for one blade in the $x-z$ plane normalized by the blade radius

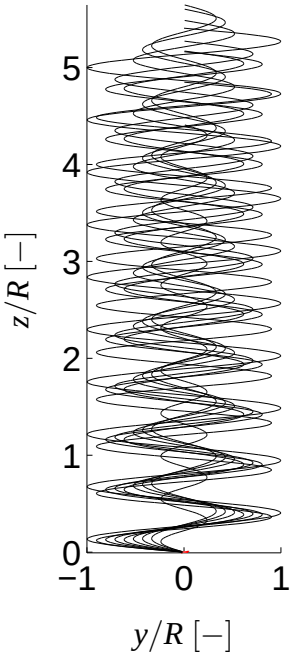

Figure 4.15: Lifting line prescribed wake. Wake geometry for one blade in the $y-z$ plane normalized by the blade radius

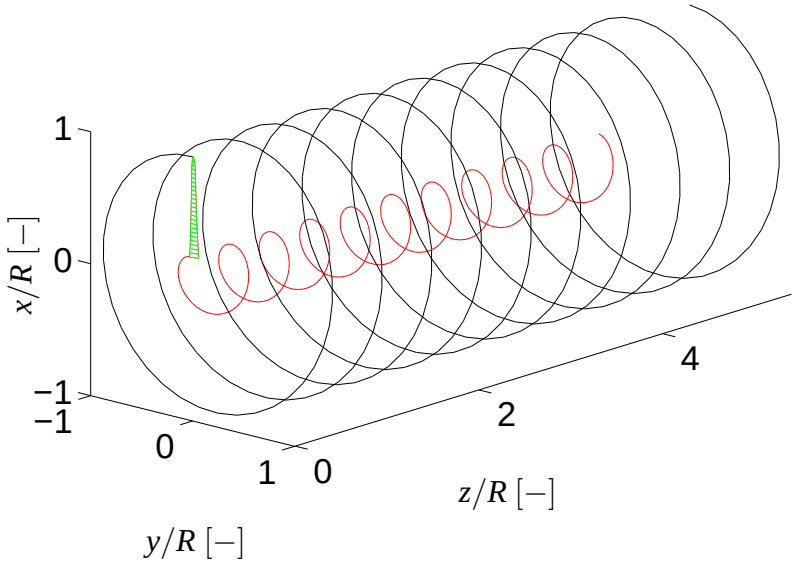

Figure 4.16: Lifting line prescribed wake. Tip and root vortices for one blade normalized by the blade radius, ——: Tip vortex, ——: Root vortex

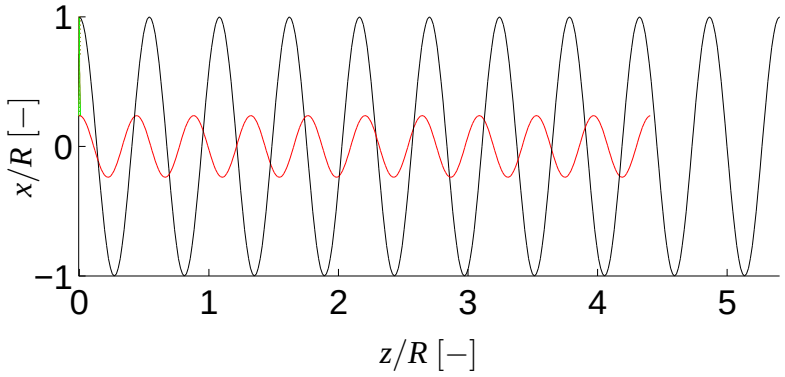

Figure 4.17: Lifting line prescribed wake. Tip and root vortices for one blade normalized by the blade radius, ——: Tip vortex, ——: Root vortex

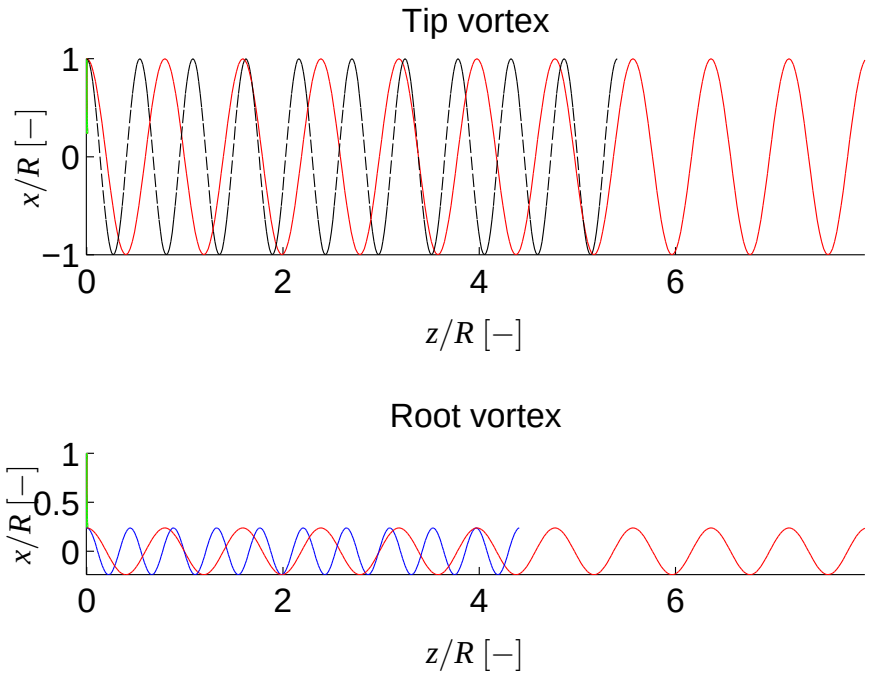

Figure 4.18: Lifting line prescribed wake. Tip and root vortices compared with the helix for one blade in the $x-z$ plane normalized by the blade radius, ------: Tip vortex, ——: Root vortex, ——: Helix

vortices shrinks the wake in the axial direction and amplifies the wake rotational velocity. The reason for this is that the induced tangential velocity is produced in reaction to the torque, which is in the opposite direction of the blade motion.

No. of chordwise section	Power [MW]	error [%]	Thrust [kN]	error [%]
1	1.670	19.731	257.448	30.750
2	1.853	10.947	302.463	18.642
4	1.989	4.400	340.349	8.451
8	2.066	0.716	365.766	1.614
11	2.057	1.131	363.390	2.267
16	2.081	—	371.768	—

Table 4.6: Power and thrust error for the different number of blade chordwise sections

4.2 Vortex Lattice Prescribed Wake

Similar to the previous section, the parameters influencing the accuracy and the time efficiency of the blade and the wake modeling in the vortex lattice prescribed wake are studied. For all cases, the number of blade spanwise sections is assumed to be 25 with fine tip resolution (Cosine method) based on the conclusion drawn from the lifting line prescribed wake model. The calculations for the number of blade chordwise sections are done based on one wake revolution with 10 degrees of segmentation in the azimuthal direction; for the wake discretization effect, they are done for only one wake revolution. Finally, the effect of the wake truncation is studied where the wake is discretized by 10 degrees in the azimuthal direction for different wake lengths.

4.2.1 Blade chordwise section

In the vortex lattice prescribed wake, since the blade is modeled as the lifting surface and the circulation distribution, Γ, over the blade is obtained by satisfying the zero normal flow boundary condition, the resolution of the blade surface discretization in the chordwise direction must be studied.

Table (4.6) shows a comparison of the generated power and the thrust for the different number of equally spaced blade chordwise sections. The maximum calculated error for 8 and more chordwise discretization is about 2%, which means that the surface curvature plays an important role for the blade circulation distribution (see also fig.(4.19)).

Figures (4.20) and (4.21) show that the inadequate resolution of the blade chordwise sections can influence both the tangential and normal forces over the blade. The results are consistent with table (4.6), since the generated power and the thrust are calculated by the tangential and normal forces, respectively.

The effective angle of attack is also affected by the number of blade chordwise sections where, in agreement with the circulation, tangential and normal forces, 8 panels seem to be sufficient to take into account the blade surface curvature.

Table (4.7) shows the NRMSE of the different number of chordwise sections on the circulation, angle of attack and forces, which are in agreement with the related figures.

To sum up, the blade chordwise discretization has a significant effect on the wind turbine performance parameters and is directly connected to the blade circulation distribution. This discretization must be examined, especially for highly cambered airfoils.

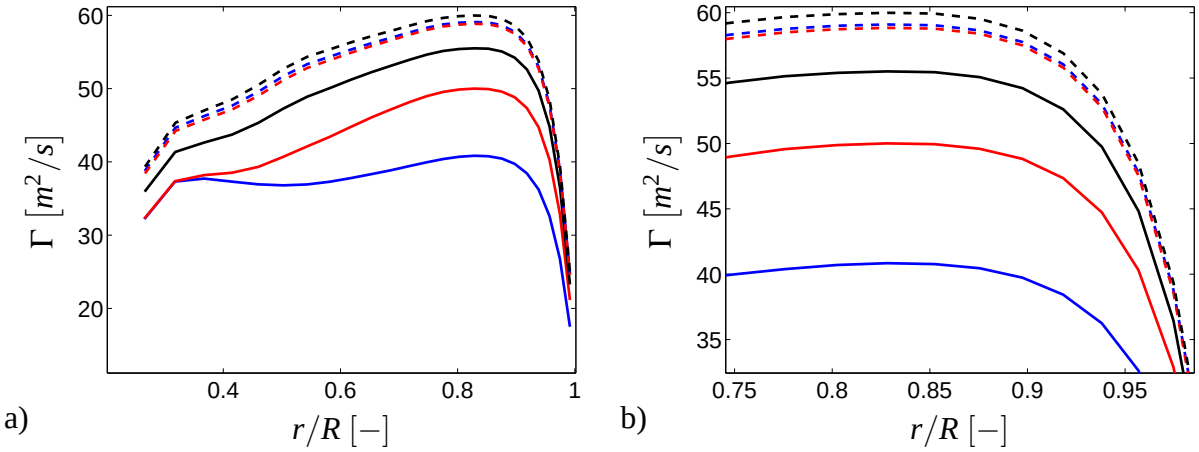

Figure 4.19: Distribution of the circulation along the blade, ——: 1 section, ——: 2 sections, ——: 4 sections, - - - -: 8 sections, - - - -: 11 sections, - - - -: 16 sections

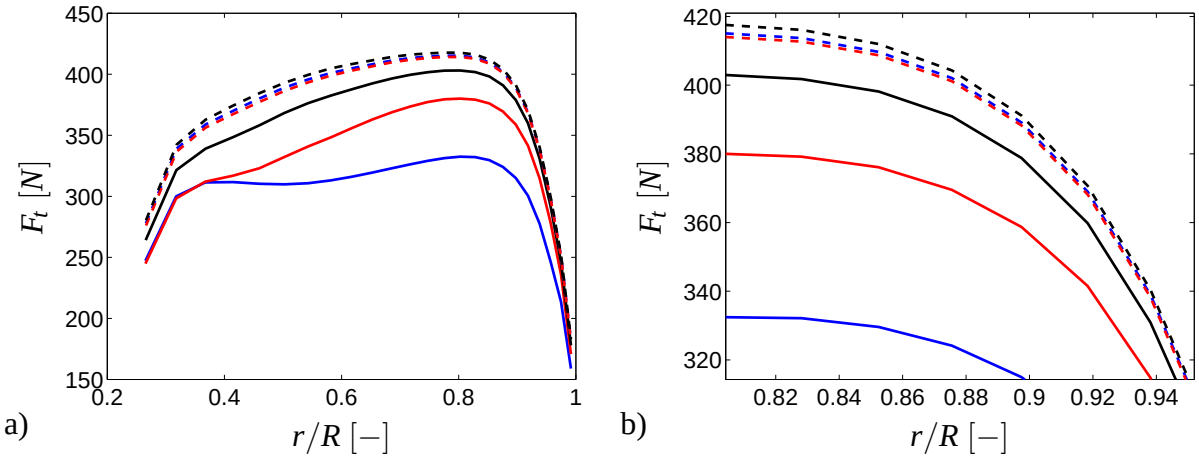

Figure 4.20: Distribution of the tangential force with respect to the rotor plane, ——: 1 section, ——: 2 sections, ——: 4 sections, - - - -: 8 sections, - - - -: 11 sections, - - - -: 16 sections

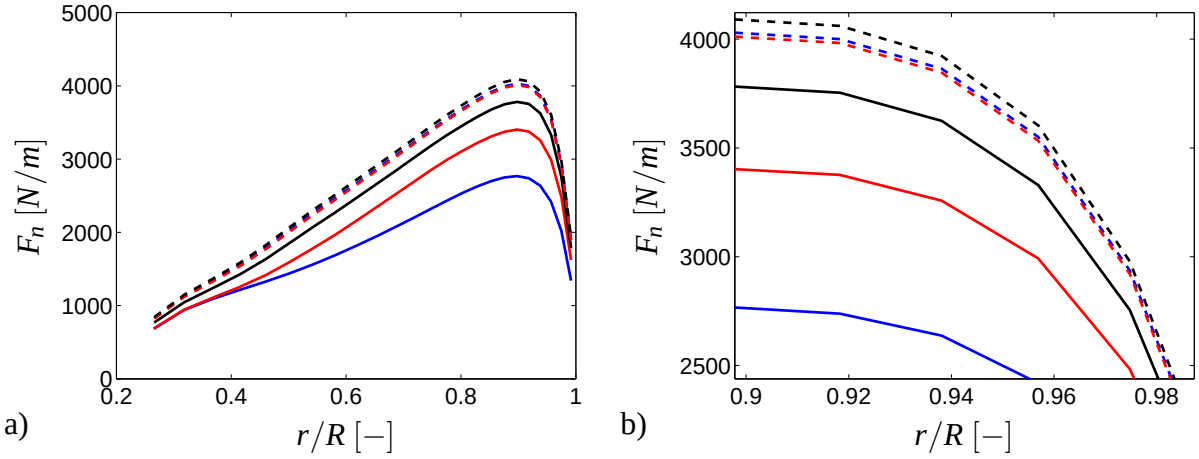

Figure 4.21: Distribution of the normal force with respect to the rotor plane, ——: 1 section, ——: 2 sections, ——: 4 sections, - - - -: 8 sections, - - - -: 11 sections, - - - -: 16 sections

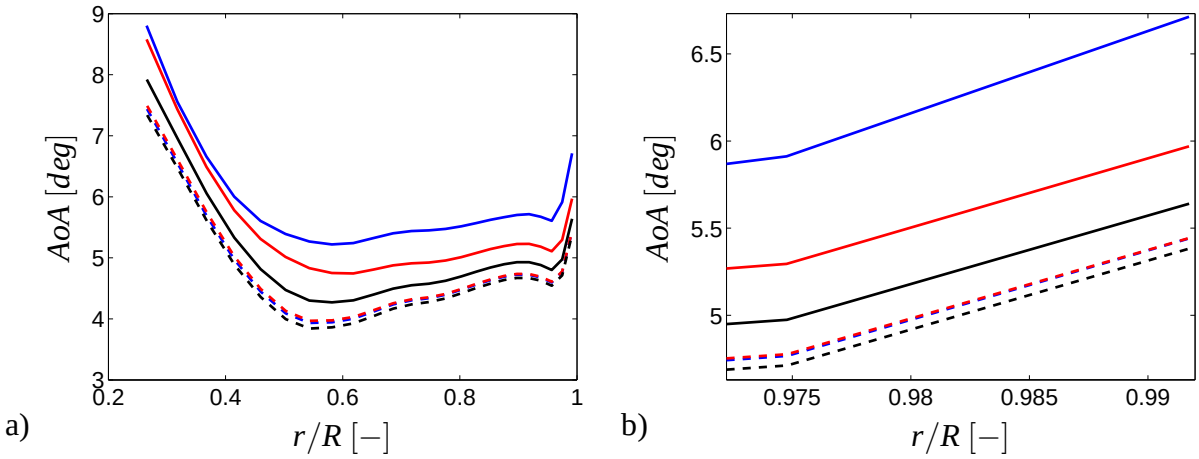

Figure 4.22: Distribution of the angle of attack along the blade, ——: 1 section, ——: 2 sections, ——: 4 sections, - - - -: 8 sections, - - - -: 11 sections, - - - -: 16 sections

No. of chordwise section	NRMSE (Γ)	NRMSE (F_t)	NRMSE (F_n)	NRMSE (AoA)
1	0.705	0.430	0.469	0.333
2	0.342	0.204	0.200	0.199
4	0.139	0.078	0.081	0.099
8	0.025	0.012	0.015	0.020
11	0.035	0.020	0.020	0.028
16	—	—	—	—

Table 4.7: Normalized root-mean squared error for the different number of blade chordwise sections

Wake azimuthal angle [deg]	Power [MW]	error [%]	Thrust [kN]	error [%]
2	2.081	—	367.288	—
5	2.076	0.238	366.790	0.136
10	2.066	0.734	365.770	0.415
15	2.055	1.259	364.670	0.712
20	2.044	1.801	363.530	1.024
30	2.020	2.957	361.030	1.703

Table 4.8: Power and thrust error for the different wake azimuthal angles

4.2.2 Wake azimuthal angle

The velocity field induced by trailing wake vortices may have a large contribution to the performance of a wind turbine inflow condition. As we know, the emanating helical trailing vortices are modeled by straight vortex filaments where, in order to increase the accuracy of the induced velocity field over the blade, they are divided into a number of small segments. In this part, the effect of the different wake segmentations is studied. Based on the conclusion drawn in the previous section, the calculations are done for the blade consisting of the 8 panels in the chordwise direction and 25 sections in the spanwise direction.

Table (4.8) shows how the power and the thrust of the wind turbine are changed due to the wake discretization.

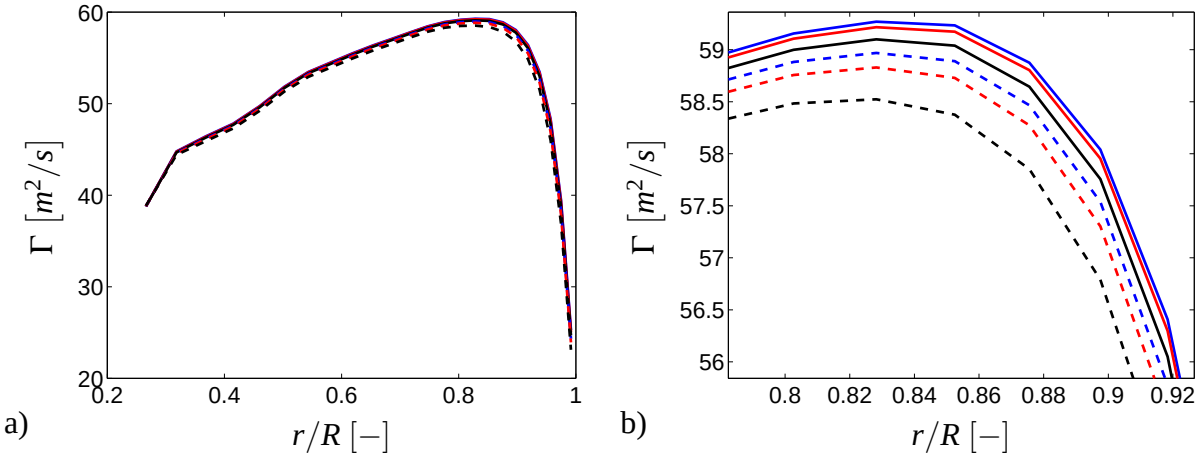

Figure 4.23: Distribution of the circulation along the blade, ——: 2 deg, ——: 5 deg, ——: 10 deg, - - - -: 15 deg, - - - -: 20 deg, - - - -: 30 deg

According to fig.(4.23), the circulation values along the blade are converged by refining the wake segmentation in terms of the azimuthal angle. In addition, table (4.8) shows that 10 degrees of azimuthal segmentation may be referred to be enough for the wake discretization.

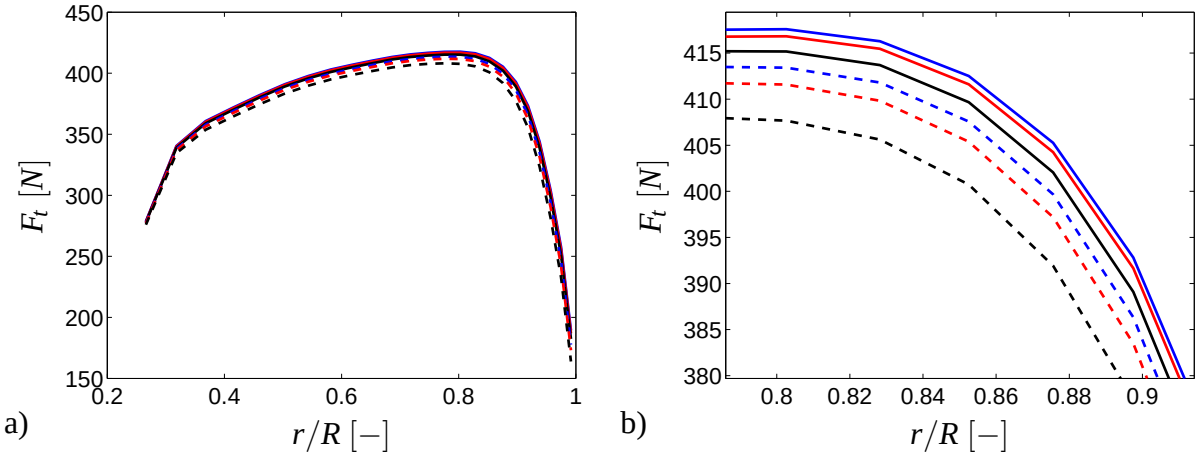

Figure 4.24: Distribution of the tangential force with respect to the rotor plane, ——: 2 deg, ——: 5 deg, ——: 10 deg, - - - -: 15 deg, - - - -: 20 deg, - - - -: 30 deg

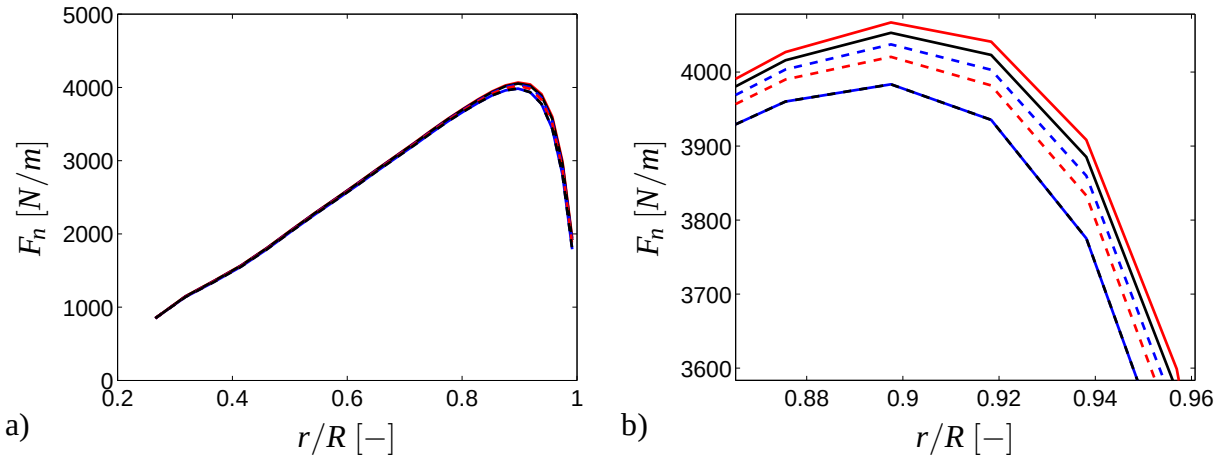

Figure 4.25: Distribution of the normal force with respect to the rotor plane, ——: 2 deg, ——: 5 deg, ——: 10 deg, - - - -: 15 deg, - - - -: 20 deg, - - - -: 30 deg

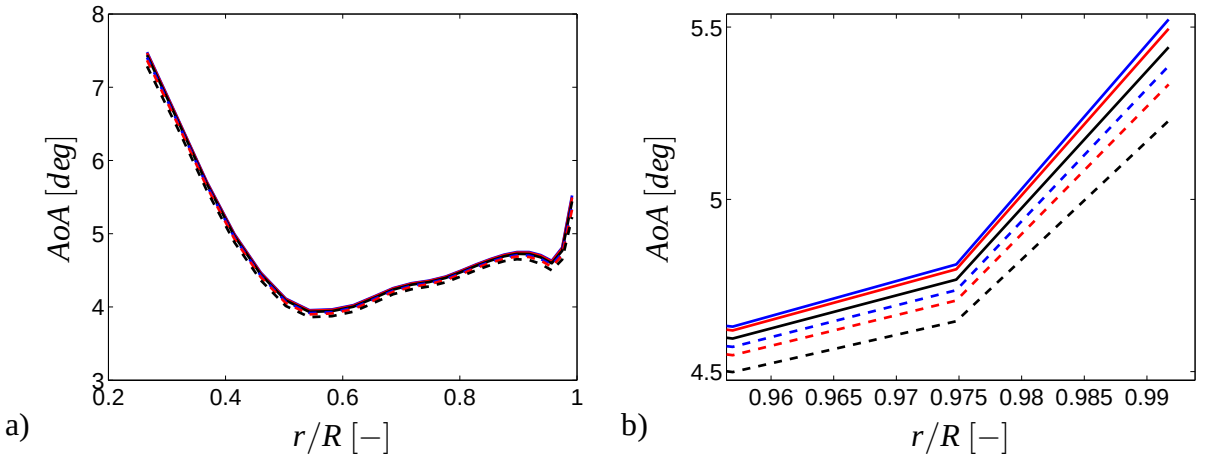

Figure 4.26: Distribution of the angle of attack along the blade, ——: 2 deg, ——: 5 deg, ——: 10 deg, - - - -: 15 deg, - - - -: 20 deg, - - - -: 30 deg

Wake azimuthal angle [deg]	NRMSE (Γ)	NRMSE (F_t)	NRMSE (F_n)	NRMSE (AoA)
2	—	—	—	—
5	0.003	0.005	0.002	0.003
10	0.008	0.014	0.006	0.009
15	0.014	0.024	0.011	0.015
20	0.020	0.034	0.016	0.022
30	0.032	0.054	0.026	0.036

Table 4.9: Normalized root-mean squared error for the different wake azimuthal angles

Wake length [m]	Power [MW]	error [%]	Thrust [kN]	error [%]
1D	2.195	10.273	376.941	5.051
2D	2.058	3.392	364.867	1.686
3D	2.018	1.371	361.268	0.683
4D	2.002	0.545	359.793	0.272
5D	1.993	0.135	359.061	0.068
6D	1.991	—	358.817	—

Table 4.10: Power and thrust error for the different wake lengths

It is also obvious from figs.(4.24), (4.25), (4.26) and table (4.9) that very fine wake discretization only increases the computational time and the NRMSE dose not change a great deal.

Similar to the lifting line prescribed wake, the error of the generated power and the thrust along with the NRMSE of the different factors imply that the 10 degrees of azimuth is well suited for the trailing wake vortices" segmentation.

4.2.3 Wake length

In the vortex theory, which is based on the potential flow, it is supposed that the trailing wake extends to infinity. For computational reasons, the flow field is calculated only for a limited wake length. To study the effect of the wake length, it is assumed that the blade surface in the chordwise section is divided into 8 equally spaced panels. 10 degrees of azimuthal discretization is also used for the vortex wake elements.

Table (4.11) shows how the power and the thrust of the wind turbine are affected by the wake length. It can be seen that the power and the thrust errors for the $4D$ wake length are less than 1%, which is similar to the lifting line prescribed wake method.

The circulation of the blade is shown in fig.(4.27) where a good convergency can be observed for $4D$ wake length and more.

Increasing the length of the wake more than four blade diameters does not change the forces and the effective angle of attack, as can be seen in figs.(4.28), (4.29) and (4.30). In addition, table (4.11) is in agreement with the corresponding figures.

It is clear that the effect of wake truncation after $4D$ wake length on the blade is fairly small. This fact supports the conclusion drawn in the lifting line prescribed wake approach.

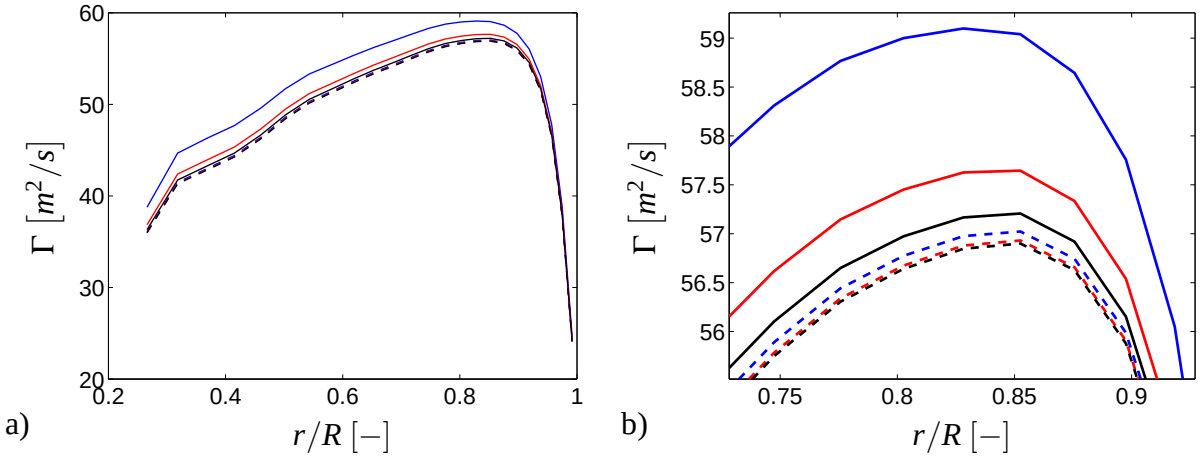

Figure 4.27: Distribution of the circulation along the blade, ——: $1D$, ——: $2D$, ——: $3D$, : $4D$, ------: $5D$, ------: $6D$

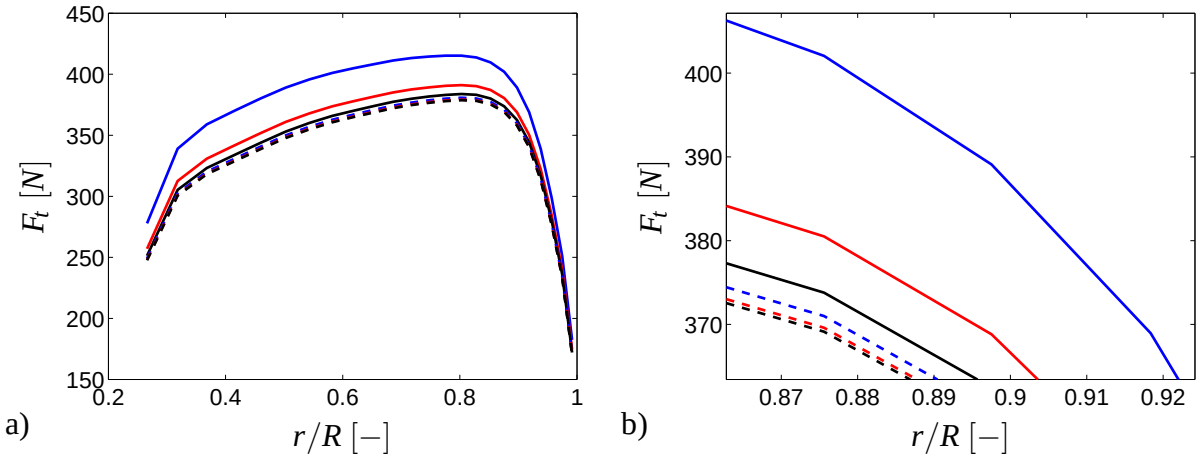

Figure 4.28: Distribution of the tangential force with respect to the rotor plane, ——: $1D$, ——: $2D$, ——: $3D$, ------: $4D$, ------: $5D$, ------: $6D$

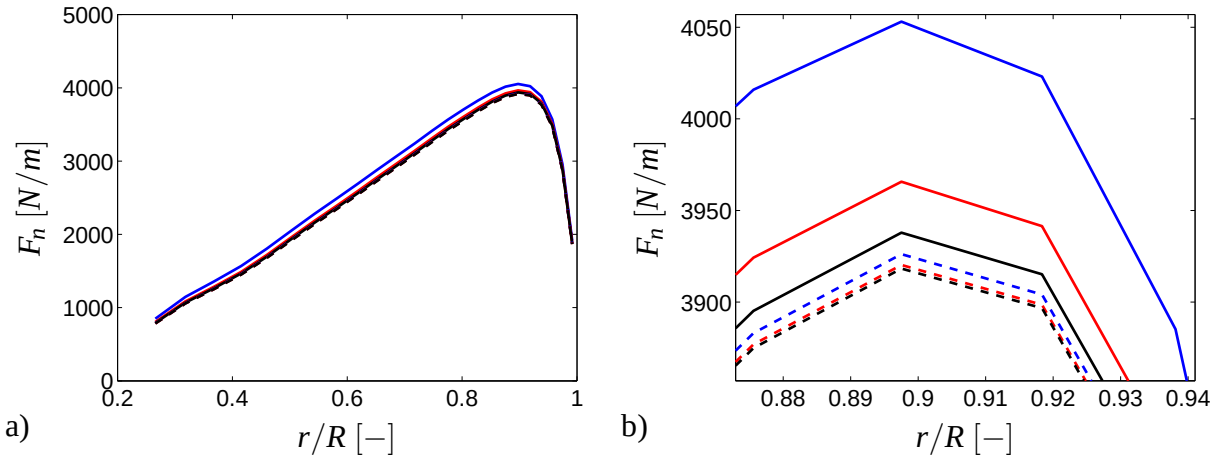

Figure 4.29: Distribution of the normal force with respect to the rotor plane, ——: $1D$, ——: $2D$, ——: $3D$, ------: $4D$, ------: $5D$, ------: $6D$

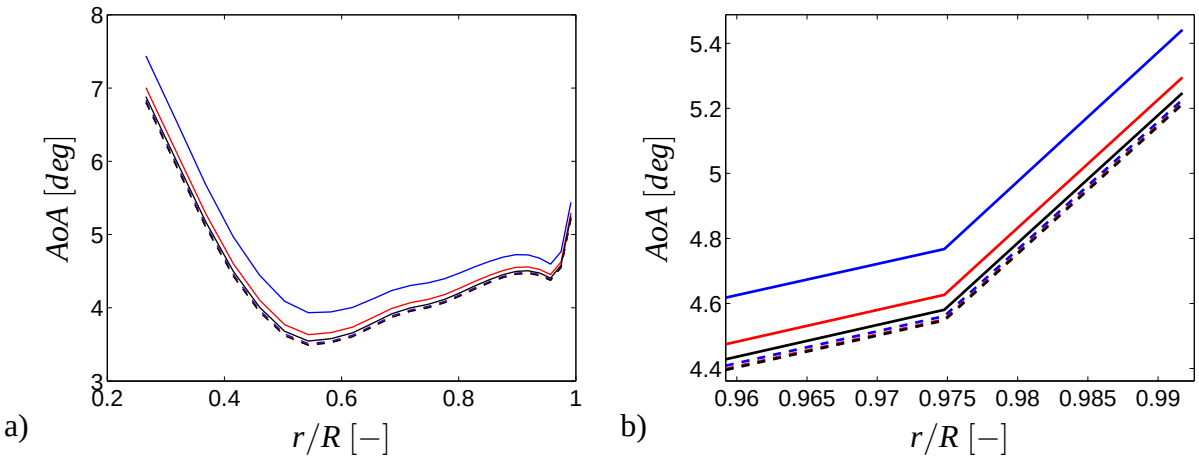

Figure 4.30: Distribution of the angle of attack along the blade, ——: 1D, ——: 2D, ——: 3D, - - - -: 4D, - - - -: 5D, - - - -: 6D

Wake length [m]	NRMSE (Γ)	NRMSE (F_t)	NRMSE (F_n)	NRMSE (AoA)
1D	0.075	0.151	0.040	0.113
2D	0.026	0.053	0.014	0.039
3D	0.010	0.022	0.006	0.016
4D	0.004	0.009	0.002	0.006
5D	0.001	0.002	0.001	0.002
6D	—	—	—	—

Table 4.11: Normalized root-mean squared error for the different wake lengths

4.2.4 Modeling features

Different parameters, such as number of blade spanwise sections, wake element discretization and wake length, were studied for the vortex lattice prescribed wake where 25 blade spanwise sections with the fine resolution near the tip, 8 equally spaced blade discretization in the chordwise direction, 10 degrees of azimuth for the wake element segmentation and 4D wake length fulfill the accuracy and the computational time efficiency. The outcomes of this model can be discussed as the following.

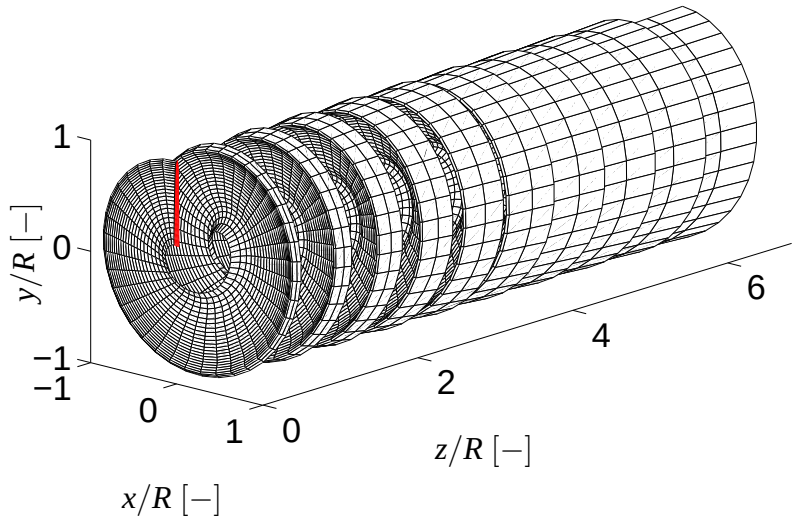

Figure 4.31: Vortex lattice prescribed wake. Wake geometry for one blade normalized by the blade radius

The trailing vortices constructed by the vortex ring elements for one blade are shown in figs.(4.31), (4.32) and (4.33). Similar behavior shown for the lifting line prescribed wake is repeated here where the vortex wake elements are not permitted to travel downstream with the same velocity of the upstream flow because of the induced velocity field. In addition, figs.(4.34) and (4.35) show that the induced velocity varies along the blade since all the trailing vortices do not travel with the same axial velocity. The root vortices move more slowly than the tip vortices, which means that there is a larger induced velocity field over the blade root section than the tip region.

Comparison of the tip and root vortices with the helix seen in fig.(4.36) reflects the effect of the induced velocity field, which shows that the wake is squeezed in the z direction but that it rotates faster in reaction to the blade torque. This means that the axial induced velocity is against the wind flow, but its circumferential component enhances the wake rotational velocity. Finally, no wake expansion is realized as a result of the prescribed wake.

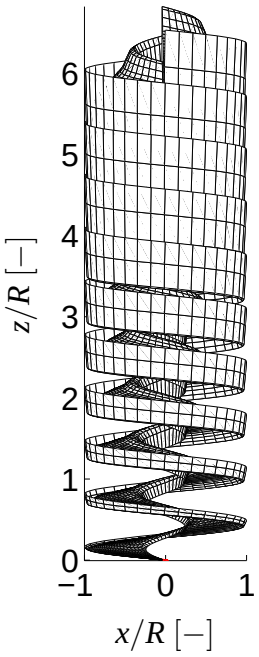

Figure 4.32: Vortex lattice prescribed wake. Wake geometry for one blade in the $x-z$ plane normalized by the blade radius

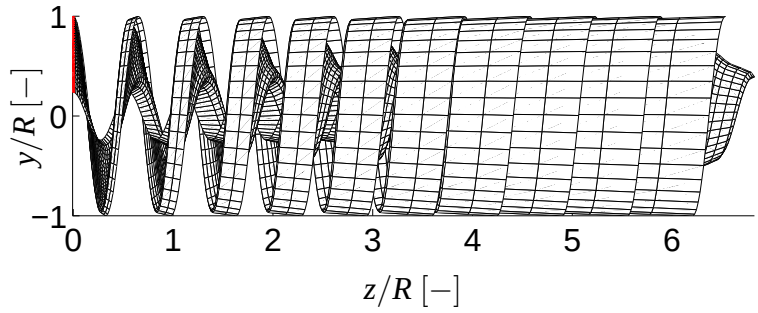

Figure 4.33: Vortex lattice prescribed wake. Wake geometry for one blade in the $y-z$ plane normalized by the blade radius

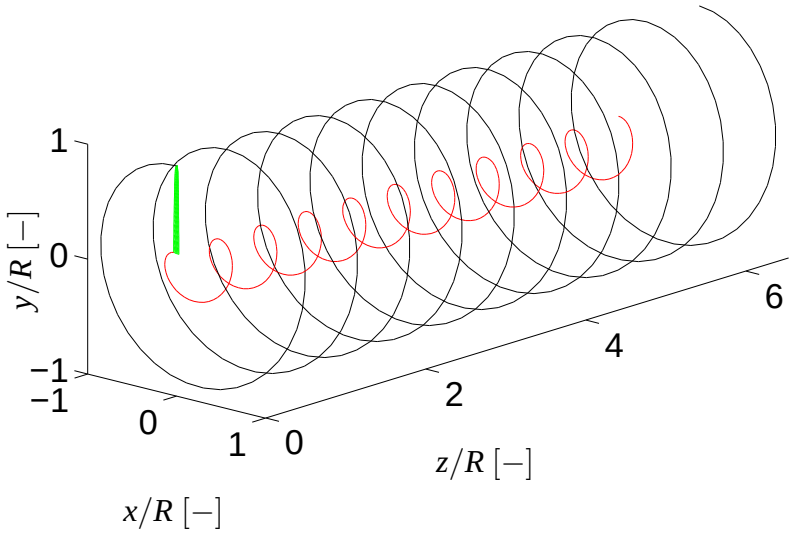

Figure 4.34: Vortex lattice prescribed wake. Tip and root vortices for one blade normalized by the blade radius, ——: Tip vortex, ——: Root vortex

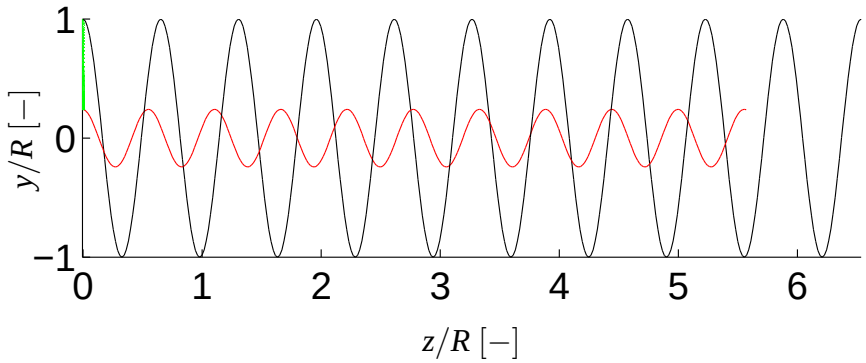

Figure 4.35: Vortex lattice prescribed wake. Tip and root vortices for one blade in the $y-z$ plane normalized by the blade radius, ——: Tip vortex, ——: Root vortex

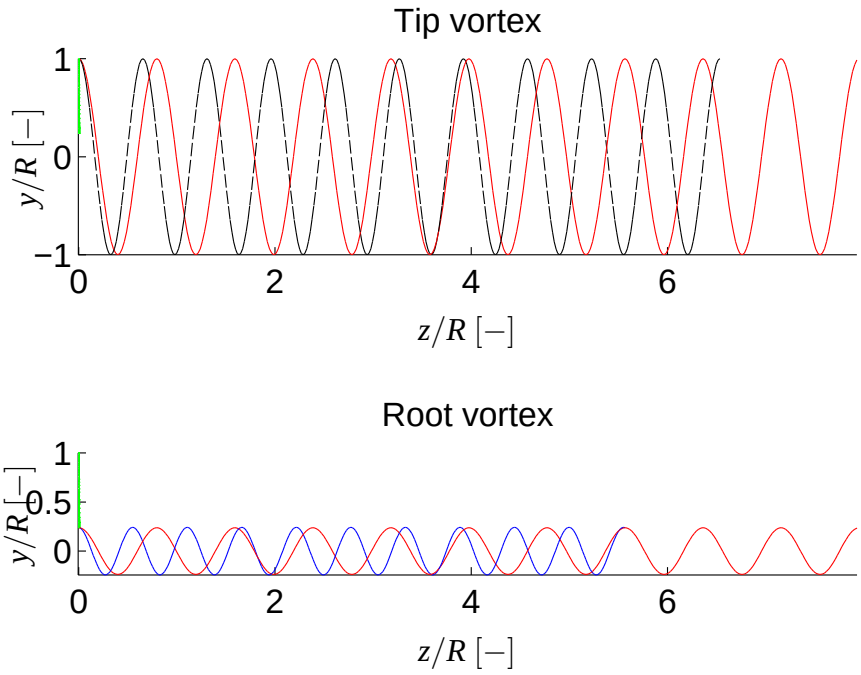

Figure 4.36: Vortex lattice prescribed wake. Tip and root vortices compared with the helix for one blade in the $y-z$ plane normalized by the blade radius, ------: Tip vortex, ——: Root vortex, ——: Helix

4.3 Vortex Lattice Free Wake

As for the other approaches studied before, different blade and wake modeling parameters are examined in this section. For all cases, the blade is divided into 25 spanwise sections with a fine tip region because of the large circulation gradient. The resolution of the blade chordwise discretization, the wake segmentation and the wake truncation length are studied. The explicit method is used as the numerical integration scheme for all the cases. It is also assumed that the core radius of the vortex filaments remains constant.

4.3.1 Blade chordwise section

Table (4.12) proves that the 8 equally spaced sections in the chordwise direction is the minimum blade discretization. Compared with the very fine resolution, 16 chordwise sections, it can be seen that the error of the power and thrust is below 2% for 8 sections suitable for the modeling purpose. Also, fig.(4.37) shows how the coarse chordwise discretization leads to an inaccurate circulation distribution because the blade surface curvature cannot be accurately accounted for when applying the zero normal boundary condition to calculate the circulation over the blade.

Recalling the contribution of the circulation on the wind turbine inflow condition, figs.(4.38), (4.39) and (4.40) are in accordance with the results obtained with the vortex lattice prescribed wake. It can also be seen in table (4.13) that the NRMSE of the coarse chordwise resolution is large for different load parameters.

As discussed above, the blade resolution in the chordwise direction plays an important role

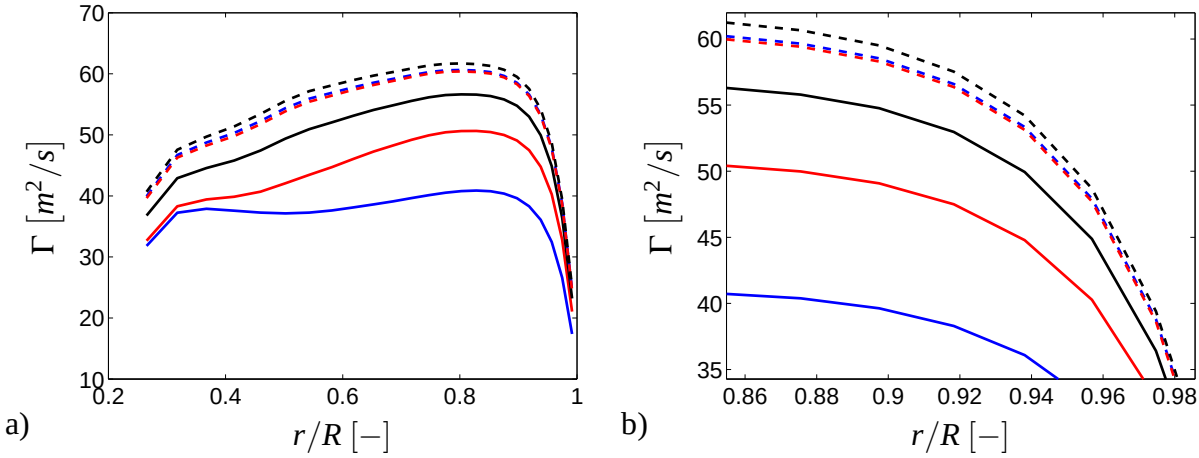

Figure 4.37: Distribution of the circulation along the blade, ——: 1 section, ——: 2 sections, ——: 4 sections, - - - -: 8 sections, - - - -: 11 sections, - - - -: 16 sections

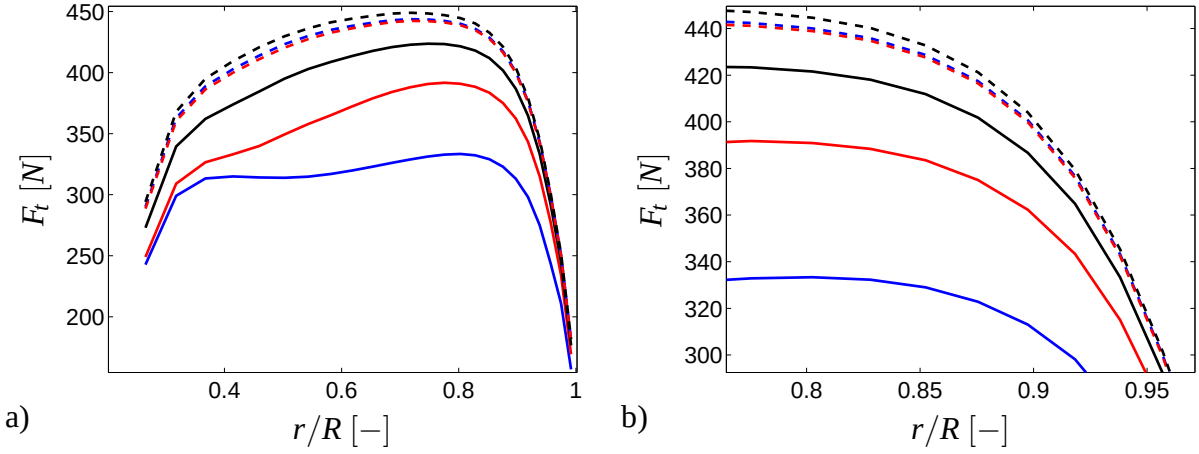

Figure 4.38: Distribution of the tangential force with respect to the rotor plane, ——: 1 section, ——: 2 sections, ——: 4 sections, - - - -: 8 sections, - - - -: 11 sections, - - - -: 16 sections

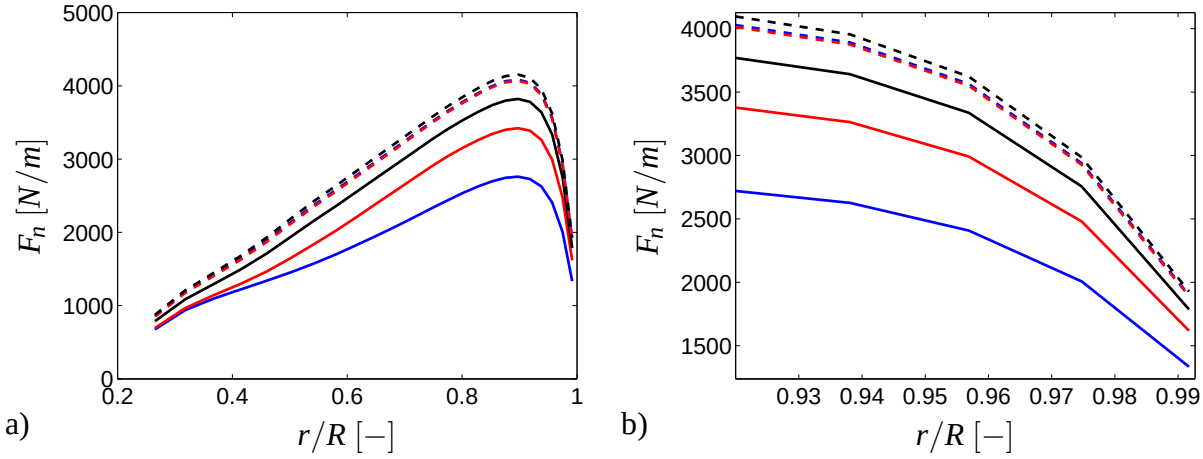

Figure 4.39: Distribution of the normal force with respect to the rotor plane, ——: 1 section, ——: 2 sections, ——: 4 sections, - - - -: 8 sections, - - - -: 11 sections, - - - -: 16 sections

No. of chordwise section	Power [MW]	error [%]	Thrust [kN]	error [%]
1	1.676	24.450	258.098	32.927
2	1.911	13.863	308.086	19.936
4	2.086	5.994	349.450	9.187
8	2.193	1.143	377.670	1.853
11	2.184	1.550	375.368	2.451
16	2.219	—	384.800	—

Table 4.12: Power and thrust error for the different number of blade chordwise sections

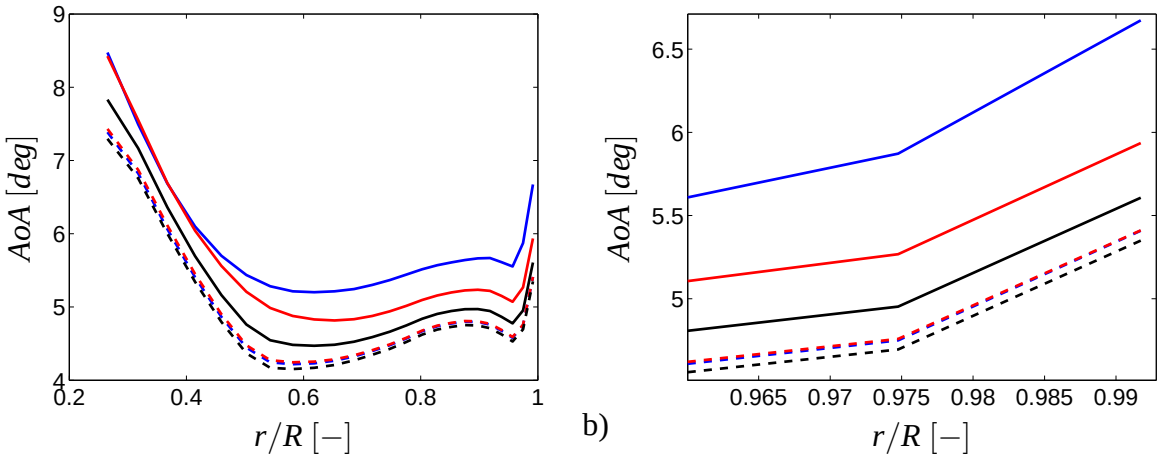

Figure 4.40: Distribution of the angle of attack along the blade, ——: 1 section, ——: 2 sections, ——: 4 sections, - - - -: 8 sections, - - - -: 11 sections, - - - -: 16 sections

No. of chordwise section	NRMSE (Γ)	NRMSE (F_t)	NRMSE (F_n)	NRMSE (AoA)
1	0.772	0.561	0.507	0.300
2	0.369	0.260	0.218	0.178
4	0.151	0.102	0.089	0.090
8	0.028	0.018	0.017	0.019
11	0.038	0.025	0.022	0.026
16	—	—	—	—

Table 4.13: Normalized root-mean squared error for the different number of blade chordwise sections

Wake azimuthal angle [deg]	Power [MW]	error [%]	Thrust [kN]	error [%]
2	2.194	—	377.496	—
5	2.195	0.036	377.632	0.036
10	2.193	0.015	377.670	0.046
15	2.191	0.133	377.580	0.022
20	2.187	0.313	377.402	1.025
30	2.177	0.778	376.891	0.160

Table 4.14: Power and thrust error for the different wake azimuthal angles

since it represents the blade surface configuration that is used to compute the circulation distribution over the blade and is directly connected to the strength of the trailing and shed vortices. This is the main reason for the relatively large errors that are shown in table (4.13). Regarding the results of this section, it is considered for the next sections that the blade consists of 8 equally spaced sections.

4.3.2 Wake azimuthal angle

Since the wake geometry is represented by the vortex ring elements, including the trailing and the shed vortices in the vortex lattice method, the discretization of the wake can have a considerable effect on the accuracy of the induced velocity field.

Here, six different wake segmentations in terms of the azimuthal angle are studied. A Comparison of table (4.14) and fig.(4.41) shows that the generated power error of the wake discretization is sufficiently low for 10 degrees of azimuthal discretization.

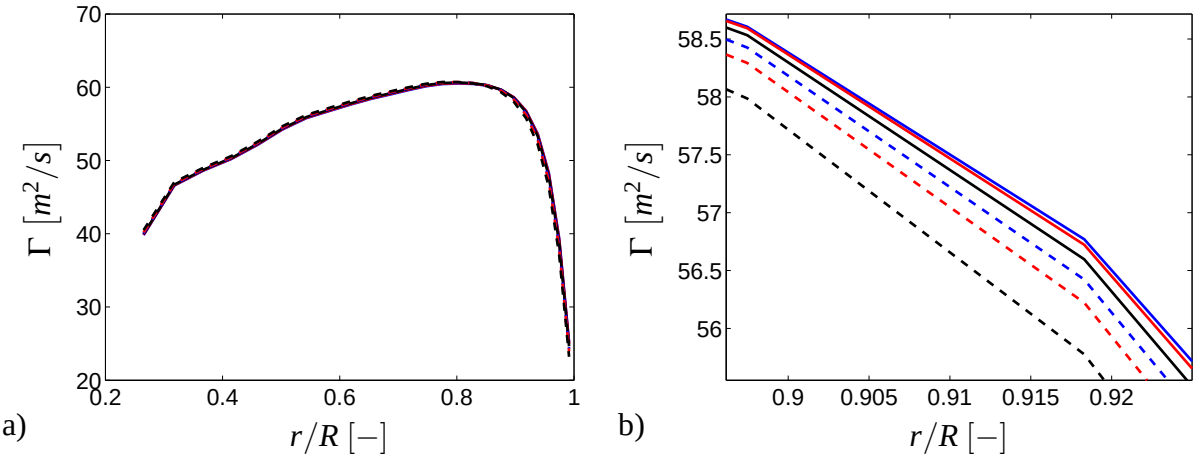

Figure 4.41: Distribution of the circulation along the blade, ——: 2 deg, ——: 5 deg, ——: 10 deg, - - - - - -: 15 deg, - - - - - -: 20 deg, - - - - - -: 30 deg

It can be seen from figs.(4.42) and (4.43) that the large segmentation of the trailing wake also does not predict the different forces along the blade well. A similar pattern is repeated for the effective angle of attack, as it can be seen in fig.(4.44). The tangential and normal forces are converged to the specific values by increasing the number of segmentations per wake revolution.

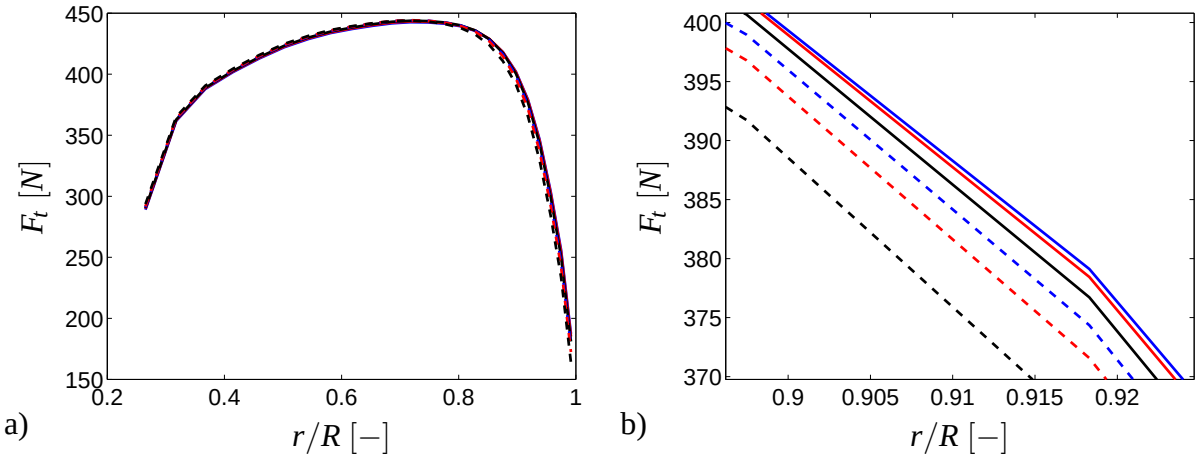

Figure 4.42: Distribution of the tangential force with respect to the rotor plane, ——: 2 deg, ——: 5 deg, ——: 10 deg, - - - -: 15 deg, - - - -: 20 deg, - - - -: 30 deg

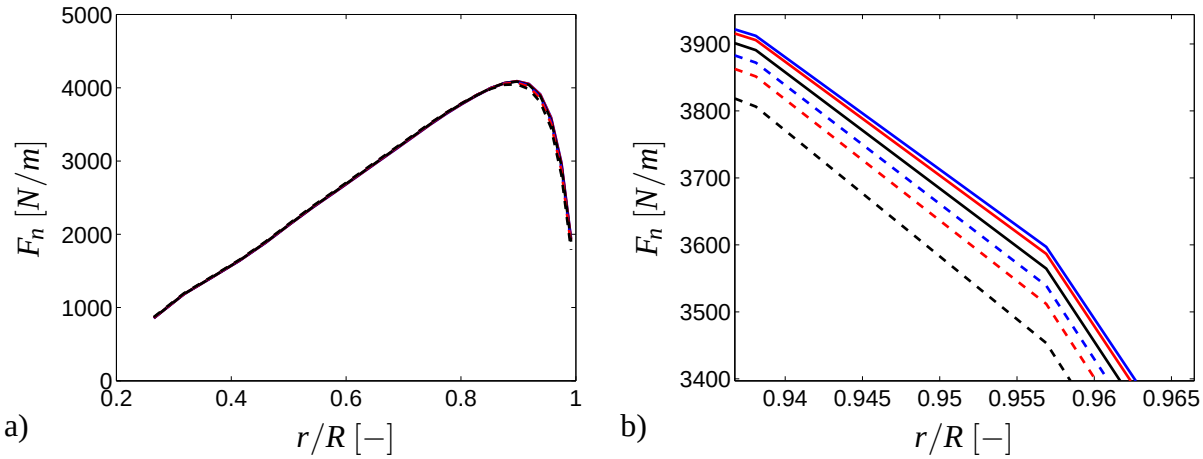

Figure 4.43: Distribution of the normal force with respect to the rotor plane, ——: 2 deg, ——: 5 deg, ——: 10 deg, - - - -: 15 deg, - - - -: 20 deg, - - - -: 30 deg

Wake azimuthal angle [deg]	NRMSE (Γ)	NRMSE (F_t)	NRMSE (F_n)	NRMSE (AoA)
2	——	——	——	——
5	0.002	0.003	0.002	0.002
10	0.006	0.009	0.005	0.006
15	0.010	0.015	0.008	0.011
20	0.015	0.021	0.012	0.016
30	0.024	0.034	0.020	0.027

Table 4.15: Normalized root-mean squared error for the different wake azimuthal angles

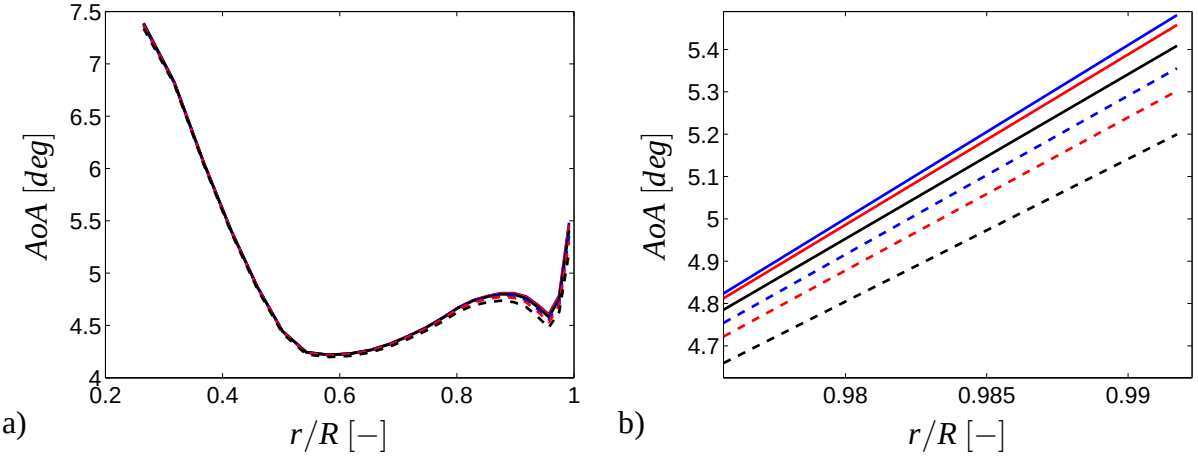

Figure 4.44: Distribution of the angle of attack along the blade, ——: 2 deg, ——: 5 deg, ——: 10 deg, - - - -: 15 deg, - - - -: 20 deg, - - - -: 30 deg

Wake length [m]	Power [MW]	error [%]	Thrust [kN]	error [%]
1D	2.193	10.740	377.669	5.238
2D	2.074	4.707	367.177	2.314
3D	2.027	2.344	363.021	1.156
4D	2.003	1.146	360.907	0.567
5D	1.989	0.435	359.644	0.215
6D	1.981	——	358.873	——

Table 4.16: Power and thrust error for the different wake lengths

By refining the wake discretization, the computational time increases spectacularly, which shows that the number of vortex filaments for each wake revolution must be chosen carefully. Table (4.15) shows the NRMSE variation of the different parameters related to the wake discretization. As mentioned in the above paragraph, the 10 degrees of azimuth wake discretization may be interpreted to fit both the accuracy and computational time efficiency.

4.3.3 Wake length

In the vortex lattice free wake, the wake elements move freely based on the local velocity field where the velocity field induced by the trailing and the shed vortices is evaluated by the Biot-Savart equation at each time step. Therefore, the more the number of wake elements, the more computational time and memory are required. In order to overcome this problem, it is assumed that the wake is truncated as in the previous sections. Here, 10 degrees of azimuth is applied for the wake discretization.

According to table (4.16), the truncation error of the generated power and the thrust for $4D$ wake length is about 1%. Also, fig.(4.45) proves that there is no significant change for the blade circulation distribution when the wake length is increased from $4D$ to $6D$.

The converged solution for $4D$ wake length means that the effect of the very far wake on the blade load is negligible, as can be seen in figs.(4.46) and (4.47).

In agreement with the results for the forces, the effective angle of attack shows similar behav-

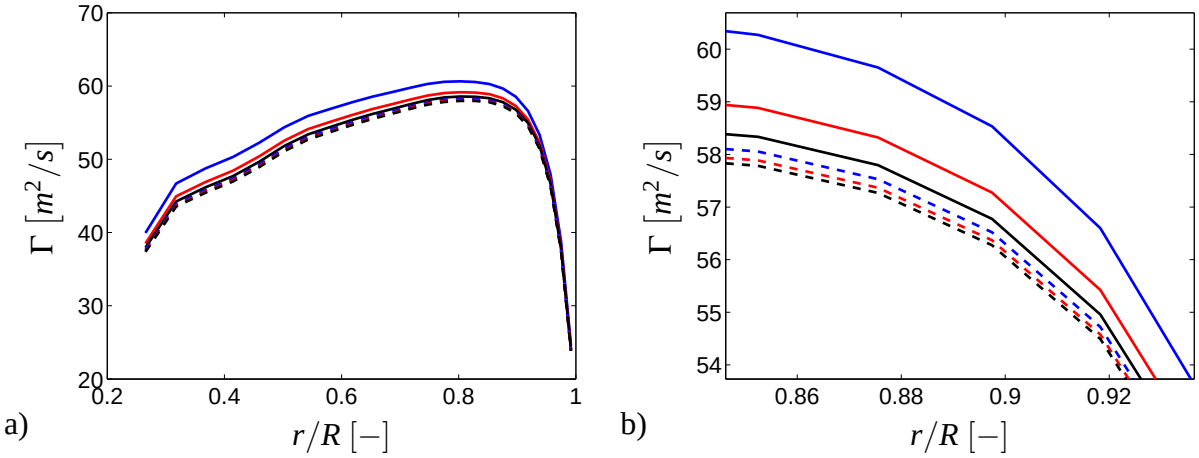

Figure 4.45: Distribution of the circulation along the blade, ——: 1D, ——: 2D, ——: 3D, : 4D, - - - - - -: 5D, - - - - - -: 6D

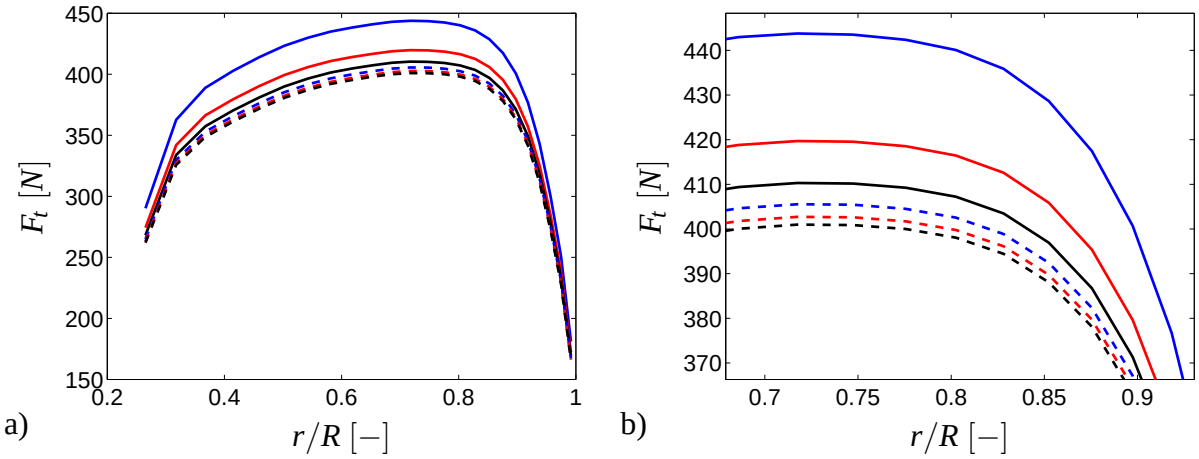

Figure 4.46: Distribution of the tangential force with respect to the rotor plane, ——: 1D, ——: 2D, ——: 3D, - - - - - -: 4D, - - - - - -: 5D, - - - - - -: 6D

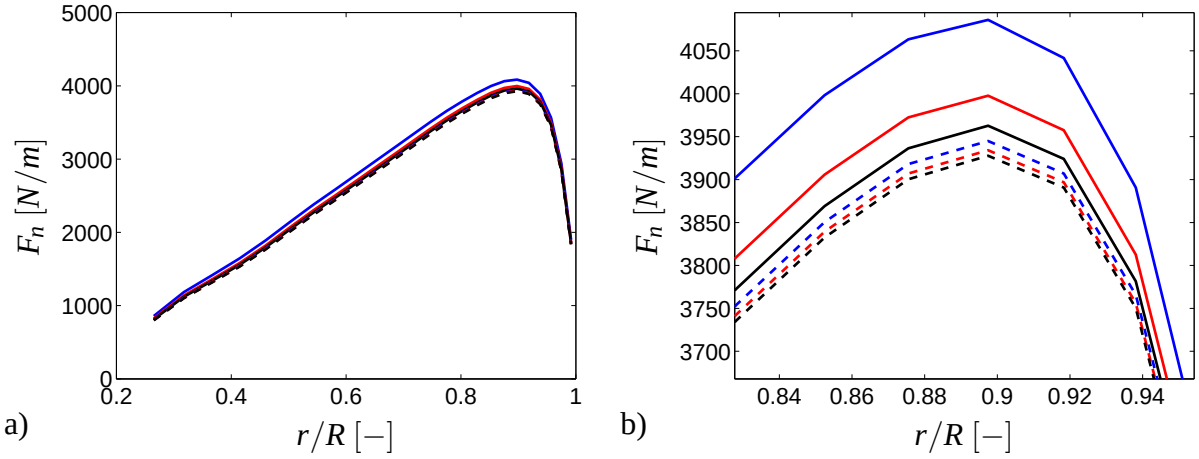

Figure 4.47: Distribution of the normal force with respect to the rotor plane, ——: 1D, ——: 2D, ——: 3D, - - - - - -: 4D, - - - - - -: 5D, - - - - - -: 6D

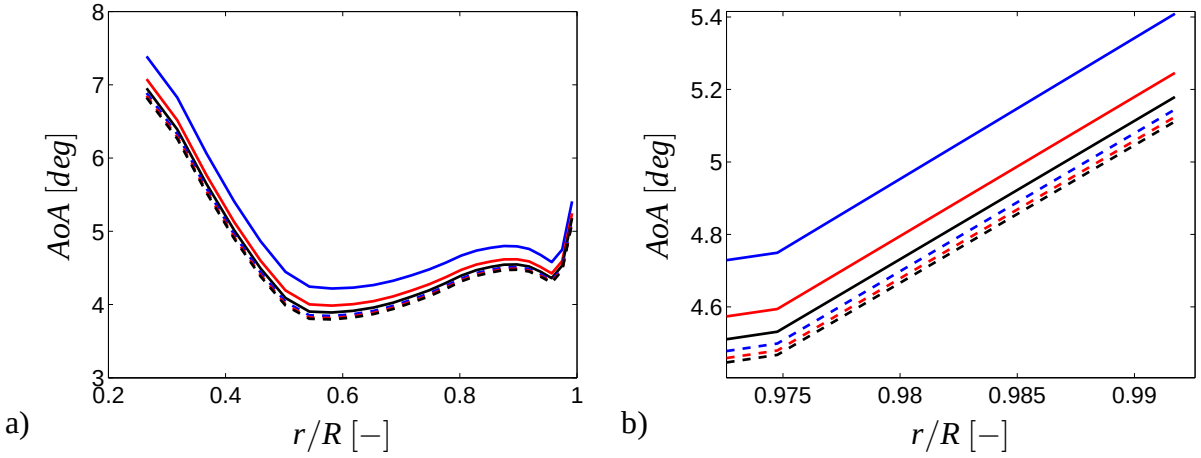

Figure 4.48: Distribution of the angle of attack along the blade, ——: $1D$, ——: $2D$, ——: $3D$, - - - - - -: $4D$, - - - - - -: $5D$, - - - - - -: $6D$

Wake length [m]	NRMSE (Γ)	NRMSE (F_t)	NRMSE (F_n)	NRMSE (AoA)
1D	0.075	0.147	0.043	0.127
2D	0.034	0.068	0.019	0.058
3D	0.017	0.035	0.010	0.030
4D	0.009	0.017	0.005	0.015
5D	0.003	0.006	0.002	0.006
6D	——	——	——	——

Table 4.17: Normalized root-mean squared error for the different wake lengths

ior. This can be seen in fig.(4.48).

By investigating the wake truncation length effect on the blade circulation, the angle of attack and the forces, which is shown in table (4.17), it can be concluded that $4D$ wake length may be considered a suitable wake length in the vortex lattice free wake.

4.3.4 Modeling features

Studying the different features of the vortex lattice free wake leads us to do a simulation based on 25 blade spanwise sections with fine resolution near the tip, 8 equally spaced blade discretization in the chordwise direction, 10 degrees of azimuth for the wake element segmentation and $4D$ wake length. It is assumed that, at t equal to zero, the blade is at rest and, in the next time step ($t = 1$), the blade rotational velocity takes its final value.

The wake geometry of the vortex lattice free wake is represented in figs.(4.49), (4.50) and (4.51). The free moving of the Lagrangian markers is the reason for the non-structured configuration of the vortex wake panels, especially far downstream. However, the longer wake length makes the wake geometry stabler, as can be seen in figs.(4.56) and (4.57). Fig.(4.56) shows that the tip vortex remains stable around $2.5D$ wake length for 40 wake revolutions whereas it remains stable around $1.5D$ wake length for 10 wake revolutions (see fig.(4.54)). There is similar behavior for the root vortex. Nevertheless, comparison of tip and root vortices in figs.(4.54) and (4.57) shows that the root vortex moves downstream faster than the tip vortex which means that the axial

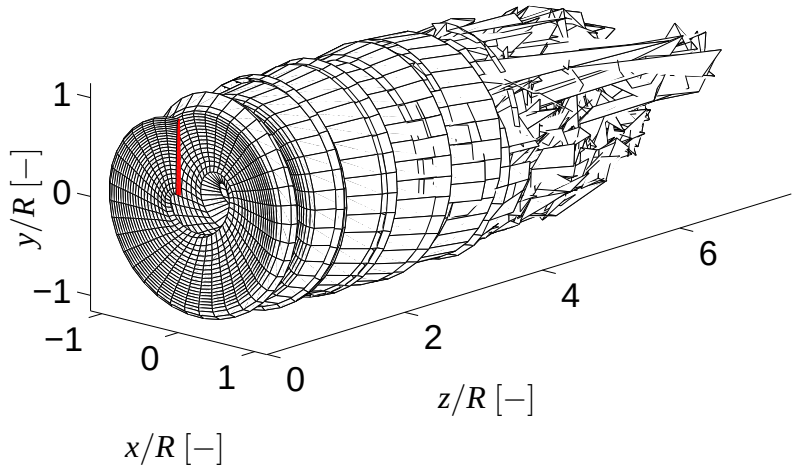

Figure 4.49: Vortex lattice free wake. Wake geometry for one blade normalized by the blade radius

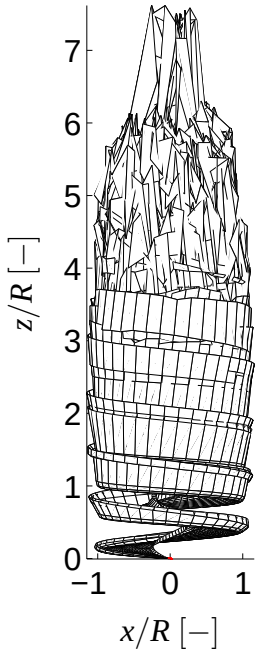

Figure 4.50: Vortex lattice free wake. Wake geometry for one blade in the $x-z$ plane normalized by the blade radius

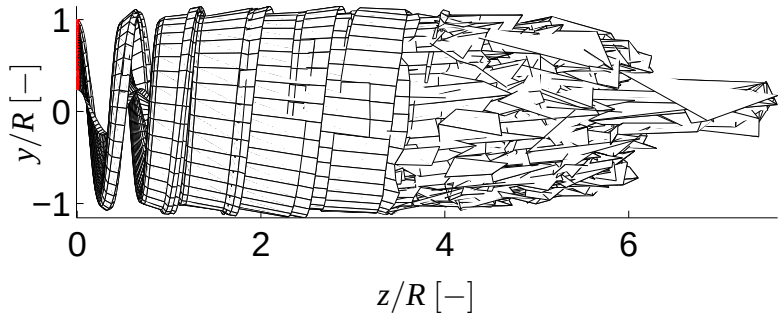

Figure 4.51: Vortex lattice free wake. Wake geometry for one blade in the $y-z$ plane normalized by the blade radius

induced velocity near the root is larger than near the tip.

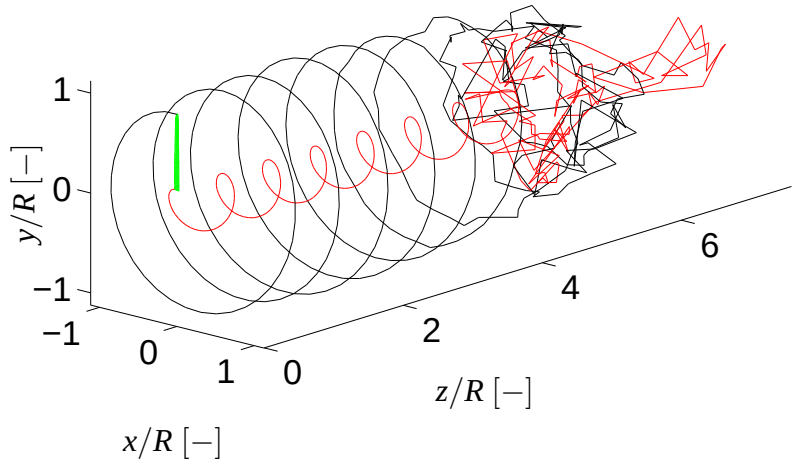

Figure 4.52: Vortex lattice free wake. Tip and root vortices for one blade normalized by the blade radius, ——: Tip vortex, ——: Root vortex

Like the other approaches, the induced velocity field acts as a retarder in the axial direction (see fig.(4.54)). One of the major differences between the free wake and the prescribed ones is

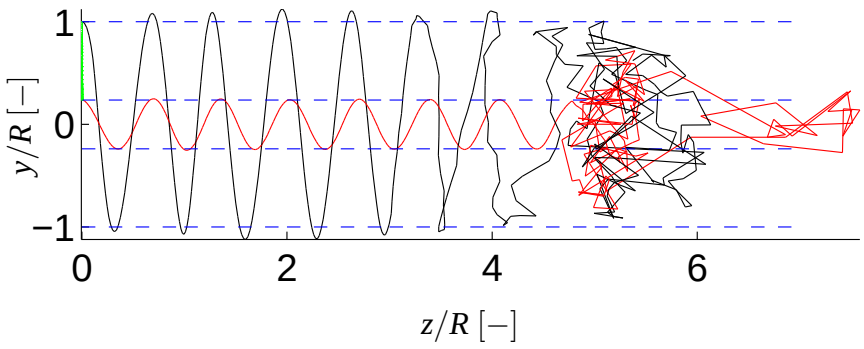

Figure 4.53: Vortex lattice free wake. Tip and root vortices for one blade in the $y-z$ plane normalized by the blade radius, ——: Tip vortex, ——: Root vortex, - - - - - -: Constant radius line

the radial expansion of the wake, as can be seen in figs.(4.53) and (4.54).

Since the axial velocity of the air is decreased by the rotor blade, the wake diameter must increase [39]. Comparison of the prescribed helix with the tip and root vortices in fig.(4.54) shows that the induced velocity field does indeed slow down the movement of the Lagrangian markers in the axial direction.

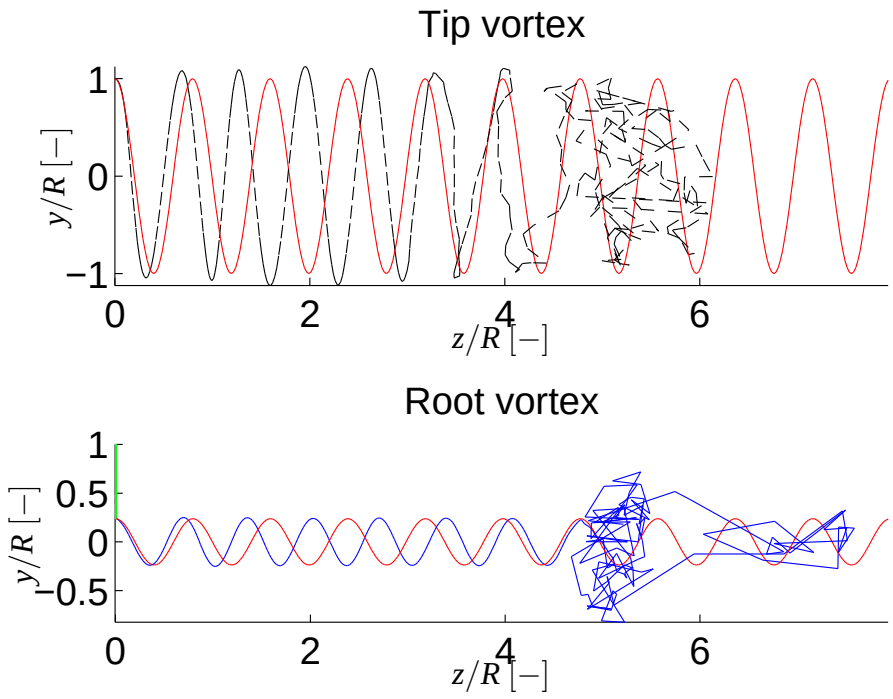

Figure 4.54: Vortex lattice free wake. Tip and root vortices compared with the helix for one blade in the $y-z$ plane normalized by the blade radius, ------: Tip vortex, ——: Root vortex, ——: Helix

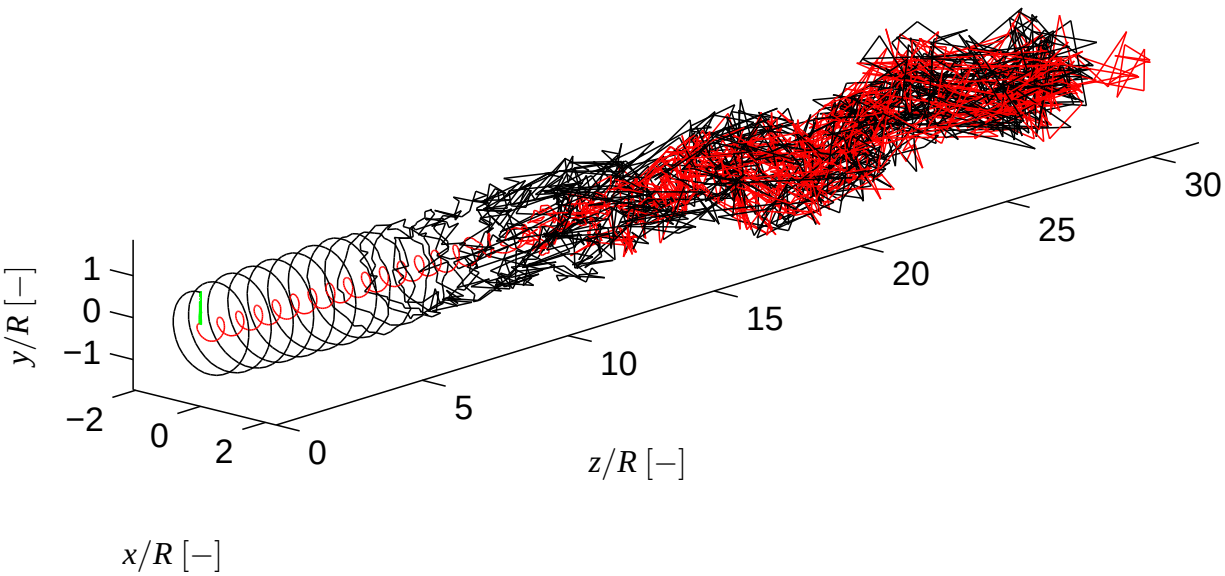

Figure 4.55: Vortex lattice free wake. Tip and root vortices for one blade and 40 revolutions normalized by the blade radius, ——: Tip vortex, ——: Root vortex

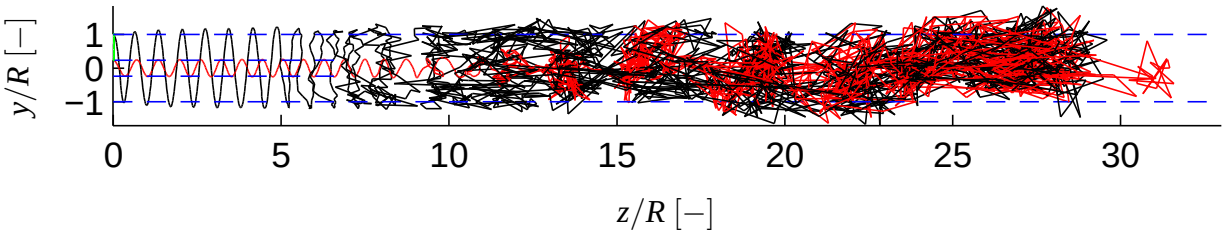

Figure 4.56: Vortex lattice free wake. Tip and root vortices for one blade and 40 revolutions in the $y-z$ plane normalized by the blade radius, ——: Tip vortex, ——: Root vortex, - - - - - -: Constant radius line

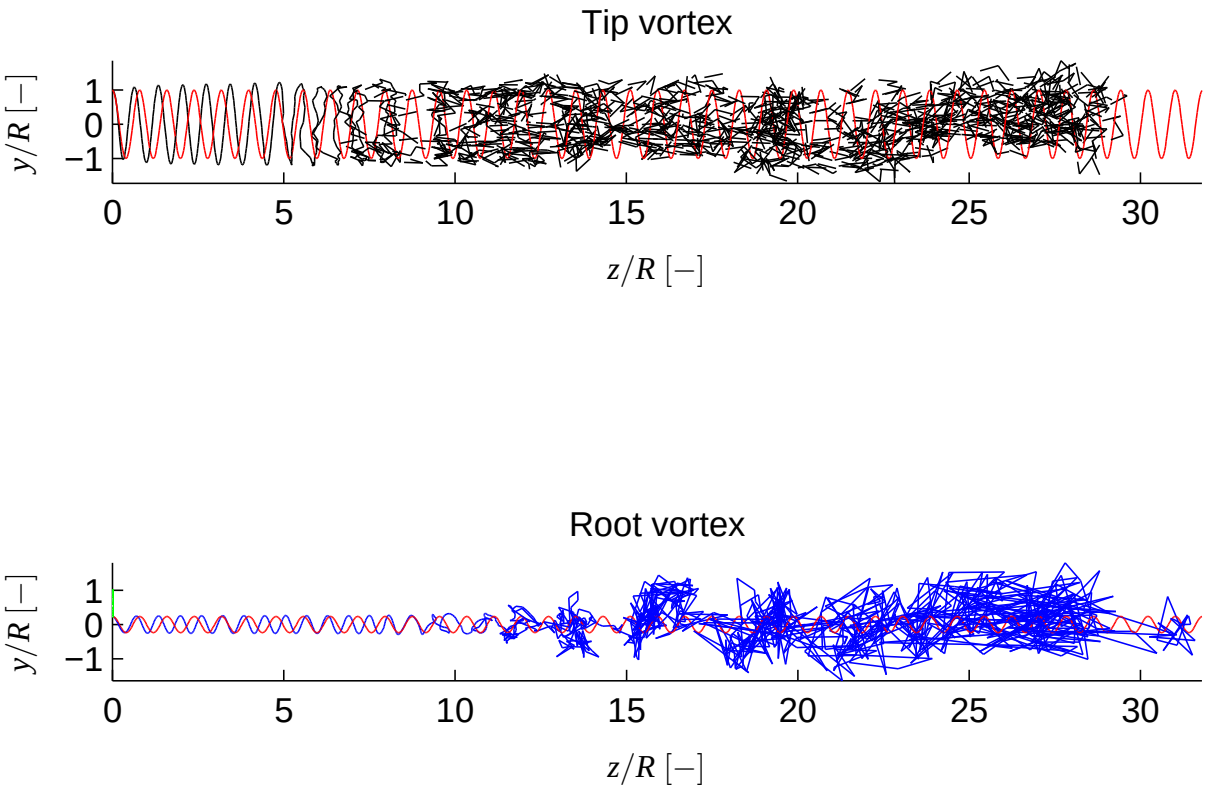

Figure 4.57: Vortex lattice free wake. Tip and root vortices compared with the helix for one blade and 40 revolutions in the $y-z$ plane normalized by the blade radius, - - - - - -: Tip vortex, ——: Root vortex, ——: Helix

Model	Power [MW]	error [%]	Thrust [kN]	error [%]
Lifting line prescribed wake	1.819	2.427	379.228	17.559
Vortex lattice prescribed wake	2.002	7.390	359.793	21.784
Vortex lattice free wake	2.002	7.392	360.651	21.598
BEM	1.949	4.566	387.042	15.860
GENUVP	2.002	7.390	365.360	20.574
NREL ([43])	1.864	—	460.000	—

Table 4.18: Power, Thrust and their normalized error for the different methods

4.4 Comparison of the different approaches

Based on the conclusions made in the previous sections, the three different approaches are compared with the BEM method and GENUVP. For all methods, the blade discretization is the same and there are 25 spanwise sections with fine tip resolution and 8 equally spaced chordwise sections. 10 degrees in the azimuthal direction is applied for the wake segmentation and the wake length is truncated after 4 rotor diameters. For the vortex lattice free wake, the explicit method is used as the numerical scheme and it is assumed that the vortex filament core radius is constant. Recall that the machine that is used for the simulations is the $5MW$ reference wind turbine [43] and the operation conditions are $\mathbf{V}_\infty = 8.0\ [m/s]$ and $\Omega = 1.0032\ [rad/s]$ as the uniform and the steady free stream and the constant rotational velocity, respectively.

Table (4.18) shows a comparison between the five different methods. Since the vortex method is a potential flow (no viscous drag), it predicts more power than the BEM method. In the lifting line prescribed wake method, the $2D$ airfoil data are used. Hence the viscous drag effect is accounted for, which results in less power and more thrust compared with the pure potential methods, i.e. the vortex lattice prescribed wake (VLPW), the vortex lattice free wake (VLFW) and the GENUVP.

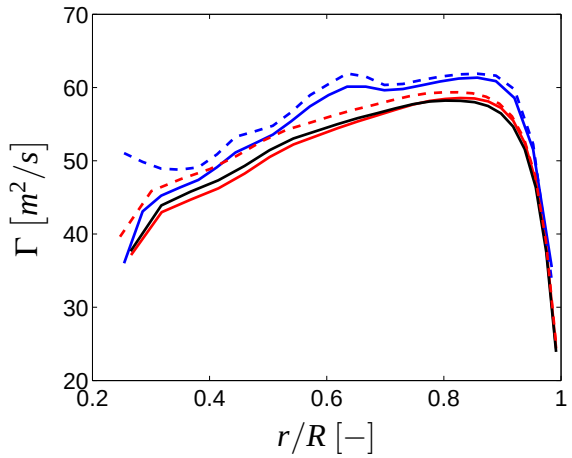

Figure 4.58: Distribution of the circulation along the blade, ——: $LLPW$, ——: $VLPW$, ——: $VLFW$, - - - -: BEM, - - - -: $GENUVP$

The circulation distribution along the blade is shown in fig.(4.58) where the maximum circulation is located near the tip. There is also good agreement between the VLPW, VLFW and

the GENUVP methods. Compared with the vortex method, the BEM method predicts higher circulation values, especially near the root.

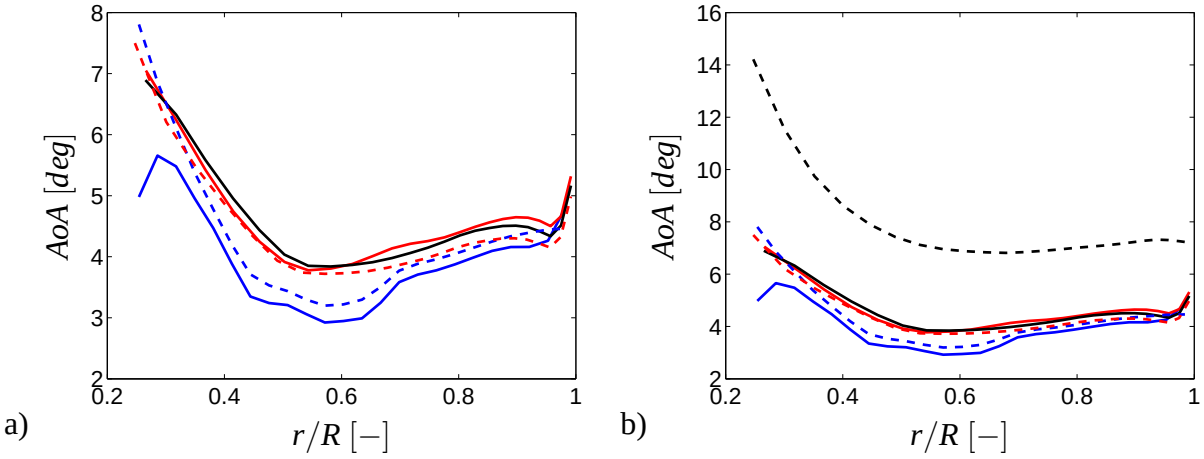

Figure 4.59: Distribution of the angle of attack along the blade, ——: *LLPW*, ——: *VLPW*, ——: *VLFW*, - - - -: *BEM*, - - - -: *GENUVP*, - - - -: *Geometric*

The effective angle of attack can be seen in fig.(4.59 a). The rotor blade in the lifting line prescribed wake (LLPW) method and the BEM method sees a smaller angle of attack compared with the other methods, which means that these methods predict a slightly larger induced velocity field over the blade. In the VLPW, VLFW and the GENUVP, the effective angle of attack is calculated based on the load distribution (see eq.(3.32)). Hence, the blade airfoil characteristics, based on the 2D airfoil data (C_L and C_D), are not detected by the solution and, contrary to the BEM and the LLPW methods, a smooth distribution of the angle of attack along the rotor blade can be observed. Figure (4.59 b) shows the geometric and the effective angle of attack along the blade. As can be seen, in all cases, because of the induced velocity field around the rotor blade, the effective angle of attack is less than the geometric one, which makes a significant power reduction for a wind turbine.

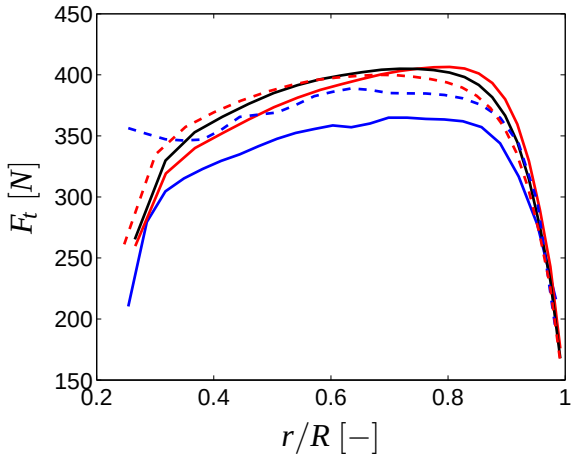

Figure 4.60: Distribution of the tangential force along the blade, ——: *LLPW*, ——: *VLPW*, ——: *VLFW*, - - - -: *BEM*, - - - -: *GENUVP*

Figure (4.60) shows the tangential force with respect to the rotor blade. Except for the BEM method , near the blade tip, the tangential force for all the methods is larger than near the blade

root, which means that the tip region of the blade produces more power compared with the other parts of the blade, especially the root region.

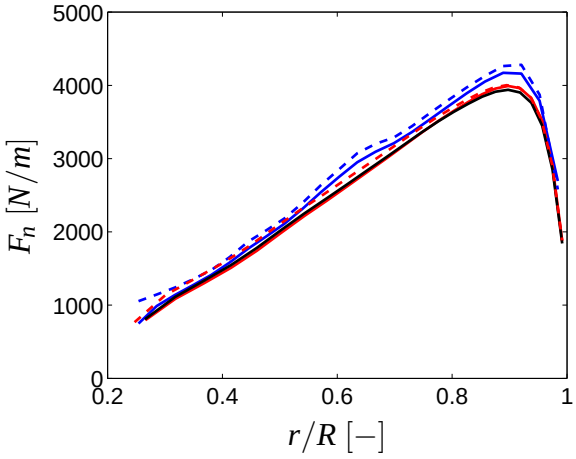

Figure 4.61: Distribution of the normal force along the blade, ——: *LLPW*, ——: *VLPW*, ——: *VLFW*, - - - -: *BEM*, - - - -: *GENUVP*

The normal force along the blade is shown in fig.(4.61) where, in agreement with the conclusion drawn based on table (4.18), the pure potential methods, i.e. the VLPW, the VLFW and the GENUVP, predict lower thrust force with respect to the rotor plane.

4.4.1 Conclusions

Comparisons were made of the three applications of the vortex method to calculate the aerodynamic loads on the rotor blade. It was shown that there are a number of factors that affect the solution, such as the blade discretization, the wake discretization and the wake truncation length. These parameters must be studied carefully during the load calculation of a wind turbine.

The root of the induced velocity field over the blade comes from the blade circulation distribution, where the calculation method has a large impact on the solution. Therefore, modeling the blade consisting of a number of panels and applying the zero normal flow boundary condition gives a more accurate circulation distribution in the vortex lattice method than the lifting line prescribed wake. The number of blade sections, both in the spanwise and the chordwise directions also have a great influence on the circulation distribution. As was discussed, the blade tip and root, especially the tip region, must be refined to resolve the large circulation gradients. The chordwise discretization must be rather fine to take into account the blade surface curvature.

The wake discretization and truncation length need attention since they are the most time consuming parts of the simulation. The results showed that, for the steady and the uniform flow, 10 degrees of azimuthal wake segmentation and $4D$ wake length fulfill both the requirements of computational time efficiency and model accuracy. For the unsteady condition, where the upstream condition may be a function of either time or space (or both), it is necessary to pay attention to the wake discretization.

In some wind turbine operating conditions, the rotor blades experience a stall condition where, in order to accurately predict separated and stalled flow along the blade, coupling the $2D$ airfoil data with an engineering approach called dynamic stall model is inevitable, especially for the vortex lattice method.

Chapter 5

Future outlook

The present project is currently cooperating with the project, Hönö turbine properties and thrust vector at yaw misalignment, where the aim is to study power generation and thrust vector at significant yaw misalignment.

Furthermore, it will also cooperate with the project Fatigue Loads in Forest Regions (TG2-2) through the Swedish Wind Power Technology Centre (SWPTC). The outcome of the TG2-2 project, turbulent fluctuation in atmospheric boundary layers both with and without forest, will be used when describing the incoming wind to the rotor blades in the present project.

There are many open issues that may enhance the vortex method for wind turbine application. Some are described briefly below:

- Modification of the Biot-Savart law such as vortex filament core thickness, vortex curvature effect, vortex stretching, vortex merging and vortex dissipation.
- Applying different parameters such as wind speed, yaw condition, wind turbulence, atmospheric boundary layer, separated flow and the blade elastic deformation.
- Blade-wake interaction for yaw angle variations and impulsive loads for pitch-regulated wind turbine.
- Self-induced motion of a vortex filament.

Bibliography

[1] W.J.M. Rankine. *On The Mechanical Principle Of The Action Of Propel1ers*. Transactions of the Institute of Naval Architects, Vol. 6, 1865.

[2] W. Froude. *On The Elementary Relation Between Pitch, Slip And Propulsive Efficiency*. Transactions of the Institute of Naval Architects, Vol. 19, 1978.

[3] Martin O.L. Hansen. *Aerodynamics Of Wind Turbines*. 2nd edition, EarthScan, 2008.

[4] A. van Garrel. *Development Of A Wind Turbine Aerodynamics Simulation Module*. ECN report, ECN-C–03-079, August 2003.

[5] L.J. Vermeer, J.N. Sørensen, and A. Crespo. Wind Turbine Wake Aerodynamics. *Progress in Aerospace Sciences*, 39:467–510, 2003.

[6] H. Glauert. *The Elements Of Airfoil And Airscrew Theory*. University Press, Cambridge, 1948.

[7] L. Prandtl. *Application Of Modern Hydrodynamics To Aeronautics*. NACA Report 116, 1921.

[8] S. Goldstein. On The Vortex Theory Of Screw Propellers. In *Proceedings of the Royal Society of London*, volume 123.

[9] V.M. Falkner. *The Calculation Of Aerodynamic Loading On Surfaces Of Any Shape*. British Aeronautical Research Council, 1943.

[10] Sandeep Gupta. *Development Of A Time-Accurate Viscous Lagrangian Vortex Wake Model For Wind Turbine Applications, Publisher = University of Maryland, Department of Aerospace Engineering*. 2006.

[11] S.D. Pesmajoglou and J.M.R. Graham. Prediction Of Aerodynamic Forces On Horizontal Axis Wind Turbines In Free Yaw And Turblence. *Journal of Wind Engineering and Industrial Aerodynamics*, 86:1–14, 2000.

[12] SG. Voutsinas. Vortex Methods In Aeronautics: How To Make Things Work. *International Journal of Computational Fluid Dynamics*, 20:3–18, 2006.

[13] J.J. Chattot. Helicoidal Vortex Model For Wind Turbine Aeroelastic Simulation. *Computers and Structures*, 85:1072–1079, 2007.

[14] J.J. Chattot. Optimization Of Wind Turbines Using Helicoidal Vortex Model. *Journal of Solar Energy Engineering*, 125:418–424, 2003.

[15] A.J. Landgrebe. The Wake Geometry Of A Hovering Rotor And Its Influence On Rotor Performance. *Journal of the American Helicopter Society*, 17, No. 4:2–15, 1972.

[16] J.D. Kocurek and J.L. Tangler. A Prescribed Wake Lifting Surface Hover Performance Analysis. *Journal of the American Helicopter Society*, 22, No. 1:24–35, 1977.

[17] T.A. Egolf and A.J. Landgrebe. Helicopter Rotor Wake Geometry And Its Influence In Forward Flight, Vol. 1 Generalized Wake Geometry And Wake Effects In Rotor Airloads And Performance. *NASA CR-3726*, 1983.

[18] A.J. Landgrebe. *An Analytical And Experimental Investigation Of Helicopter Rotor Hover Performance And Wake Geometry Characteristics*. USAAMRDL Tech. Report 71-24, US Army Air Mobility Research and Development Lab., Fort Eustis, June 1971.

[19] P. Crimi. Prediction Of Rotor Wake Flows. In *CAL/USAAVLABS Symposium Proceedings*, volume 1, June 1966.

[20] W.G. Brady and P. Crimi. *Representation Of Propeller Wakes By Systems Of Finite Core Vortices*. Cornell-Aeronautical Lab. Report No. BB-1655-5-2, February 1965.

[21] A.R. Trenka. *Development Of A Method For Predicting The Performance And Stresses Of VTOL-Type Propellers*. USAAVLABS TR66-26, June 1966.

[22] J.G. Leishman and Mahendra J.B.A Bagai. Free Vortex Filament Methods For The Analysis Of Helicopter Rotor Wakes. *Journal of Aircraft*, 39, 2002.

[23] S.G. Sadler. A Method For Predicting Helicopter Wake Geometry, Wake-Induced Flow And Wake Effects On Blade Airloads. In *27th Annual National V/STOL Forum of the American Helicopter Society*, 1972.

[24] F.N. Coton and T. Wang. The Prediction Of Horizontal Axis Wind Turbine Performance In Yawed Flow Using An Unsteady Prescribed Wake Model. *Journal of Power and Energy*, 213:33–43, 1999.

[25] H. Dumitrescu and V. Cardos. Wind Turbine Aerodynamic Performance By Lifting Line Method. *International Journal of Rotating Machinery*, 4, No. 1:141–149, 1999.

[26] D. Kocurek. Lifting Surface Performance Analysis For Horizontal Axis Wind Turbines. *SER/STR-217-3163*, 1987.

[27] H.D. Curin, F.N. Coton, and B. Wood. Dynamic Prescribed Vortex Wake Model For AERODYN/FAST. *Journal of Solar Energy Engineering*, 130, 2008.

[28] J.C. Gohard. *Free Wake Analysis Of Wing Turbine Aerodynamics*. ASRL TR-184-14, Aero, and Struc. Research Lab., Dept. of Aeronautics and Astronautics, MIT, 1978.

[29] H.A. Madsen. A CFD Analysis For the Actuator Disc Flow Compared With Momentum Theory Results. In *Proceedings of the 10th IEA symposium on the aerodynamics of wind turbines*, pages 109–124, The Technical University of Denmark, 1996.

[30] J.N. Sørensen and W. Shen. Numerical Modeling Of Wind Turbine Wakes. *Journal of Fluids Engineering*, 124:393399, 2002.

[31] M.E. Berkman, L.N. Sankar, C.R. Berezin, and M.S. Torok. A Navier-Stokes/Full-Potential/Free Wake Method For Rotor Flows. *AIAA Paper 97-0401*.

[32] G. Xu and L.N. Sankar. Computational Study Of Horizontal Axis Wind Turbines. *AIAA Paper 99-0042*.

[33] S. Schmitz and J.J. Chattot. A Coupled Navier-Stokes/Vortex-Panel Solver For The Numerical Analysis Of Wind Turbines. *Computers and Fluids*, 35:742–745, 2006.

[34] J.D. Anderson. *Fundamentals Of Aerodynamics*. McGraw-Hill, 3rd edition, 2001.

[35] A. van Garrel. *Requirements For A Wind Turbine Aerodynamics Simulation Module*. ECN report, ECN-C-01-099, 1st edition, 2001.

[36] M.J. Bhagwat and J.G. Leishman. Generalized Viscous Vortex Model For Application To Free-Vortex Wake and Aeroacoustic Calculations. In *58th Annual Forum and Technology Display of the American Helicopter Society International*, Montreal, Canada, 1113 June 2002.

[37] G.H. Vasitas, V. Kozel, and W.C. Mih. A Simpler Model For Concentrated Vortices. *Experiments in Fluids*, 11:73–76, 1991.

[38] A. Bagai and J.G. Leishman. Flow Visualization Of Compressible Vortex Structures Using Density Gradient Techniques. *Experiments in Fluids*, 15:431–442, 1993.

[39] Hamidreza Abedi. *Aerodynamic Loads On Rotor Blades*. Department of Applied Mechanics, Division of Fluid Dynamics, Chalmers University of Technology, 2011.

[40] Joseph Katz and Allen Plotkin. *Low-Speed Aerodynamics*. Cambridge University Press, 2nd edition, 2001.

[41] S. Gupta and J.G. Leishman. Stability Of Methods In The Free-Vortex Wake Analysis Of Wind Turbines. In *23rd ASME Wind Energy Symposium and the 42nd AIAA Aerospace Science Meeting*, Reno NV, 5-8 Jan 2004.

[42] G.L. Crouse and J.G. Leishman. A New Method For Improved Rotor Free-Wake Convergence. *31st AIAA Aerospace Sciences Meeting and Exhibit, Reno, NV*, 1994.

[43] J. Jonkman, S. Butterfield, W. Musial, and G. Scott. *Definition Of A 5-MW Reference Wind Turbine For Offshore System Development*. National Renewable Energy Laboratory, Colorado, USA, 2009, NREL/TP-500-38060.

[44] J. Deyoung. *Historical Evolution Of Vortex-Lattice Methods*. NASA. Langley Res. Center Vortex-Lattice Utilization, 1976, 19760021076, p 1-9.

[45] W.H. Mason. *Applied Computational Aerodynamics Text/Notes*. Department of Aerospace and Ocean Engineering Virginia Polytechnic Institute and State University, 1997.

Appendix A

1/4-3/4 rule

A.1 History

In the lifting surface theory, a point vortex is located along the blade at each spanwise section at $1/4$ chord downstream of the leading edge. The control point of each section at which the bound vortex circulation is evaluated is placed at the $3/4$ chord behind the leading edge. This rule, which is called the $1/4-3/4$ rule, is a fundamental rule in the vortex lattice method, where it was introduced by E.Pistolesi in 1937 [44]. In reality, it is not a theoretical law, and he found it from the solution of a single panel vortex lattice for a 2D wing, where he realized that, with the bound vortex at the $1/4$ chord line and the control point at $3/4$ chord (where the zero normal flow boundary condition is evaluated), the sectional lift and moment for a constant angle of attack gives exactly the same result as the thin wing theory. W. Mutterperl (1941) and J. Weissinger (1942) were the first who applied this rule [44]. The rule was extended by P.A. Byrd (1951), where he divided a wing section into a number of panels in the chordwise direction and applied the $1/4-3/4$ rule for each panel [44].

A.2 Proof

Here, a 2D flat plate is used to prove the $1/4-3/4$ rule where the bound vortex and the control point are located at arbitrary points a and b, respectively (see fig.(A.1)). The induced velocity at

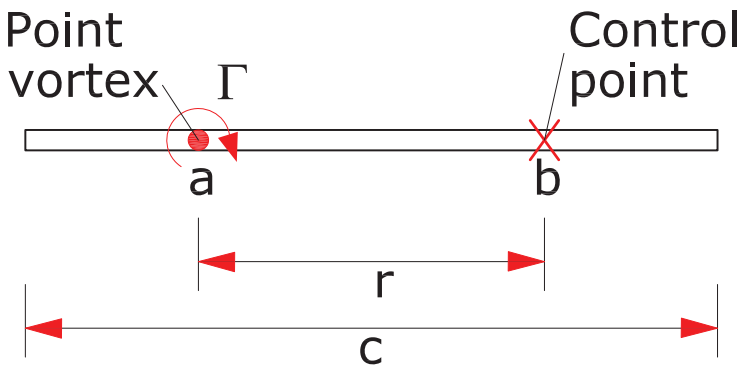

Figure A.1: Schematic of $1/4-3/4$ rule

an arbitrary point a distance of r from a point vortex gives

$$V = \frac{\Gamma}{2\pi r} \tag{A.1}$$

According to fig.(A.2), the normal component of the free stream can be written as

$$V_{\infty,n} = V_{\infty,n} sin\left(\alpha + tan^{-1}\left(-\frac{dz}{dx}\right)\right) \tag{A.2}$$

where for a small angle assumption

$$V_{\infty,n} = V_{\infty,n} sin\left(\alpha - \frac{dz}{dx}\right) \tag{A.3}$$

To satisfy the zero normal flow boundary condition, the velocity (V) induced by the vortices must be canceled by the normal component of the free stream ($V_{\infty,n}$). Therefore, a combination of eqs.(A.1) and (A.3) gives

$$\frac{V}{V_\infty} = \alpha - \frac{dz}{dx} \tag{A.4}$$

where, by ignoring the camber ($\frac{dz}{dx} = 0$), we get

$$\alpha = \frac{\Gamma}{2\pi r V_\infty} \tag{A.5}$$

The Kutta-Jukowski theory is written as

$$L' = \rho V_\infty \Gamma \tag{A.6}$$

and the potential lift, where the lift coefficient (C_L) is expressed based on the thin airfoil theory

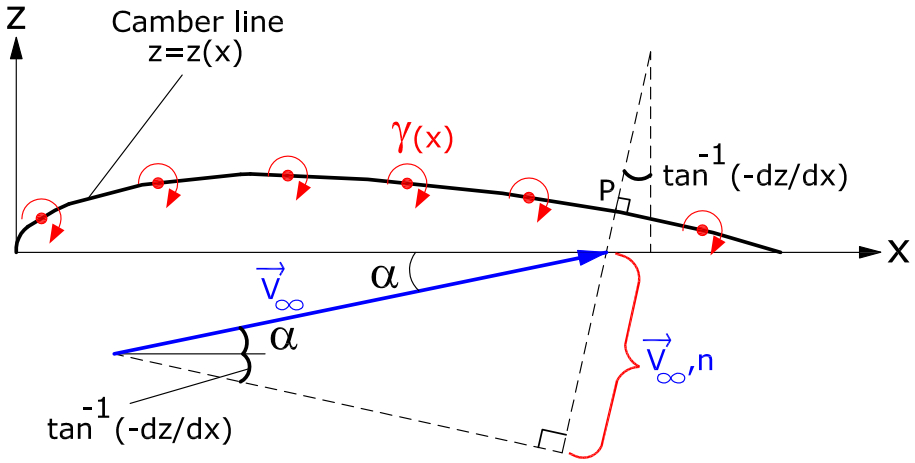

Figure A.2: Schematic for free stream and vorticity distribution

($C_L = 2\pi\alpha$), can be written as

$$L' = \frac{1}{2}\rho V_\infty^2 c 2\pi\alpha \tag{A.7}$$

Now, by combining eqs.A.5, A.6 and A.7 we get

$$\begin{aligned} \rho V_\infty \Gamma &= \frac{1}{2}\rho V_\infty^2 c 2\pi\alpha \\ &= \rho V_\infty c \frac{\Gamma}{2r} \end{aligned} \tag{A.8}$$

which means that

$$r = \frac{c}{2} \tag{A.9}$$

Equation A.9 denotes the location of a control point with respect to the vortex point based on the thin airfoil theory assumption, but it does not give any information about the vortex point location. By assuming the point vortex position at the aerodynamic center of a thin flat plate airfoil located at the $1/4$ chord point and using eq.(A.9), we get $r = \frac{c}{2}$, which proves the $1/4 - 3/4$ rule. Using the parabolic camber model determines the vortex point location, which is in agreement with the $1/4 - 3/4$ rule [45].